A STUDY OF THE CRYSTALLIZATION AND AMORPHIZATION MECHANISMS OF METALLIC GLASSES UNDER ION BOMBARDMENT

A Dissertation

by

LLOYD MILTON PRICE

Submitted to the Office of Graduate and Professional Studies of
Texas A&M University
in partial fulfillment of the requirements for the degree of

DOCTOR OF PHILOSOPHY

Chair of Committee,	Lin Shao
Committee Members,	Cable Kurwitz
	Criag Marianno
	Pavel Tsvetkov
	Xinghang Zhang
Head of Department,	Yassin Hassan

May 2016

Major Subject: Nuclear Engineering

ABSTRACT

The recent development of metallic glasses has led to a growth in study and innovation of the unique material properties these systems have to offer. In general, metallic glasses offer high yield strength, great corrosion resistance and high-elasticity. These properties, along with the ease of part creation through plastic-forming, make it a desirable material for several different industry applications. For the nuclear industry in particular, metallic glasses are being researched as coatings for reactor vessels as well as coatings for fuel cladding for long term storage. However, metallic glasses do have drawbacks. Metallic glasses are defined by their amorphous structure, and as such have an undesirable brittle failure mode. The amorphous structure is also a meta-stable structure and under several stimuli including high heat, pressure shocks, irradiation and plastic deformation can cause crystallization within the metallic glass. This crystallization does allow for some improvement in ductility but reduces strength and corrosion resistance. The nuclear environment will subject metallic glass to all of the aforementioned stimuli. It is therefore important to know under what conditions crystallization will occur and the mechanism behind the phase change in order for this material to be effectively implemented.

While crystallization under high heat and plastic deformation has been studied extensively, crystallization from irradiation is an understudied field. This behavior is difficult to describe and quantify due to its nuanced and unintuitive nature. This body of work is aimed at more completely understanding the crystallization and re-amorphization mechanisms in metallic glass due to ion bombardment. Thin film samples and bulk ribbon samples were both subjected to a variety of ion bombardment conditions. It was found that direct crystallization in thin film samples

can be induced from irradiation induced excess free volume, while it can recover to an amorphous state from rapid damage cascade quenching. In bulk studies, it was found that the beam cannot induce direct crystallization, but can make a metallic glass amorphous after it has been crystallized. These findings will help determine the proper operation envelope for this material, so it can be used effectively in engineering applications.

DEDICATION

This work is dedicated to all of those who have supported me over the years in both my professional and personal endeavors. I would like to thank especially my life partner Carey McDavid, for keeping me sane, safe and healthy, my co-workers for all of their help in my research, working through the night, weekends and on the ground, and my family for all their support in getting me to this point.

ACKNOWLEDGEMENTS

I would first like to acknowledge my adviser Dr. Lin Shao. I have worked under Dr. Shao's mentorship ever since my sophomore year in college. His guidance and support is the reason that I have been able to progress my professional career to the degree I have at this point. The principles and advice he has imparted to me over the many years will be sure to guide and influence my decisions for many years to come.

I would also like to thank mark Hollander for his guidance and support for all of my undergraduate work and most of my graduate career. I still recall my first summer working in the IMF facility and learning more about ion beam systems than I though I would ever know in my life. Continuing for years after that Mark continued to teach me about not only ion beam systems themselves, but a methodology for designing, troubleshooting and repairing all manners of scientific equipment. This knowledge is sure to inform decisions that I will make many years from now.

Next I would like to thank Xuemei Wang for her support through my graduate career. The advice and lessons that I gained from her have helped me mature through my research in graduate school. She has taught me invaluable lessons about thorough problem solving methodologies and excellent standards for all aspects of research.

A large thank you must also be given to Dr. Guoqiang Xie of the Institute for Materials Research in Tohoku University for providing the samples. Without this contribution, none of the research presented here would be possible.

Tianyi Chen provided invaluable time creating samples using the FIB lift-out process as well as sample characterization using TEM operation. His expertise and tireless efforts were crucial in the execution of this project.

TEM observation was also performed by Jonathan Gigax. His help in performing the multiple types of imaging and sample characterization techniques cannot be understated.

FIB preparation was also aided by Hyosim Kim. Her expertise in sample preparation greatly expedited analysis time. The samples produced by her were of exceptional quality and allowed for the observation of very nuanced phenomena by TEM observation.

Maintenance and operation of the 140 kV system for the He implantation was helped in large part by Elizabeth Castanon. Without her efforts, the irradiations would have been greatly delayed.

NOMENCLATURE

RBS	Rutherford Backscattering Spectroscopy
NRA	Nuclear Reaction Analysis
PIXE	Particle Induced X-ray Emission
ERD	Elastic Recoil Detection
GVM	Generating Volt Meter
TEM	Tunneling Electron Microscope
FIB	Focused Ion Beam
MG	Metallic Glass
TTT	Time Temperature Transition
SEM	Scanning Electron Microscope
EDS	Energy Dispersive Spectroscopy
STEM	Scanning Transmission Electron Microscopy
EELS	Electron Energy Loss Spectroscopy
IBA	Ion Beam Analysis
SNICS	Source of Negative Ions by Cesium Sputtering
GVM	Generating Volt Meter
DI	De-Ionized
FIB	Focused Ion Beam
TEM	Transmission Electron Microscopy
DSC	Differential Scanning Calorimetry
DPA	Displacements Per Atom

TABLE OF CONTENTS

Page

LIST OF FIGURES

FIGURE Page

LIST OF TABLES

TABLE Page

1. INTRODUCTION

This chapter is intended to provide an overview of the characteristics of metallic glass, motivations for its implementation in practical engineering applications and issues preventing its current use. First, a description of the general system is provided to familiarize the reader with its properties. Next, the strengths of metallic glass when compared to traditional materials are discussed in detail. Weaknesses of metallic glass will then be addressed which provide motivation for the studies performed in this dissertation. Finally a review of previously performed studies will be given to provide the basis of the work performed here.

1.1 Metallic Glass: Overview

Metallic glass (MG) is a relatively newly discovered and novel material defined by its metallic composition and amorphous atomic structure [5] [6]. Unlike most metal alloys, which have a poly-crystalline structure, MG has no regular arrangement of its atoms; rather they are spread randomly throughout the material. To produce this material, a liquid pool of the desired composition must be made. Several heating options are available for this, but all take place in an oxygen free environment. Next, the liquid metal must be rapidly quenched. If the solidification is rapid enough, the end result will be a metallic solid with the desired amorphous structure. If the cooling rate is too slow, the results will be a traditional poly-crystalline material. An image of metallic glass in ribbon and ingot form can be seen in Figure 1.1.

The composition of a metallic glass is very important. Several factors influence the ability of a composition to form an amorphous microstructure. Each of these factors help to frustrate crystal formation or expedite cooling, allowing for slower cooling rates to be used to form the metallic glass.

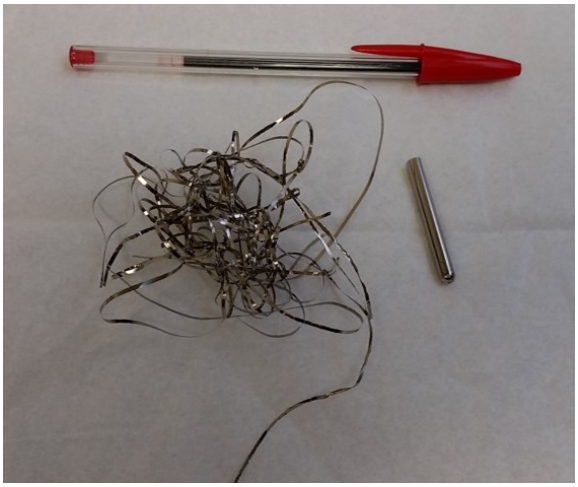

Figure 1.1: An image of a metallic glass ribbon, formed by the melt spinning process, and a metallic glass rod, formed by casting. The pen is provided for size comparison.

First, good compounds for glass forming will typically have 4-5 primary elements. This mix of different atoms will enhance the effectiveness of the other factors by providing even more diversity.

In their pure forms, each of these elements should form a different crystal structure (Ex. Body-centered, Face-centered, Hexagonal, ect.). With each of the elements attempting to form different crystal structures, the atoms will have a difficult time aligning and "choosing" a crystal lattice form.

It is also desired that these elements have a large atomic size mismatch. This again makes it difficult for all of the elements to form a single crystal structure which is a low energy state for all elements involved.

Lastly, if possible, the elements should have a negative enthalpy of mixing. This characteristic helps solidify the mixture more quickly, effectively accelerating the cooling process.

The different structures and large atomic size mismatch help frustrate crystal formation. This allows the amorphous structure to be formed even with a slower

cooling rate. The negative enthalpy of mixing helps cool the sample more rapidly, helping solidification. A hypothetical time temperature transition (TTT) diagram showing these enhancements from these factors can be seen in Figure 1.2.

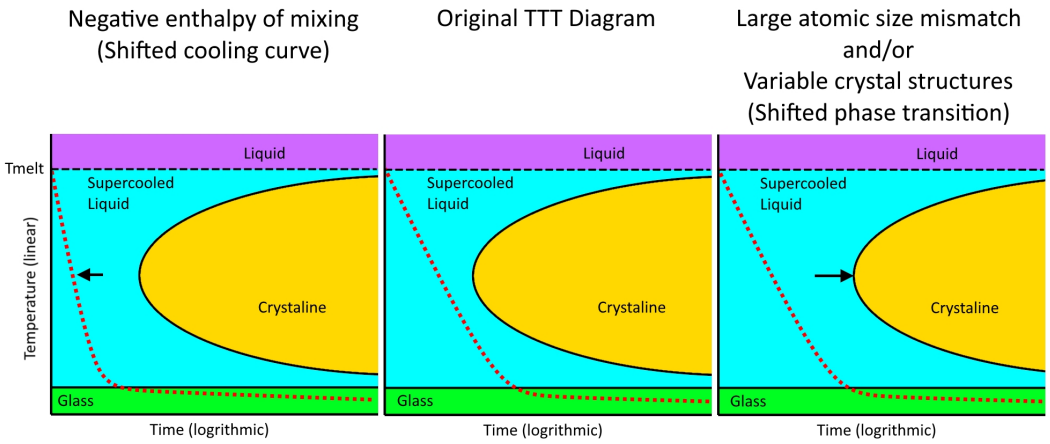

Figure 1.2: Three hypothetical TTT diagrams showing the impact of various parameters affecting the glass forming ability.

All of these characteristics will determine at what rate the liquid metal needs to be solidified in order to form an amorphous solid. This rate is known as the critical cooling rate. A glass with a slow critical cooling rate is said to have good glass forming ability. The glass forming ability of any compound being considered for metallic glass is incredibly important since the maximum thickness of a metallic glass component is ultimately limited by the critical cooling rate. A metallic glass compound with very poor glass forming ability can only form very thin components, as it must be cooled very rapidly. Conversely, compositions with a good glass forming ability can be made into thick components, enhancing the practical useability.

An amorphous structure results in two primary microstructure characteristics

which determine the compound's mechanical behavior. First, there are no traditional crystalline defect structures such as interstitials, vacancies or dislocations. Since there are no dislocations which can move, metallic glass has a distinct lack of plasticity. This is similar in behavior to other non-metallic element based amorphous materials. While there are no interstitials or vacancies, in the traditional sense, there are areas of abnormally high or low packing densities. These defects will form the nucleation sites for shear bands which will form whenever the metallic glass is loaded past the elastic limit. Without any sort of grain boundaries, or crack tip deforming, the shear bands will propagate through the material without any barrier, causing catastrophic failure of the metallic glass.

Secondly, there are no grain boundaries. This is part of the reason shear bands can propagate without restriction. The lack of grain boundaries also aids in the inherent corrosion resistance of metallic glass. Corrosion normally occurs initially on exposed grain boundaries since they are more susceptible to the corrosive agent[7].

1.1.1 Manufacturing

There are many ways to produce a metallic glass. Most methods initially start with arc melting. In this process, an arc welder is used to flash melt and cool the stock material. This is often the first step since the raw elemental stock is often difficult to melt by conventional means. A pictorial representation of this process with the end result can be seen in Figure 1.3. By melting the stock materials together, they form a mixture which has a much lower melting temperature and is then easier to melt by conventional resistive heaters for re-casting.

Once the stock has been made, several different methods can be used to form the final desired shape. Tilt casting is a popular method of producing nearly any shape of metallic glass desired. A diagram of this process can be seen in Figure 1.4.

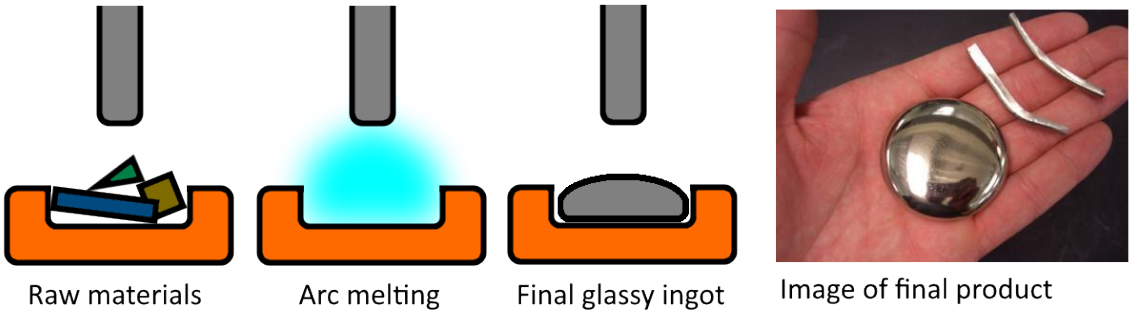

Figure 1.3: Pictorial diagram of metallic glass manufacturing by the arc discharge method and an image of a final ingot. Image by: PNAS/Douglas Hofmann, Caltech

In this technique, the metallic glass stock material is first melted in a heated pool. The molten material is then poured into an actively cooled mold, normally made of copper (Cu), in order to remove heat and quench the material into its solid state as quickly as possible. The solidified metallic glass can then be removed from the mold and processed as needed. An example of a metallic glass rod formed by this method can be seen in Figure 1.1.

A popular subset of casting is a process known as melt spinning[8]. Figure 1.5 provides a pictorial representation of this method. In this process the molten feed material is poured directly onto a cooled spinning wheel. When the molten material hits the wheel it solidifies extremely rapidly, forming metallic glass. This method is very popular for producing samples for scientific research for several reasons. Samples produced in this way have very uniform properties, and a very low percentage of crystallinity. Melt-spinning provides extremely high cooling rates, so most metallic glass compounds, even those with poor glass forming ability, can still be formed using this method. Most scientific experiments also do not require large samples for testing. The ribbon shape provides a large surface area with little overall volume, allowing for large amounts of usable samples to be produced with a small amount of

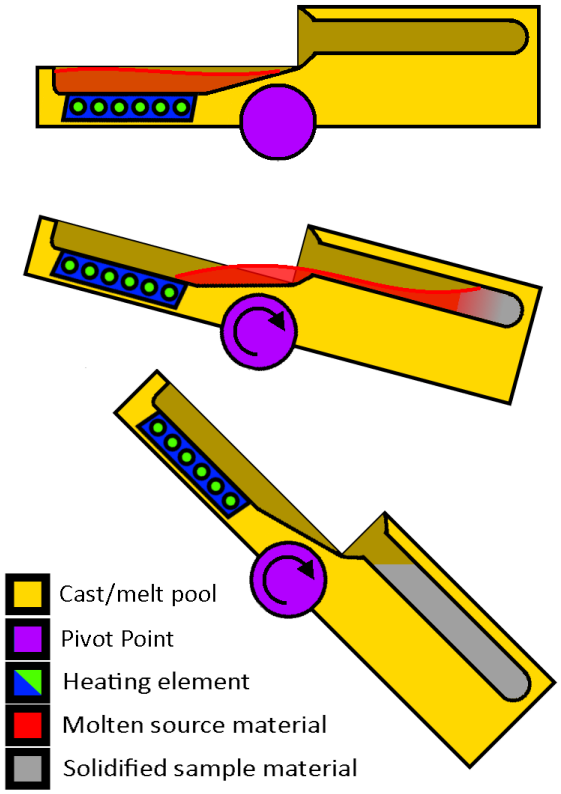

Figure 1.4: Pictorial diagram of metallic glass manufacture by tilt casting method

source material. A ribbon sample produced from this process can be seen in Figure 1.1.

Lastly, if finer control over the sample geometry is desired, metallic glasses can also be formed by magnetron sputtering. Using a standard magnetron sputterer, samples can be formed in thin layers. This method is advantageous since layer thickness is able to be controlled on the order of nanometers, and thick layers of alternating compositions can be formed. An example of a resulting structure formed using this method can be seen in Figure 1.6.

In the studies performed here, both melt spun ribbon samples and magnetron sputtered samples were used. In both cases the samples were determined to be

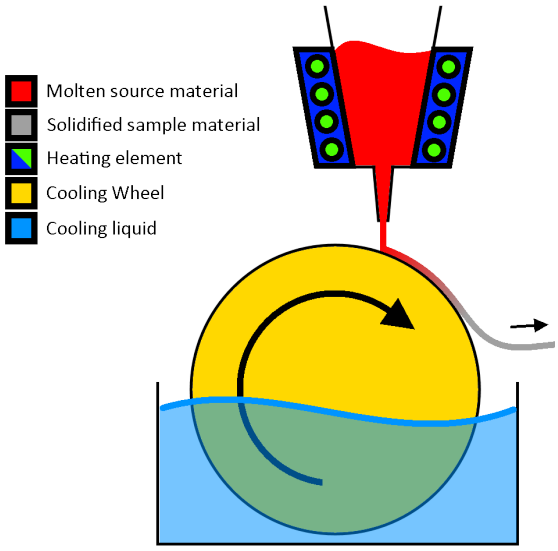

Figure 1.5: Pictorial diagram of metallic glass manufacture by melt spinning

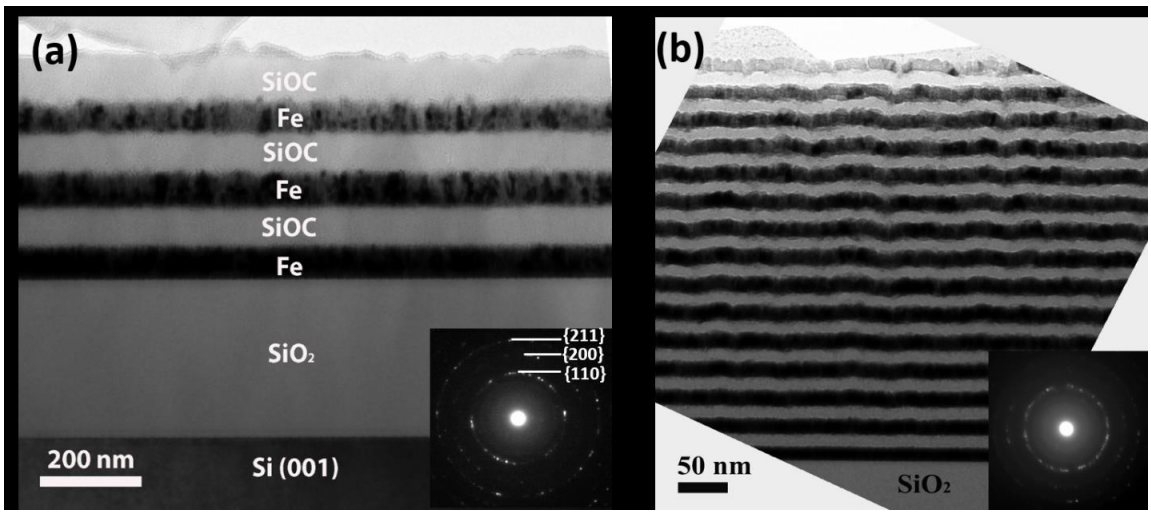

Figure 1.6: TEM image of a layered metallic glass specimen produced by magnetron sputtering

completely amorphous before any testing began.

1.1.2 Benefits

No matter how it is produced, the amorous structure of metallic glass comes with some very beneficial properties which has driven research on these materials. MG's have a very high strength [9]. This strength not only comes from the bonds between elements but their amorphous arrangement. The stress strain curve seen in Figure 1.7 is a clear illustration of this advantage. This high strength mainly comes from the fact that there is no dislocation movement within the material. Since there are no defects which will move easily with an applied strain, the atoms are frozen in place, forced to hold onto their neighboring atoms until sufficient force is applied to rend many atomic bonds at once.

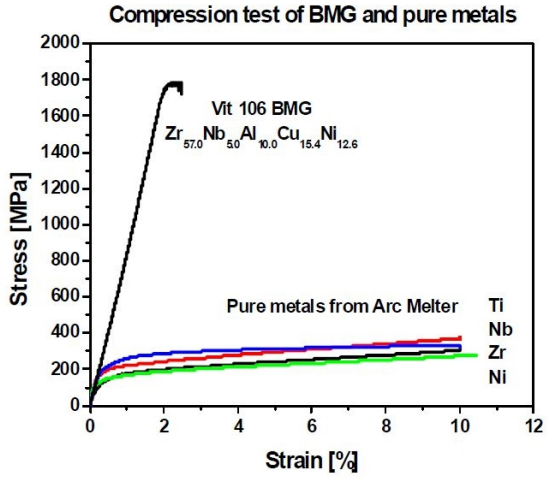

Figure 1.7: A comparison plot of the compressive strain stress curves for a commercially available metallic glass, Vitreloy, and its elemental components [1].

MG's are also very corrosion resistant [10]. This is due to two factors. One is that the highly variable composition of the metallic glass makes it very improbable that a corroding agent will attack all of the elements. Secondly, the amorphous structure

is naturally corrosion resistant. Upon forming, the metallic glass in general will have a very smooth surface, free of sharp edges or cracks which are corrosion susceptible. Also metallic glasses have no grain boundaries that can be exposed to the corrosive agent. Grain boundaries are areas of very low packing density and high free surface energy, which makes them susceptible to chemical corrosion[7]. Since metallic glass only presents its bulk structure, it is more difficult for the corrosive agent to attack the material.

These materials also have a higher fracture toughness than most ceramic materials, which is their closest material counterpart [11] [8]. Fracture toughness is a very important factor especially when dealing with brittle materials. In engineering applications a high fracture toughness can be the difference between a brittle material failing catastrophically or staying structurally sound when it is struck or chipped. In more ductile materials, fracture toughness is not a critical consideration since the materials can stop crack propagation by crack tip blunting. However, in brittle materials, once a crack is formed, it cannot be stopped. The fact that metallic glasses outperform ceramics in terms of fracture toughness makes it more desirable to be used as a load bearing material.

When compared to ceramics, metallic glasses also have a much higher thermal conductivity and can conduct electricity. While this is not a direct improvement over ceramics, it does open the possibility of applications in places where ceramics are either unusable or undesirable. For instance, a coating on a pipe that is heat cycled will need to expand and contract with the pipe to avoid micro-crack formation. Ceramics may have the corrosion resistance desired, but due to their low thermal conductivity and low coefficient of thermal expansion, the coating will crack over time exposing the pipe wall to the corrosive agent. Metallic glasses on the other hand, have the corrosion resistance desired but also will stay close to the same temperature

of the pipe, and expand and contract at the same rate. This greatly improves the longevity of the metallic glass coating when compared to a ceramic option.

1.1.3 Motivation

While MG does have many desirable characteristics, it also has detriments which have prevented its widespread use in engineering applications [12]. With their high strength, MGs have very low ductility, also shown in Figure 1.7, resulting in a low toughness [13]. This class of material is also very difficult to manufacture. Many times, manufacturing thicknesses are limited by the critical cooling rate of the MG [8]. Most research focuses on solving these two problems: improving the ductility of MG without greatly sacrificing strength, and finding compositions of elements with good glass forming abilities[14] [15].

However, there is another issue with MG that is of particular concern to the field of nuclear engineering: its metastable state. When MG is formed by rapidly quenching a liquid mixture into a solid, the atoms do not have time to find their lowest energy configuration. This leaves them in the amorphous state which is at a higher energy than the lower energy poly-crystalline state. While at many mild conditions the amorphous structure is stable, there are several conditions under which the MG will revert to a crystalline state. High temperatures, pressures, or irradiation can all cause MG to crystallize [16] [17] [18]. Figure 1.8, acquired by Transmission Electron Microscopy (TEM), shows a side by side comparison of the micro-structure of MG before and after crystallization.

As can be seen in Figure 1.8, the transition from an amorphous to crystalline structure results in a massive re-structuring of the atoms. This will result in atomic segregation, a decrease in corrosion resistance, as well as reduction of the overall strength of the material. This change is undesirable under most conditions as it will

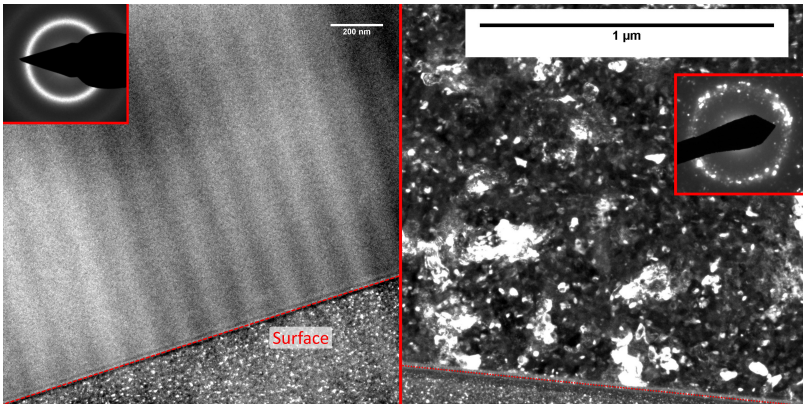

Figure 1.8: Two micrographs acquired by TEM of two MG specimens. One, completely amorphous, the other after undergoing complete crystallization. Both images were taken using the dark field technique in order to highlight crystallinity in the samples.

radically change the character of the material, more than likely making it unsuitable for the original intended application.

1.2 Previous Works

While testing for heat and pressure conditions is relatively straightforward, the response to irradiation is much more complex and nuanced [19]. Radiation response is also a characteristic that will have widespread impact in the nuclear field. As such, this body of work seeks to understand the radiation response of MG due to charged particle bombardment.

This work is sorely needed as there is a distinct lack of research concerning the effect of MeV level particle bombardment on metallic glass. This is a crucial subset of radiation damage response as it is a very common type of damage event in a fission or fusion type nuclear reactor. Studies outside of the advisers group so far have used swift heavy ion bombardment in the hundreds of MeV to GeV range [20] [21] or electron bombardment [22]. These experiments are able to answer some

important questions about the fundamental responses of MG, however, they are not a good representation of the types of damage expected in a reactor. These studies are also primarily focused with either the changing magnetic behavior or the effect of strong coulombic interactions on the viscous flow rate of MG. None of these studies have a strong focus on the onset of phase changes within the MG or show detailed changes of the internal structure. Characterization techniques primarily use scanning electron microscope (SEM) with supplementary X-ray measurements. Neither of these techniques give any detailed observation of the evolution of the internal structure after bombardment. The conclusions gathered from these studies are limited in the engineering context and the results gained are of little use to understanding the mechanics of crystallization in MG.

For instance, *Sorescu et al.* [22]shows that under extremely intense low energy electron bombardment, crystallization can occur. However, it is very likely that the very high energy deposition rate caused crystallization in these samples simply due to heating of the MG above its crystallization temperature.

Inside the advisers' group, some previous experiments have been done regarding MG crystallization due to ion bombardment. One such experiment shows that crystallization may be caused by ion-induced segregation [17]. MG stability is very reliant on composition. Changing the compositional makeup, even by a few atom percent, can create an compound which is not able to maintain an amorphous state at room temperature. The hypothesis given in this study is that ion-mixing may allow certain elements to form compounds which more readily create a crystal structure. TEM evidence is given to support the hypothesis.

It has also been shown in another study within the advisers group, that controlling the temperature of the substrate effects the resiliency of MG to crystallization [23]. In this study, an ion milling machine, normally used for sample preparation, was

the sample treatment tool. Ion energy as well as the substrate temperature were investigated. Crystallization is readily caused by ion milling under standard operating conditions. However, it was observed that by reducing the energy of the bombarding ion or lowering the substrate temperature using liquid nitrogen, crystallization can be prevented.

These studies are a good starting point, but lack a breadth of knowledge in order to truly determine the mechanics involved in the crystallization of MG. This study of the MG response to irradiation is broken into three main categories based upon the macroscopic sample geometry: thin film, layered structures, and bulk MG. This categorical system rises naturally from the studies, as each system will require unique sample preparation, treatment and characterization. Each study is aimed at revealing a unique aspect of the crystallization/amorphization behavior.

2. EXPERIMENTAL DATA ACQUISITION

All experimentation uses various scientific equipment and measurement techniques to acquire information about the systems being studied. Knowledge of the inherent strengths and flaws as well as the operational principles of each device and technique used is extremely important in experimental design, and interpreting results. In completing this project, many unique and complex pieces of equipment and measurement techniques were used. This section is aimed at explaining the relevant details of each piece of equipment and the nuances of the techniques used.

2.1 Equipment

All equipment outlined in this section was chosen based on its strengths, weaknesses and availability to the researcher. In this section, the operating principles will be described for each piece of equipment. The goal is to show how each piece of equipment works which will help shed light on how physically each technique is performed.

2.1.1 General IONEX 1.7 MV Tandem Accelerator

The 1.7 MV Tandem accelerator used for these experiments was made by the General Ionex Corporation in 1983. To generate the ions used in the various experiments, the accelerator has two different source heads which feed the main acceleration column. After being accelerated by the main terminal voltage, the ions are directed down a beam pipe to one of three target chambers where the ions will impinge upon the target material. To describe this system in greater detail, it is convenient to isolate the accelerator into three main sections: low energy, main acceleration column, and high energy. Each of these sections will be discussed in greater detail. An

overview of the system showing all major beam optic components is shown in Figure 2.1.

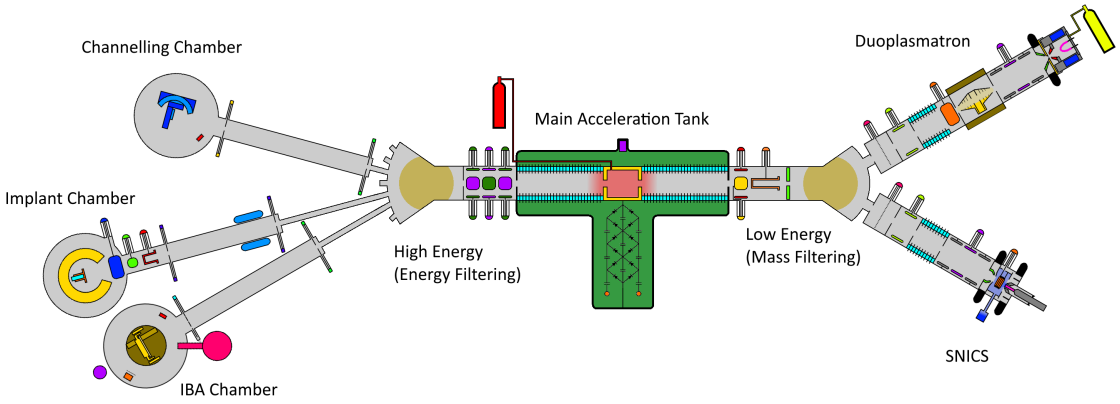

Figure 2.1: A schematic showing the overall structure of the 1.7 MV Tandem accelerator

2.1.1.1 Low Energy

The low energy end of the accelerator is comprised of three main components: a Source of Negative Ions by Cesium Sputtering (SNICS) source, a Duoplasmatron source, and a low energy magnet. Each source is capable of producing ions and accelerating them to a low energy to feed to the low energy magnet. That magnet is then used to bend the ion beam into the main acceleration column. The low energy end of the accelerator is kept at high vacuum by three 1000 l/s turbo pumps, each backed by dual-stage rotary vane oil pump. Turbo pumps are used due to their ease of use, fast pumping speeds, low contamination and small size profile. Oil pumps are used at the low energy end due to their robust nature and high pumping speeds. Since the turbo pumps at this end are ran continuously, oil contamination caused by back streaming from the oil roughing pumps is not an issue.

2.1.1.2 Low Energy: SNICS

The SNICS source uses a solid cathode as the source material for the ion beam it produces. Extracting ions from a solid gives this source great flexibility as all elements on the periodic table, with the exception of the noble gases, can be found in a solid form. It is important to note that even elements not found as a solid in pure form, such as hydrogen, can still be produced through the use of compounds (ex. TiH). This source can be operated reliably for long periods of time with a very stable beam current before any maintenance is required. A schematic of the source displaying the beam optics and vacuum system components is shown in Figure 2.2. This graphic may be useful to reference as the operation principles are described.

The operation principles of the source are quite interesting. The source is based around sputtering using cesium (Cs). The cesium begins as a liquid in a reservoir below the source head. This liquid is heated, causing some of the cesium to become a vapor and travel up the chimney pipe. From here, some cesium will drift towards the target cathode and condense on the surface, forming a thin layer of cesium. This thin layer of cesium is important as it enhances the percentage of ions produced that are negatively charged. While some cesium goes directly to the target cathode, most of the cesium will travel into the ionizer chamber. In the ionizer chamber, a heated coil, known as the ionizer, produces thermal electrons by being heated to a very high temperature. The ionizer temperature is controlled by adjusting the amount of electrical current that passes through it. These thermal electrons are accelerated by the target voltage potential and are directed into long, spiraling paths by a static magnetic field. The electrons, on their long path, have a good chance of colliding with a cesium atom, causing it to lose an electron and become positively charged. Cesium is very easily ionized, even by low energy electrons due to its extremely

weak electronegativity. Weak electronegativity, along with its low melting point and high atomic mass, is why this element is chosen as the sputtering species in this source. The cesium, now positively charged, will be accelerated by the target voltage into the cathode, depositing large mounts of energy in the near surface region and causing target material to sputter off. The sputtered target material will have to travel through the thin layer of cesium, which will easily give up an electron to the target atoms. This effect will cause the majority of sputtered target atoms to become negatively charged as they leave the cathode. These negatively charged ions are then accelerated away, initially by the target voltage, and then by the extraction voltage.

After accelerating through the extraction voltage, the ions go through a focusing element, an einzel lens. The beam at this point is very diffuse and this lens helps focus the charged particles immediately after leaving the source head. The beam is then given more energy as it passes through the pre-acceleration column. This will add and additional 40-50 keV of energy to the beam. This extra energy is essential later to resolve different elements after bending them through the low energy magnet. Without the higher energy, many elements would be unable to be separated resulting in a contaminated, multi-element, beam. After gaining energy through the pre-acceleration column, the beam travels through a set of electrostatic deflection plates, which help position the beam in the vertical direction. Next, the beam goes through another focusing element, the grid lens, to the focus the beam one last time before it is sent to the low energy magnet.

2.1.1.3 Low Energy: Duoplasmatron

The duoplasmatron source head is a gas-based source head, meaning that is uses a gas feed as the source material to produce ions. This source head is a compliment to the SNICS source head, since the Duoplasmatron can produce beams of noble

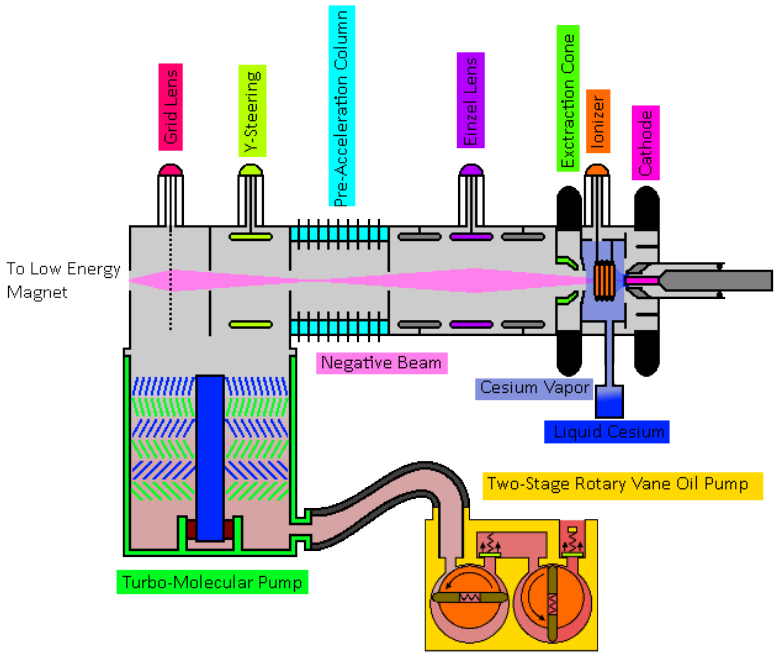

Figure 2.2: A schematic operation of the internal structure and operation principles of the SNICS ion source.

gas elements that the SNICS cannot. This source head in particular is optimized to produce intense helium beams which can be used for implantation or lesser intensity beams for ion beam analysis. Since it does not contain any cathode material or sputtering element, the duoplasmatron can be used for a very long time before any maintenance is required. A schematic diagram for this source head is provided in Figure 2.3. This diagram may be useful as a reference in understanding the operating principles of this ion source.

The ion beam begins as a gas which is fed into the source head through a leak valve. This valve is specially designed to be able to feed in gas at a very low volumetric flow rate into the source head chamber. This type of valve is needed due to the sensitive nature of the high-vacuum environment. The source head chamber geometry is similar to a bottle, with the majority of the chamber being a constant diameter

and one end of it pinched. The chamber walls are made of ferritic iron, so that they transmit magnetic field lines from the electromagnet which surrounds the source head chamber. Inside this bottle, a filament is heated in order to produce a wealth of free thermal electrons. The filament in this case is a platinum gauze coated in a material designed to enhance thermal electron emission. This setup creates the very large number of free electrons required for the duoplasmatron to operate. The area immediately surrounding the filament forms a diffuse plasma which is used mainly to enhance the number of free electrons. These free electrons are confined along the axis of the source head by the magnetic field, and then sharply concentrated near the source exit by the convergence of the magnetic field lines along the geometry of the source walls. The concentration of electrons, and the ionized gas forms a distinct and very dense plasma region at the bottle exit, producing the second plasma that the source head derives its name from. This dense plasma bubble is formed very close to the extraction voltage which extracts positively charged ions from the dense plasma.

The newly extracted beam is very poorly shaped, so it is immediately passed through an einzel lens to help better define the beam. The beam at this point is positively charged, however, since a tandem acceleration column is being used, the beam entering the column must be negatively charged. To produce a negatively charged beam, the positive beam from the source head is sent through a charge exchange canal after the einzel lens. This canal is filled with sodium (Na), that is heated until it is a liquid. The liquid sodium produces vapors which will interact with the beam. Due to sodium's low electronegativity, it will give up electrons to the incoming positive beam relatively easily. If a positive ion collects two negative charges in this process then it will become a negative ion. The probability of this occurring is quite low, and the maximum efficiency for this process is close to 5%.

The remainder of the beam will either be neutralized or remain positive. The mixed beam leaving the charge exchange canal is then sent to an electrostatic bending plate which will bend the negative beam down the pre-acceleration column. Conversely, the positive and neutral beam will be steered away, leaving only the usable negative beam to continue. The negative beam will then travel down the pre-acceleration column, gaining 40-50 keV of energy. It is vital that this beam be at a sufficient energy to separate the different elemental species produced by the source head in the low energy bending magnet. After the pre-acceleration column, the negatively charged beam passes through a set of vertical electrostatic steering elements, and then a grid lens for final focusing before entering the low-energy bending magnet.

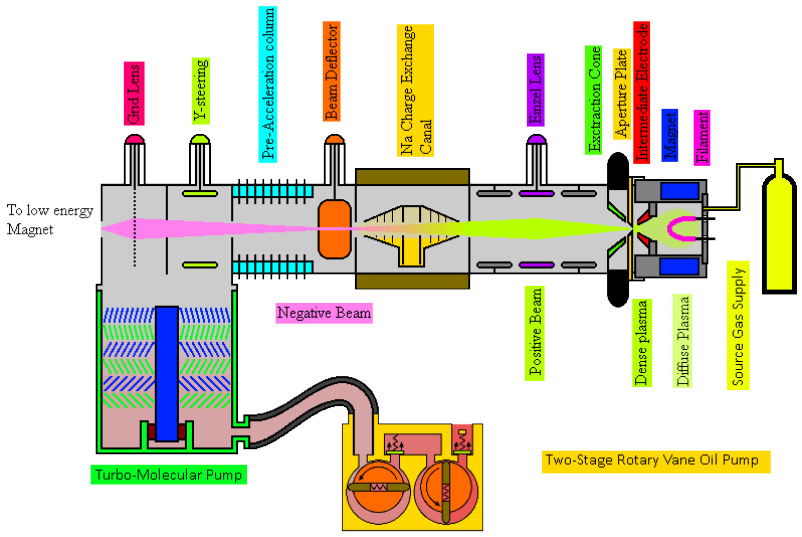

Figure 2.3: A schematic of the internal structure and operation principles of the Duoplasmatron ion source.

2.1.1.4 Low Energy: Bending Magnet

The bending magnet at the low energy end is the last major component before the beam is sent to the main acceleration column. It is extremely important to the operation of the accelerator system and performs several functions. Firstly, without a low energy magnet, this accelerator system could only have one source head. By having this magnet, and being able to switch polarity, ion beams produced from both the SNICS and duoplasmatron sources can be bent to travel down the main acceleration column. This lends great flexibility in beam production and expands the capability of the accelerator to a great degree. Similarly, the low energy magnet provides the main horizontal direction control in the low energy system. Lastly, but arguably most importantly, the low energy magnet performs a mass filtering function. A schematic of the low energy magnet system is shown in Figure 2.4. This graphic shows the beam passing through the magnet, illustrating the filtering mechanism of the magnet.

All ions at this point in the system are coming out of the source heads with the same energy. Neither source head can produce multiple charge state ions to any great degree, so nearly all ions are single charged, giving them the same energy. Since ions from the source head have the same energy, they will be bent to different angles according to their mass. Lighter ions will bend to a greater degree than heavier ions of the same energy, given the same magnetic field. This effect is used to purify the ion species that enter the main acceleration column. This filtering function is vital since both source heads produce beams with large amounts of impurity species. For example, the duoplasmatron will produce large amounts of oxygen and nitrogen ions from filament off-gassing and the SNICS source produces whatever elements are in the cathode, which are often compounds. A common example is titanium hydride

(TiH) in a copper (Cu) jacket which will produce Ti, Cu, H, and O in large quantities.

Many accelerator systems utilize a single bending magnet which must filter both energy and mass. The problem with this setup is that many species will be separated by a very small magnetic field setting, or be completely overlapping and indistinguishable from each other. However, in a tandem accelerator there are allowed to be two bending magnets, as is the case here. This extra level of filtration ensures that the correct element at the correct energy will be impinging upon the sample.

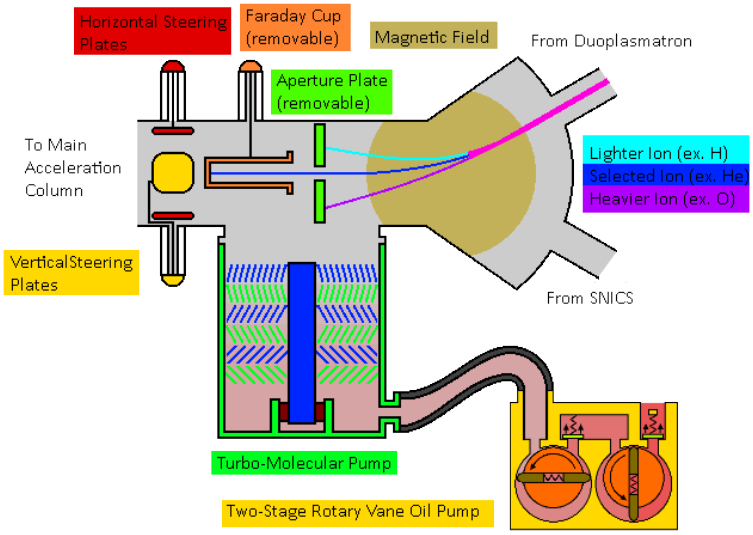

Figure 2.4: A schematic of the internal structure and operation principles of the low energy "mass filtering" magnet. Particular emphasis is placed on beam separation coming out of the duoplasmatron source, with common elements used as example beams.

2.1.1.5 Main Acceleration Column

The main acceleration column is the heart of any accelerator system. In this area the beam is exposed to very high voltages, resulting in the acceleration of the ions

to their desired energy. The maximum terminal voltage is often the metric used to define an accelerator system, such as the 1.7 MV tandem system being discussed in this section. A schematic of the main acceleration column can be seen in Figure 2.5. This graphic should aid in understanding the system as it is described in this section.

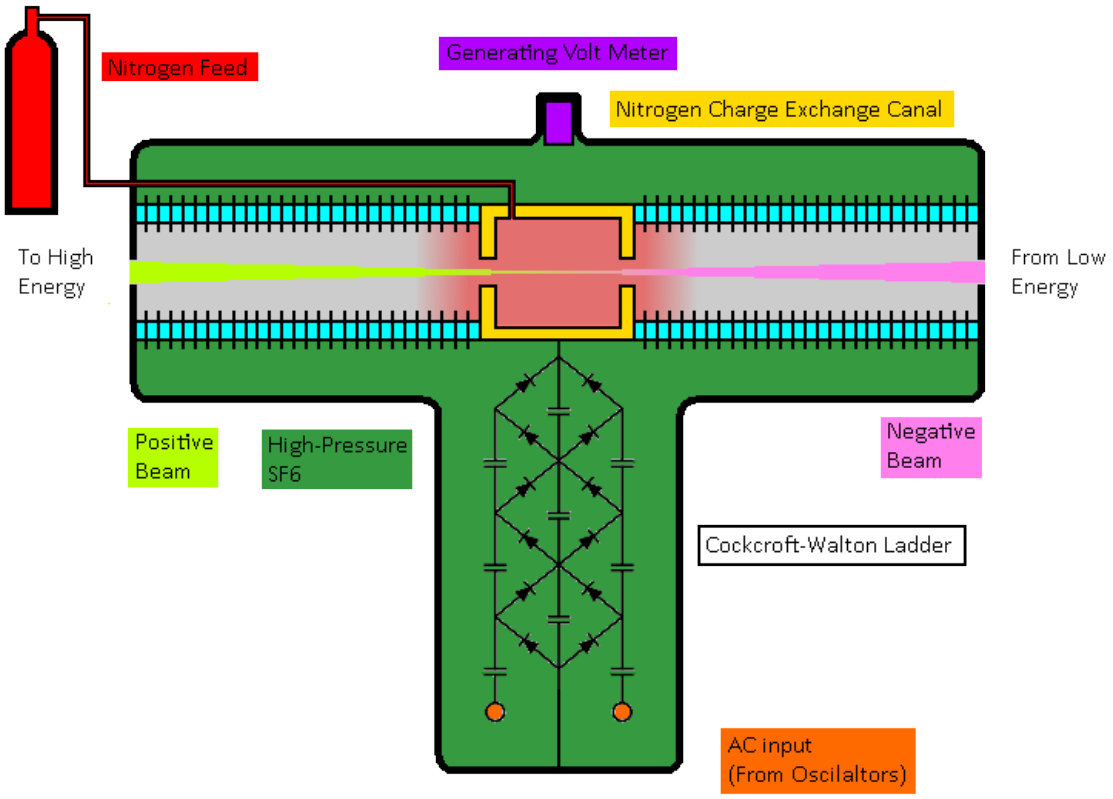

Figure 2.5: A schematic of the internal structure of the main acceleration tank.

The term "tandem" for this system is derived from the positioning of the two acceleration columns that this setup contains. The columns are positioned such that the beam passes through one column and then another. Such a configuration of any

two objects is known as a "tandem" setup (Ex. Tandem bicycle). Each column is a series of O-shaped metal plates separated by ceramic tubes and connected to its' directly adjacent neighbors by a series of high-value resistors. Suspended between these two columns is the nitrogen stripper canal where the vital charge-exchange operation takes place. The accelerator produces a high voltage via a Cockcroft-Walton ladder which is driven by a pentode-based push-pull AC circuit. This high voltage is transferred to the beam at the stripper canal while the two supporting acceleration columns are grounded at either end.

The high voltage applied at the stripper canal can be read in two different ways. One way is remotely by a generating voltmeter (GVM). Another method is by measurement of the voltage across the first few isolation plates, and then extrapolating to the terminal voltage. With the exception of the push-pull circuit, all of the high voltage generating equipment, stripper canal and two acceleration columns are encapsulated within an isolation tank approximately 3 ft in diameter filled to 100 psi with sulfur hexaflouride (SF_6). This insulating gas is used to prevent discharge to ground, and is pressurized to a high value to increase the effectiveness and prevent the encapsulating tank from being prohibitively large. All of this equipment works together in order to perform the vital task of accelerating the ions provided from the sources to a high-energy for use in scientific experiments.

The main acceleration column is kept under vacuum by turbo pumps at either end. On the high energy end, a 1500 l/s turbo pump is used, backed by an oil-free scroll pump. The low energy end is pumped primarily by one of the three 1000 l/s turbo pumps mentioned in the low energy section. The higher-pumping speed turbo is used at the high-energy end because it is more important to have a lower pressure on the high energy end than the low energy end. This is to reduce the amount of beam neutralization after the ions have been fully accelerated. The oil-free pump

has been chosen for the high-energy end to mitigate the amount of oil contamination on samples in any target chamber.

In order for this system to accelerate at all, there needs to be a charge exchange in the middle of the two columns, otherwise any acceleration gained in the first column will be canceled by the deceleration in the second column. The process starts at the low energy end. The main acceleration column is given negatively charged ions from either of the two source heads. These negative ions are attracted to the positively biased terminal, accelerating along the first column. Once they reach the center they enter the charge exchange canal, which has a relatively high pressure of nitrogen gas. This gas is fed in at a very slow rate, controlled by a leak valve from outside the tank. The negative ions will interact with this gas, which will strip electrons from the ions. Many ions lose two or more electrons and become positive. These now positive ions will be repulsed by the positive terminal voltage and accelerate away, down the second beam tube, gathering even more energy.

This system, while complicated, does provide many benefits. First, this system offers a safer alternative to single ended-air insulated machines. The system high voltage is entirely contained within the isolation tank, rendering it incapable of causing harm to any technicians or research scientists using the machine. This setup is also convenient for producing high energy beams without an excessively high terminal voltage. On this system, a single charged ion emerging from the main acceleration column has the same energy as a double charged ion would have on a single ended machine with the same terminal voltage. This allows higher energies than is possible with a single-ended machine of the same terminal voltage. The preferred charge state, and therefore the energy can be optimized by controlling the level of nitrogen gas in the stripper canal. For instance, if higher charge states are desired, a heavier gas load can be used, enhancing the creation of multi-charge state ions.

It should be noted that this charge state bias is performed without modification of the source head parameters. The tandem setup is also easier to maintain. Since the column is grounded at both ends, the source head systems can be located at ground potential, making them much more accessible when compared to being located inside the main isolation tank. This also greatly aids in source head testing, maintenance and repair.

While the tandem column setup does have many advantages, it has a few disadvantages as well. First, ultimate beam currents are lower when compared to single ended machines. This is inherent to the charge exchange process. The nitrogen stripping canal will cause significant beam loss inherently in the process. For example, for the General Ionex 1.7 MV tandem, a single charged helium (He) beam has about a 30% transmission efficiency. This means that only ≈30% of the beam current that enters the main acceleration column will come out of the other end as single charged helium. This is one of the highest charge exchange efficiencies achievable. Heavier ions have much worse efficiencies. Another commonly run beam in this accelerator is double charged iron (Fe). For this beam, efficiencies are typically 10-15%. The tandem column setup also has difficulty in running certain ion species. In order for the tandem accelerator to produce a beam of a given element, the element must be able to be negatively and positively charged relatively easily. This fact alone makes it nearly impossible to run elements such as cesium (Cs) or krypton (Kr), both of which cannot hold a negative charge long enough for them to be accelerated to the terminal. This setup then limits the elements that are able to be produced by the tandem accelerator compared to a single-ended system.

2.1.1.6 High Energy

The high energy equipment encompasses all systems after the main acceleration tank. This includes the high-energy beam optics and the various target chambers located on the accelerator. The high energy beam optics are very important for directing the beam as well as controlling its shape. After the beam traverses the nitrogen stripper canal, located on the main acceleration column, it will become less focused. This unfocused beam is then passed through a quadrupole focusing element to shape the beam. Properly shaped, the beam continues to the high energy magnet which directs the desired energy beam to the correct beam line. For the 1.7 MV tandem there are three chambers available: the ion beam analysis (IBA) chamber, the implantation chamber, and the channeling chamber. Each chamber is tailored to perform certain tasks which will be discussed in their respective sections.

The high energy end is kept at high vacuum by a mixture of turbo pumps and ion pumps. Each chamber is equipped with a 1000 l/s turbo pump backed by an oil-free scroll pump. The turbo pumps are used here due to their A) very fast pumping speed, which helps reduce chamber cycle time, B) their small size profile, which reduces the amount of space required between beam lines and C) their inherent cleanliness which, together with the oil-free scroll pump, helps reduce the amount of sample contamination. The ion pumps are used on the beam lines for the ion beam analysis chamber and the implantation chamber. These pumps are used since they are very simple, require no backing pumps, can be left on indefinitely, and provide very good beam line pressures. Beam line pressure is especially important to keep low, since a poor beam line pressure will result in a large amount of beam neutralization. The neutralization problem is especially pronounced in the beam line since the beam path length within that section is quite high when compared with

other zones, such as the chamber.

2.1.1.7 High Energy: Beam Optics

The beam is sent initially from the main acceleration column through an X-Y focusing quadrupole. This element is designed to be able to focus a divergent beam in the vertical and horizontal directions independently, resulting in not only a more focused beam, but a beam with a controllable shape. After the beam has been shaped by the quadrupole, it enters the high-energy bending magnet. This magnet, like the low energy magnet, performs several important tasks. First, it is used to direct the beam down the beam pipe to the chamber to be used for the experiment. This magnet also performs the vital function of performing energy filtering of the beam. Due to the creation of many charge states in the nitrogen stripper canal, the beam emerges from the main acceleration column as a mixture of ions with different charge states. Since the low energy magnet has already purified the beam down to a single element, only the charge state, and therefore the ion energy, will differ between elements. By altering the strength of the magnetic field, different charge states, and therefore different energies, can be selected. It is important to note that the single charged beam, even though it has the least energy, will require the highest magnetic field to bend to a given angle. Multi-charged ions, even with their higher energy are easier to bend since the multiple charge state will enhance the magnetic field's effect. With the beam energy now selected by the high energy magnet, it is sent to a chamber to be used for experimentation. A schematic of the high energy beam optics can be seen in Figure 2.6

2.1.1.8 High Energy: Ion Beam Analysis Chamber

The ion beam analysis chamber is able to hold multiple samples on a goniometer to perform a wide variety of sample analysis techniques. The chamber setup on this

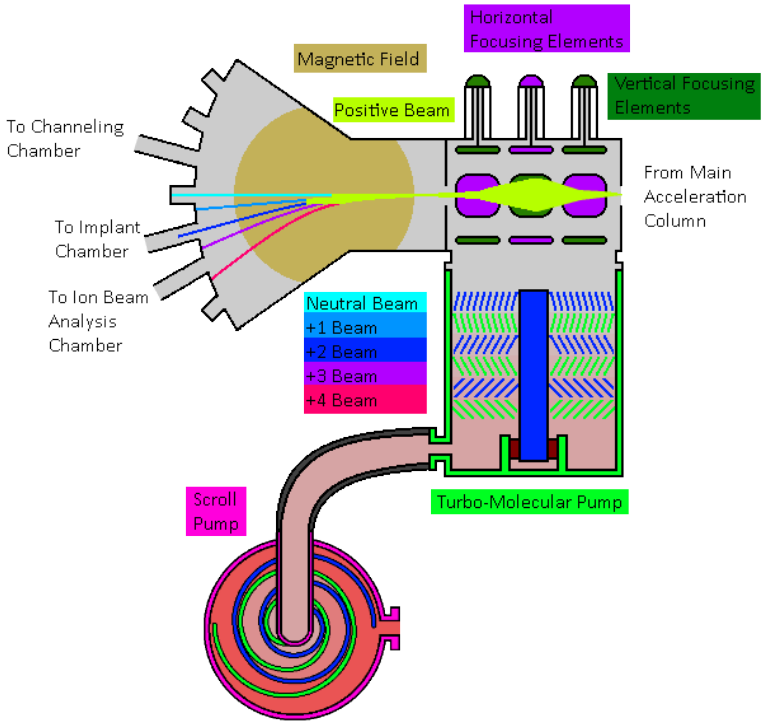

Figure 2.6: A schematic representation of the magnet and focusing elements located on the exit of the main acceleration column of the 1.7 MV tandem

accelerator is capable of performing Rutherford Back-Scattering (RBS) spectroscopy, Particle-Induced X-ray Emission (PIXE), Elastic Recoil Detection (ERD), and Nuclear Reaction Analysis (NRA) types of experiments. All of these techniques are used to determine very precisely the composition of the sample being analyzed. Each have their own strengths and weaknesses, necessitating the use of all techniques to be able to identify a wide variety of samples precisely. A schematic of this chamber, showing the relative positions of various detectors is shown in Figure 2.7.

This chamber has been placed on the left hand side 30 degree beam line. This angle was chosen in order to improve the beam energy resolution. A high magnet bend angle will help ensure that only a beam of a precise energy, with very little vari-

ation about that value, travels to the chamber. This is very important in being able to reduce measurement spread, improving measurement resolution and sensitivity. This angle is allowed since the ions used for analysis are typically very lightweight. Hydrogen (H), helium (He) and in rare instances, carbon (C) or silicon (Si) are the only beams that need to be sent to this chamber. Their low mass allows them to be bent to a high angle without having to generate a prohibitively large magnetic field.

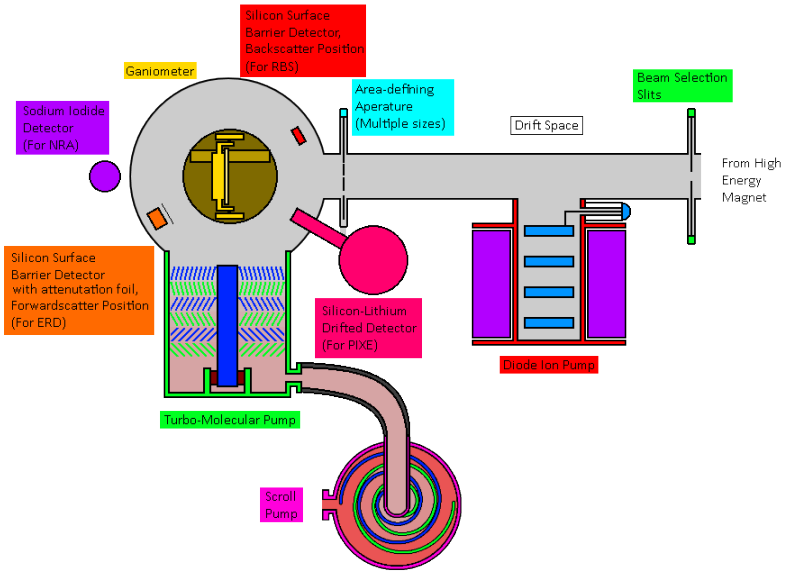

Figure 2.7: A schematic of the ion beam analysis chamber showing relative positions of detectors.

2.1.1.9 High Energy: Implantation Chamber

Another chamber used frequently is the implantation chamber. This chamber is equipped with a room temperature or heated stage, and is setup to perform a uniform implantation on samples up to 15 x 15 mm in size. It does this by having a set of raster coils located approximately 1 meter before the chamber. These coils are

able to effectively scan a focused beam spot over the entire sample surface, resulting in uniform depositions. The heated stage is capable of maintaining samples at a temperature up to 600 °C for ion implantation at a high temperature. Due to this high heat load in the chamber, a water-cooled shroud is installed around the heated stage to help reduce the heating of the chamber. A schematic of the chamber, with the heated stage displayed, is shown in Figure 2.8.

This chamber is installed on the left hand side, 11 degree beam line. This smaller angle has been chosen to allow for heavier, higher energy ions to be implanted. For example, many steels are irradiated at this facility. Iron (Fe) then is the ion of choice to mitigate the amount of chemical changes that will occur within the steel. This element helps produce good quality samples from experiments, however, it is a heavy ion to bend in the high energy magnet. By reducing the angle required to bend the ions, the magnet load can be reduced to a reasonable level. For this magnet setup, 30 amperes of current are typically required to be able to bend the iron beam to the implantation chamber. By comparison, it would require nearly 90 amperes of current to bend the same beam to the ion beam analysis chamber. This current draw is prohibitively large, showing the importance of choosing a beam line with a small bend angle.

2.1.1.10 High Energy: Channeling Chamber

The channeling chamber is used for one specific type of experiment: RBS channeling. This is a specific type of RBS analysis that uses single crystal samples. The chamber is equipped with a high-precision goniometer that is automatically controlled through a custom-coded labview program. This goniometer is controlled to precisely align the single crystal channeling axis with the beam. This allows ion channeling to take place, allowing unique measurements to be made that can reveal

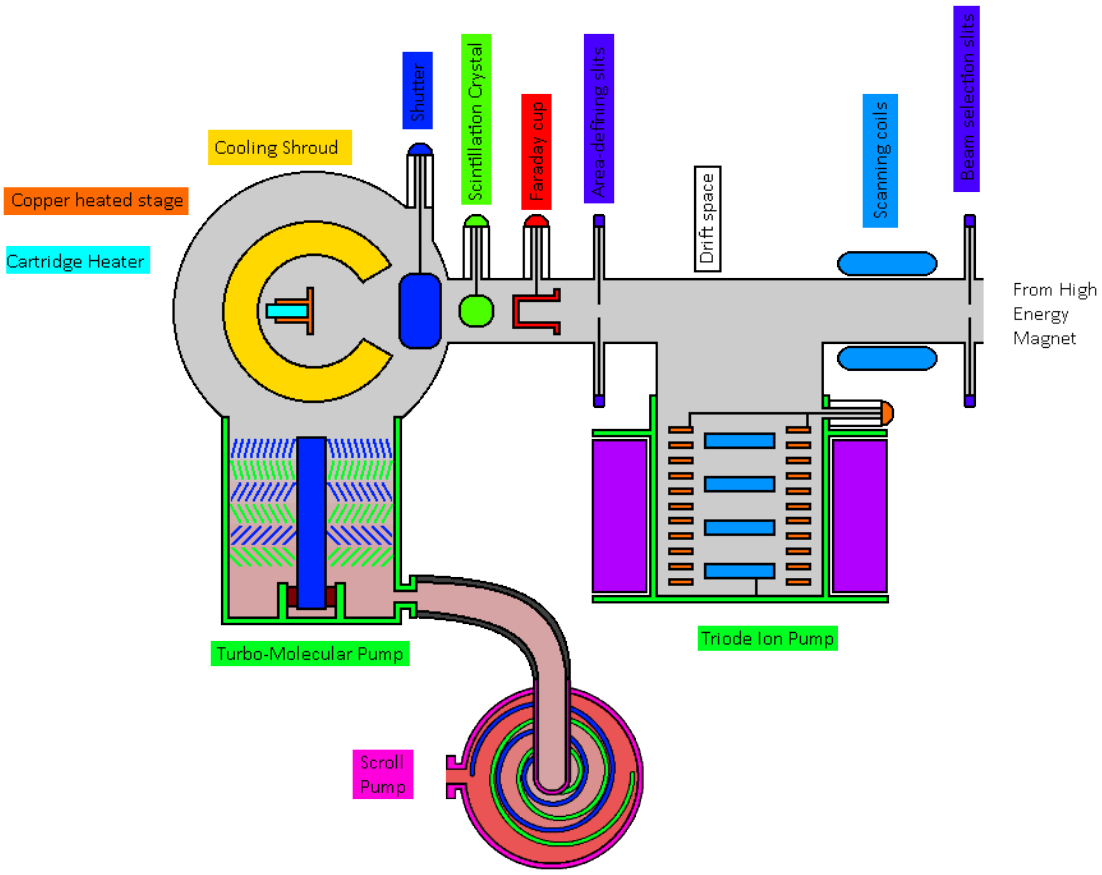

Figure 2.8: A schematic of the implantation chamber showing stage geometry and cooling shroud.

details about the internal structure of the sample. This chamber is separate from the general IBA chamber due to the need to have the high-precision goniometer. A schematic showing the chamber and beam line setup can be seen in Figure 2.9.

2.1.2 140 kV Implanter

The 140 kV implanter system is an accelerator put together from various parts and is not from a specific company. It is a relatively simple, but robust system. A schematic showing the overall structure can be seen in Figure 2.10. It has a single gas source head which sits on the end of the primary acceleration column. This column

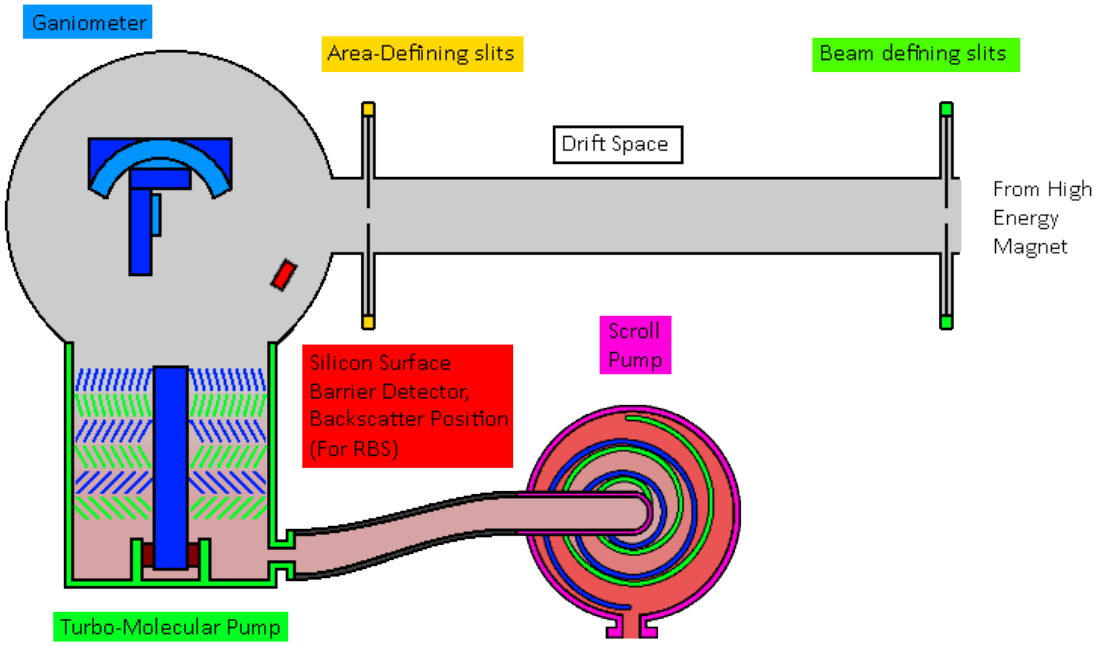

Figure 2.9: A schematic representation of the channeling chamber showing goniometer and detector positions.

is a relatively low voltage, and as such is air insulated. This system uses a single magnet which bends the desired beam to a single end station. This system is best segmented into three parts: the source, acceleration and filtering, and end station. These parts will be discussed in more detail in separate sections.

2.1.2.1 Source

The source head for the 140 kV system is a gas fed source head capable of producing very high beam currents. The source head structure is a mostly closed cylinder with a small opening at one end. Inside this cylinder is a tungsten filament. This filament is heated to a very high temperature by passign electrical current through it to generate free electrons. Gas is injected into this cavity, and due to the wealth of electrons, forms a plasma. To form and sustain this plasma, there are two other

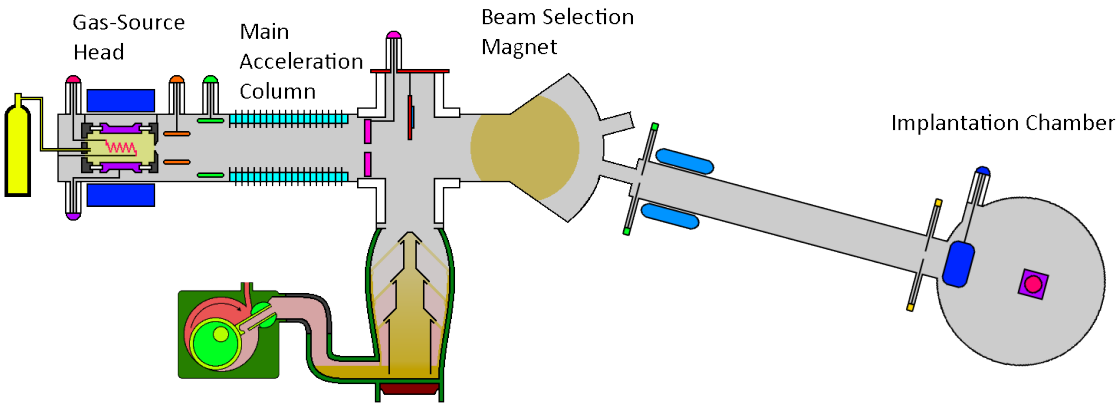

Figure 2.10: A schematic representation of the 140 kV implanter.

elements that help confine and shape the plasma. First, the entire source head is surrounded by an electromagnet. This magnet primarily confines the thermal electrons, making them travel in a long spiral path, increasing the chances of the electron interacting with a gas atom, and causing ionization. The second confinement element is the anode. This element generates a bias between the cylindrical wall of the source head cavity and the filament, the aperture plate and back wall of the source head cavity, which are all held at local ground potential. The setup may be more easily understood from close examination of the source head in Figure 2.11. This voltage bias is designed to help confine the plasma that has been generated. This enhances the amount of ions extracted from the plasma, as well as helps with the beam shape. With the plasma generated in the source head cavity, the extraction bias then extracts the positively charged ions from the source head. The beam then immediately passes through a focusing lens to help correct for the beam shape. The beam is now ready to enter the main acceleration column.

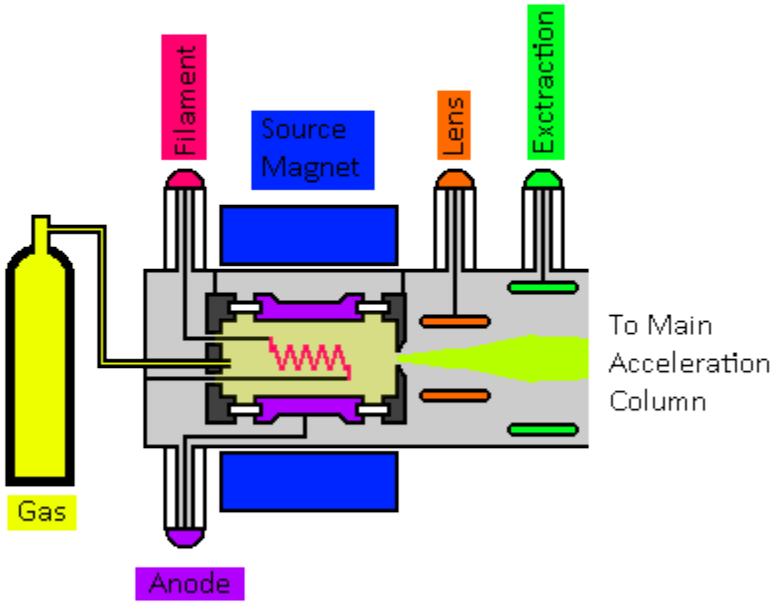

Figure 2.11: A schematic representation of the 140 kV implanter's gas source head.

2.1.2.2 Acceleration and Filtering

After the beam is produced and shaped by the source head, it immediately enters the main acceleration column. The source end of the column is held at the operating voltage, and the other end is grounded. This configuration is known as a single ended accelerator, and, as mentioned before, is quite simple, robust and straightforward. A diagram of the acceleration and magnetic filtering components of this accelerator can be seen in Figure 2.12.

This accelerator design has the advantage of losing none of the beam in a charge exchange process, and only requires a single acceleration column. The disadvantage of this system is that the source and associated power supplies all have to be held at the operating voltage. This accelerator has a relatively low terminal voltage, and so is air insulated, making maintenance a relatively simple task. However, for higher

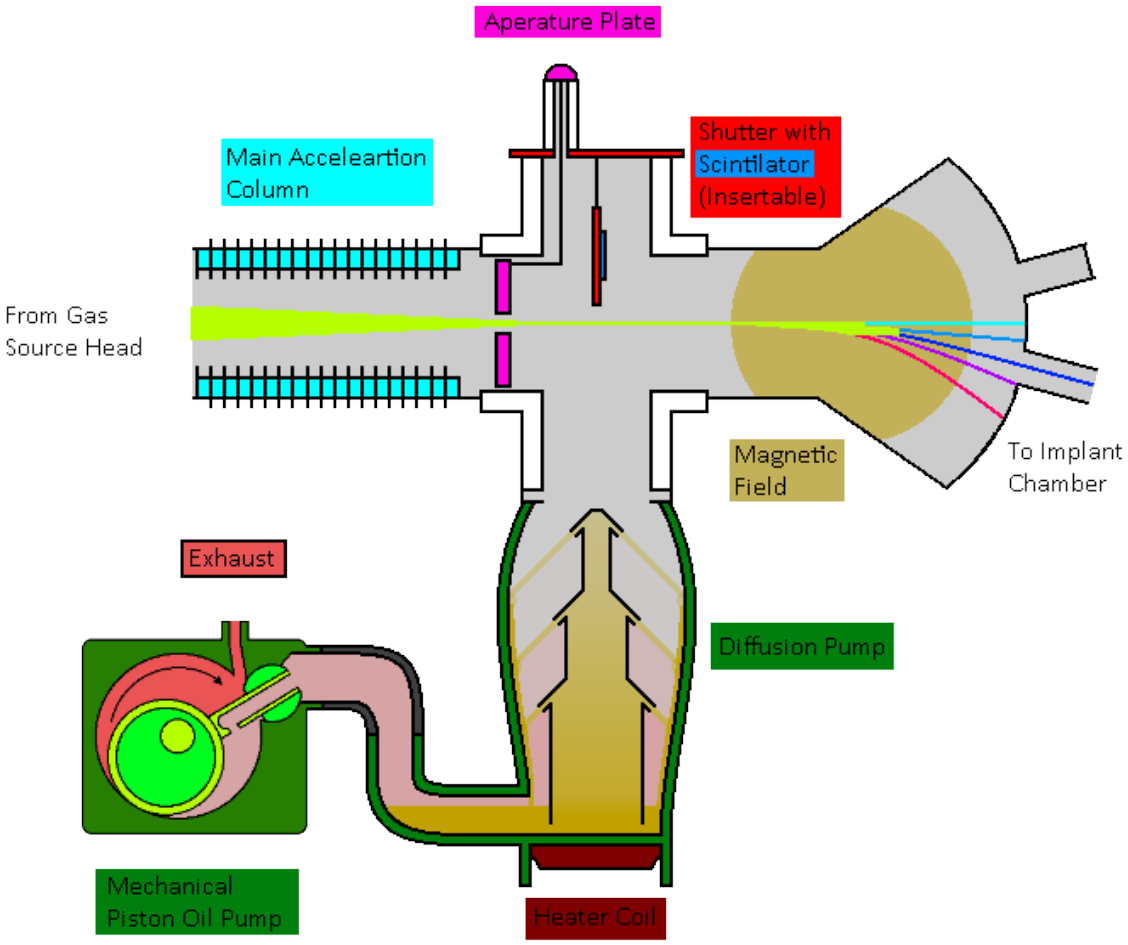

Figure 2.12: A schematic representation of the 140 kV implanter's main acceleration column and ion filtering magnet

voltage systems which require an isolation tank around the source end, performing any sort of work on the source head or supplies requires venting the tank and re-filling it after the work has been completed. This process is time consuming and must be undertaken with the utmost precaution as to keep the fill gas pure. This is a major disadvantage for high voltage single-ended systems.

After the beam is accelerated through the main column, it is sent to a single bending magnet. This magnet bends the beam to travel down the beam line to the

target chamber and provides the majority of the horizontal adjustment in the system. This magnet has to filter the beam for both energy and mass simultaneously. This is a simpler setup, but users must be very wary of closely spaced ion species, such as oxygen and nitrogen beams, as well as beams that are unresolvable since they have the same charge over mass ratio.

The source end of the accelerator is kept at high vacuum by a diffusion pump backed by a mechanical oil pump. The diffusion pump is kept at ground potential, directly after the main acceleration column, but before the bending magnet. This setup has been chosen because the diffusion pump available for this system has a very high pumping rate. This is needed due to the large gas load produced by the source head while it is operation. The disadvantage of this pump is that it contaminates the system with oil. The effect of this is partially mitigated by a water cooled collar at the top of the diffusion pump. This disadvantage is acceptable since this diffusion pump is located far from the target chamber and has a very low oil back-streaming rate when the system is at operating pressure. This pump is backed by a high-throughput mechanical oil pump in order to keep pace with the very large diffusion pump in use. The mechanical pump has another advantage of a robust design that will operate for decades with very little maintenance. An oil backing pump is acceptable even though it back-streams oil for the same reasons as mentioned for the diffusion pump.

2.1.2.3 Target Chamber

Before the beam reaches the target chamber it must travel down the implantation beam line. A diagram of the beam line and target chamber can be seen in Figure 2.13.

This beam line is equipped with a beam profile monitor and scanning coils. These coils are used to raster the beam onto to a maximum 3 x 3 cm area. This large area is

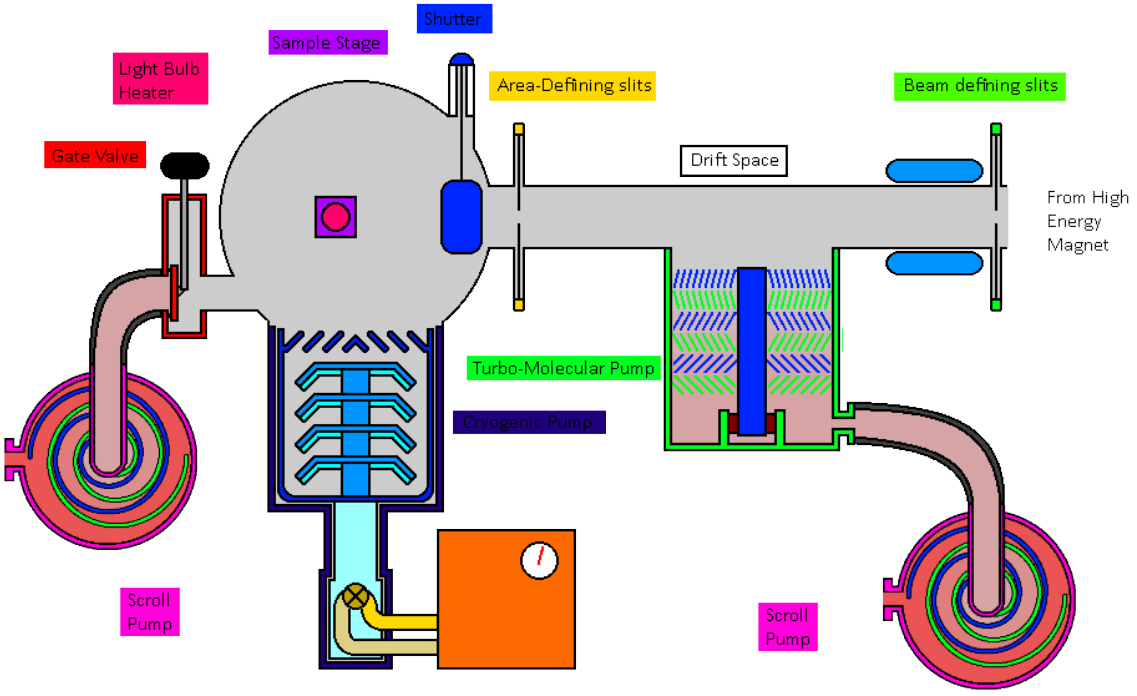

Figure 2.13: A schematic representation of the 140 kV accelerator implantation chamber showing stage position and geometry

possible from the wide bore beam pipe diameter utilized on this beam line. This large pipe is more challenging to pump to high vacuum but allows for large sample area irradiations. The beam line is equipped with a small sized turbomolecular (turbo) pump backed by an oil free scroll pump. This setup is used to reduce the amount of oil contamination seen by the samples in the target chamber. A large sized pump is not required since the diffusion pump is able to handle most of the gas load.

The target chamber equipped on this accelerator is used exclusively for implantation. It is equipped with a heated stage which can achieve temperatures up to 800 °C. This stage is flexible in position as it has 5 cm of travel, allowing for multiple sample mountings and can be rotated to offer glancing angle irradiations. The stage is also electrically isolated from ground, allowing a current integrator to be used for

room temperature irradiations, providing precise dose measurements.

The chamber is kept at high vacuum by a cryo-pump. This pump was chosen due to its very high pumping speed of most gasses, its very clean nature, and its ability to achieve very good vacuum levels. The cryo-pump does have one serious disadvantage in that it must be periodically regenerated. This is due to the nature of the pump not exhausting gasses. The pump simply traps and stores gasses until it is full. At that time the pump must be taken off line and allowed to heat up to let the trapped gasses escape. The cryo-pump is not backed by a roughing pump since it has no exhaust, however, the chamber must be still be taken to roughing vacuum before the cryo-pump takes over. To perform this task, an oil-free scroll pump is used to mitigate chamber contamination.

2.1.3 Electron-Beam Evaporator

The Electron-beam (E-beam) evaporator is a device used to very precisely deposit a thin film of material onto a given substrate. The device consists of a few different components housed inside a high-vacuum chamber. This chamber is kept at a high vacuum by a turbo pump with a dual stage rotary vane oil pump backing it. The high vacuum is required to maximize deposited film purity as well as allow the heat source, a beam of low energy electrons, to function properly. Samples to be coated are placed in the chamber on a platter located at the top of the chamber. The platter face holding the samples faces downwards, so samples must be held in place by adhesives, such as tape, or a clamp, several of which are available on the sample platter. This platter is shielded by a movable shutter. Next to the platter is a quartz crystal. This crystal is used to determine film thickness through vibrations. As a film layer builds up on the face of this quartz, its overall mass will increase. Then, similar to a pendulum, the frequency at which it oscillates will decrease. The

measured decrease in frequency can then, knowing the density of the material being deposited, be used to calculate the deposited thickness to a high precision. The bottom of the chamber holds the heat source and deposition material. Both of these are kept under a different protective shutter. A schematic of the system can be see in Figure 2.14.

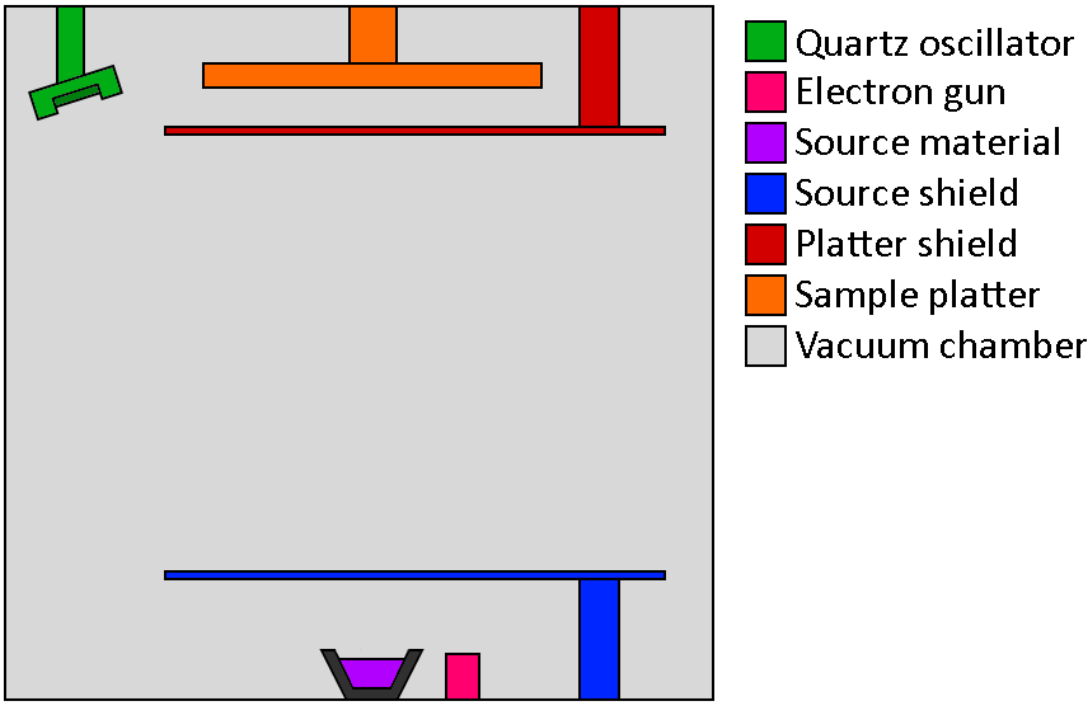

Figure 2.14: A schematic of a typical E-beam evaporator showing all critical components.

To begin a deposition, both shutters are closed and the heat source begins melting the material. The electron beam is initially set at at low power to try and evenly heat the sample. After a user defined amount of time, the intensity of the electron beam sharply increases, melting the near-surface material. Once the material has

been determined to be adequately heated and the surface oxidation removed, the shutter at the bottom of the chamber opens. With the bottom shutter open, the vapors being produced by the melted material drift upwards and begins coating the quartz thickness measurement device. While measuring the rate of deposition, the heat source power is varied until the target deposition rate is reached. Once the target deposition rate is correct, then the sample platter begins spinning and shutter protecting the sample platter swings out of the way, beginning the deposition. The platter is spun in order to increase uniformity of the deposited layer. When the deposition is complete, the shutter at the top and bottom of the chamber close, halting the deposition.

2.1.4 Tunneling Electron Microscopy (TEM)

The TEM is a powerful instrument which uses an electron beam to be able to resolve micro and even nano-scale features from within a sample. To do this, the TEM uses an electron beam which is focused and directed through the sample. As the electrons pass through the sample, they are perturbed by the structure within. The beam is then expanded on to a detector array which is able to record an image of the resulting beam. This process is able to produce images of the interior of the sample, showing features such as crystal grains, dislocation loops, voids, and other microstructure features.

There are several important lenses and apertures which must work in concert to achieve proper beam shape and placement. The important beam shaping features of a TEM are outlined in Figure 2.15. For this study, diffraction patterns, bright field imaging, and dark field imaging are all required in order to fully understand the structure. The changes to the electron beam shape needed to achieve each of these imaging modes can be seen in Figure 2.15.

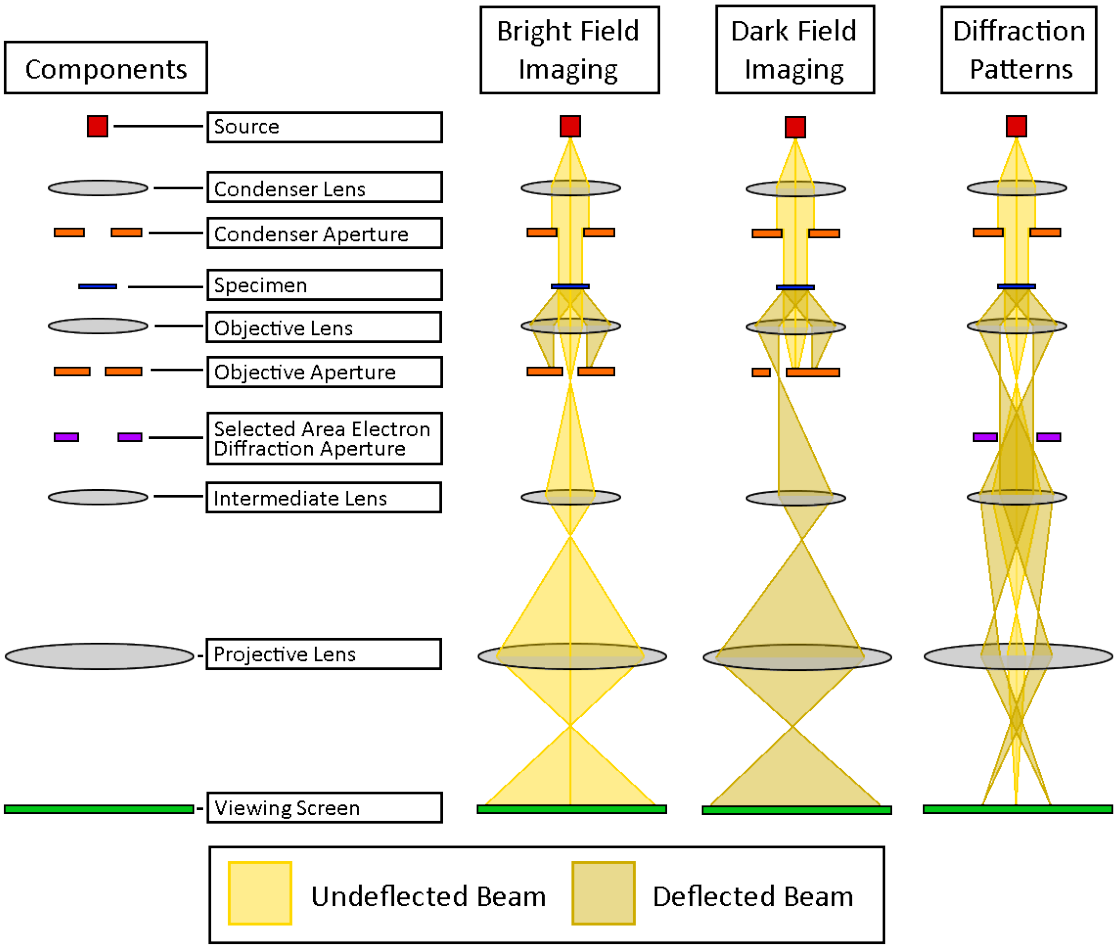

Figure 2.15: A schematic of the major components of a TEM. Also a diagram showing the differences in beam manipulation required to achieve different imaging modes.

Diffraction patterns form the basis for the imaging capabilities for the TEM. These patterns reveal a great deal about the overall or local structure of the sample, depending on the level of focus achieved. For a completely amorphous sample, the diffraction pattern will consist of the primary, or non-deflected beam, in the center and a diffuse, uniform, ring surrounding it. This ring is often referred to as a "halo" ring due to its resemblance to an angel's halo in traditional christian mythology. This pattern is formed since the amorphous structure tends to scatter the beam at

the same angle and does not have a directional dependence. An example of this structure can be seen in Figure 2.16A. For a single crystal sample, the diffraction pattern formed will consist of a regular arrangement of dots, surrounding the main, non-deflected beam. These dots are caused by the crystal structure preferentially deflecting the beam into certain crystallographic directions. This makes the diffraction pattern very useful in determining the overall crystal structure as well as atomic spacing between the atoms contained within the crystal structure. An example of a single crystal diffraction pattern can be seen in Figure 2.16C. A poly-crystalline material will contain many of these dot patterns superimposed on each other, around the primary beam spot. An example of a polycrystalline material can be seen in Figure 2.16B. This happens since each of the crystals in the analysis beam will contribute to the overall diffraction pattern. For the metallic glass, there will be a combination of amorphous and polycrystalline structures leading to diffraction patterns which can range from only having a diffuse halo ring in an amorphous sample, to a halo ring plus some scattered points in a partially crystallized sample, to only having scattered points in a fully crystallized sample. An examples of a partially crystalline diffraction pattern can be seen in Figure 2.17.

Bright field imaging is the standard imaging mode when using a TEM. In this mode, the image is created from the non-deflected electron signal by selecting the main beam from the diffraction pattern. This mode of imaging will show overall structures of the sample as well as give information about local sample density or sharp changes in composition. An example of this type of image can be seen in Figure 2.17.

Dark field imaging is a variant type of imaging which creates an image from the deflected electron beam. This style of imaging is very important to theses studies as it is very sensitive to crystallographic direction. By selecting only the deflected

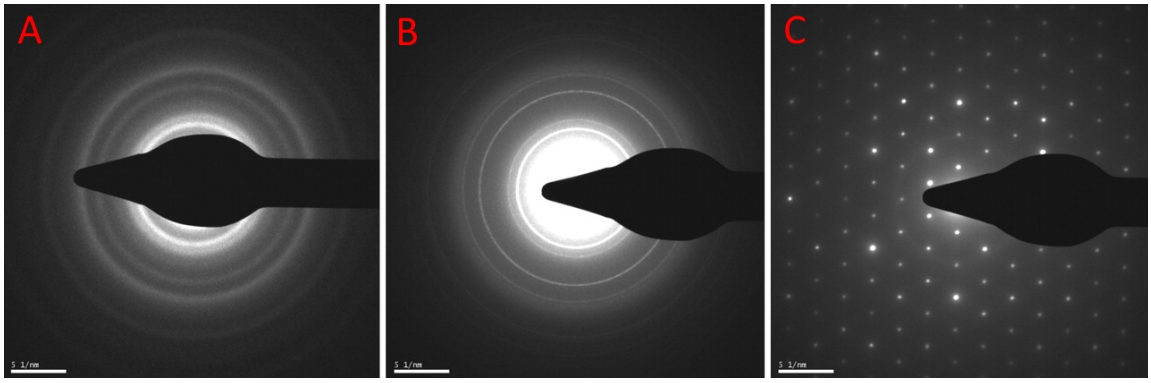

Figure 2.16: Examples of diffraction patterns from A) Amorphous carbon, B) Polycrystalline aluminum and C) Single crystal gold. Taken from Lobastov *et.al* [2]

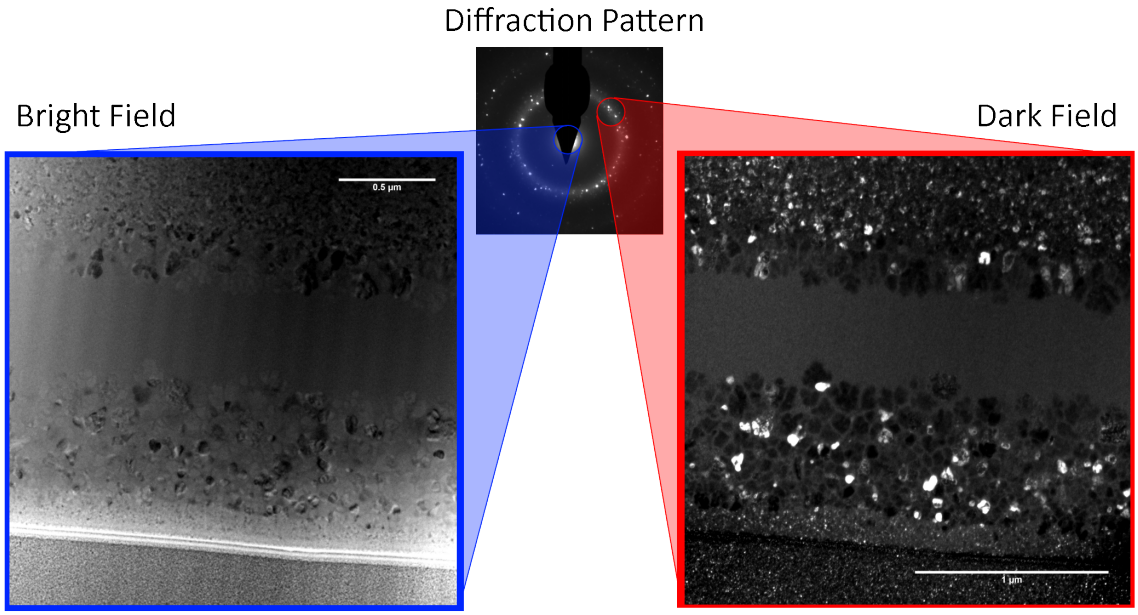

Figure 2.17: Example micrographs showing the relationship and different capabilities of bright field, dark field, and diffraction pattern images.

electrons, crystals with that preferred orientation will light up very brightly, while crystals out of that direction will become very dark. Amorphous material shows up as a uniform gray. Due to this strong contrast, this technique is most sensitive to

crystallization and can reveal the presence of nano-crystals even when bright field imaging and diffraction patterns appear to show a completely amorphous material. An example of dark field imaging can be seen in Figure 2.17.

While, TEM is a power full analysis tool, it does require a sample to be electron transparent. This means creating a sample that is 100-200 nm thick, which is quite challenging. The three methods used to create samples for this study are outlined in the following sections.

2.1.5 Focused Ion Beam (FIB)

The focused ion beam system is a relatively new tool in the suite of electron microscope characterization techniques. This instrument combines a traditional SEM with a high-precision goniometer, sample manipulator, platinum (Pt) deposition system and a well focused source of low-energy gallium (Ga) ions. Theses tools, when used together, give unprecedented control for microstructure fabrication of various types. By selectively sputtering the sample using the Ga beam, a variety of sample shapes and sizes can be created with characteristic dimensions ranging from $\approx$50 nm to $\approx$50 μm.

The FIB has many applications, but is commonly used to create micro-pillars for mechanical testing or electron transparent films for TEM characterization. In this study the FIB was used to create TEM ready specimens out of previously-irradiated MG samples. The ability of the FIB to reliably create high-quality electron transparent samples of various sizes from specific sites in the sample lends great flexibility in TEM characterization. To produce these samples there are many steps that have to be undertaken to ensure that the sample is made to the correct size and is thin enough to be viewed easily in the TEM. A pictorial representation of the process can be found in Figure 2.18.

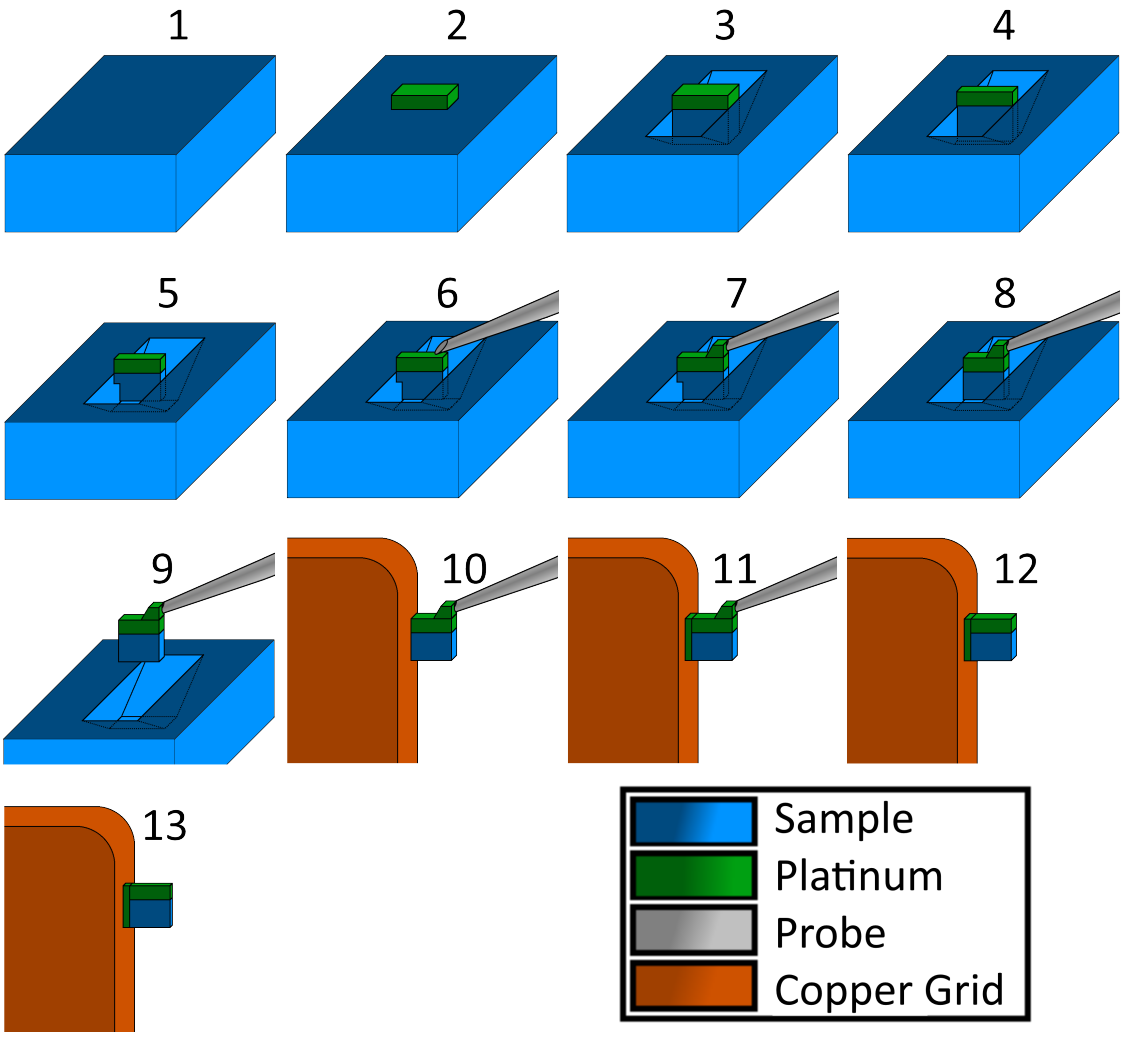

Figure 2.18: A pictorial representation of the lift-out process used to create electron-transparent specimens from focused ion beam milling.

To begin, a suitable spot on the sample is found. Ideally, a flat area away from any irregular features such as surface cracks, or obvious surface contamination. Next a platinum "pillow" is deposited on top of the sample. This layer is deposited to protect the sample surface from being etched away in the subsequent steps. Next, two trenches are cut on either side of the deposited Pt pillow using the Ga beam. The remaining material between the trenches will become the final electron-transparent

sample. With the trenching complete, rough sample thinning is performed, making the web of material thinner. After rough thinning has been completed, the Ga beam is used to cut around the sample to nearly detach the sample from the substrate. With the sample held on by only a small piece, a probe is brought over and welded to the sample through Pt deposition. With the sample now firmly attached to the probe, the Ga beam severs the remaining material holding the sample to the substrate. Next the sample is moved to a copper grid on the probe. Pt is again used to weld the sample to the grid, and the Ga beam is used to cut the probe from the sample after it is properly attached. Finally, the Ga beam on a very low energy and intensity, performs final thinning of the sample to make it electron transparent. The mounted sample can then be removed from the FIB and analyzed using a TEM.

2.1.6 Twin-Jet Electropolisher

Thinning samples to use in a TEM is a challenging task. As such there are many devices that have been developed to perform exactly that task. The Twin-Jet electropolisher performs that task by spraying acid onto a sample and applying a voltage to cause a controlled etching of the sample. In order to achieve consistent etching and good performance, all elements of the polisher have to work in concert.

The main components of the electropolisher are the: tub, pump, sample holder, electrode, power supply, laser and light sensing diode. The tub of the electropolisher is a double-walled, air insulated, plastic tub which holds the acids used to perform the etching. It is well insulated to aid in keeping the acids at a constant, low temperature. The pump rests near the bottom of the tub and circulates the acids up into the polishing head where they will react with the sample before traveling back down to the tub. The polishing head contains the sample holder, electrode, laser and light sensing diode and is the location where the actual polishing happens. The holder

positions the sample in the proper position from the electrode which is fed by the external power supply. Lastly, the laser and light sensing diode are held on opposite sides of the sample.

To operate, the tub is first filled with acid and cooled using liquid nitrogen to the appropriate temperature. The sample is then loaded into the holder and placed into the polishing head. The power supply settings are adjusted by the user and then the polishing begins. When the user starts the polish cycle, the pump runs first by itself for a few seconds to allow for a good stream of acid to develop on the sample. Next, a voltage is applied to the electrode and the laser turns on. At this point the power supply will register a high current value as the sample begins to etch. The etching process will continue until either the power supply is deactivated by the user, or the light sensing diode registers laser light above the set threshold value, indicating that the sample has thinned through. After the sample is removed, it is rinsed in an acetone bath, then a De-Ionized (DI) water bath before inspection. A sample with several small holes near the center of the material indicates that a high-quality thinning has been achieved, giving a good chance of electron transparent regions.

2.1.7 Traditional TEM Sample Preparation

The very first forms of preparation used to produce electron transparent samples implemented a fairly straightforward, albeit difficult to perform, process. This process requires three primary pieces of equipment: a standard flat grinding disc, a precision dimpler and an ion mill. Example pictures of these three pieces of equipment can be seen in Figure 2.19. To produce high quality samples using these three pieces of equipment is quite challenging and requires lots of time, patience and expertise. However, this method of preparation is quite versatile and can be applied to many samples that could not be prepared using FIB or electropolishing. A pic-

torial representation of the process can be seen in Figure 2.20, and a more detailed description of the process is continued in the next few paragraphs.

Figure 2.19: Images of the equipment used in traditional TEM sample preperation

To begin, the sample is cut into two pieces, and the faces of interest are glued together. Next, this sandwiched sample is mounted onto a polishing rig and wet sanded perpendicular to the surface using standard silicon carbide (SiC) based sandpaper until it is around 1 mm thick. Next, the sandpaper is swapped for diamond paper placed onto a smooth glass surface, and the sample is switched from the original polishing rig to a high-precision grinding apparatus. The sample is then wet sanded on the diamond paper on both sides to ensure that the two sanded surfaces are nearly exactly parallel. This sanding is done until the sample is $\approx$300 μm thick.

Next, the sample is transferred to a dimpling machine. This machine uses a small wheel to grind an impression into the sanded surface, centered about the glued surfaces of the sample. Initially a copper wheel is used with a small amount of abrasive material, usually an alumina (Al_2O_3) slurry. This will quickly grind a depression into the surface. After the depression is mostly made, the copper wheel is exchanged for a cotton wheel. This wheel is coated with a finer abrasive material. The wheel then

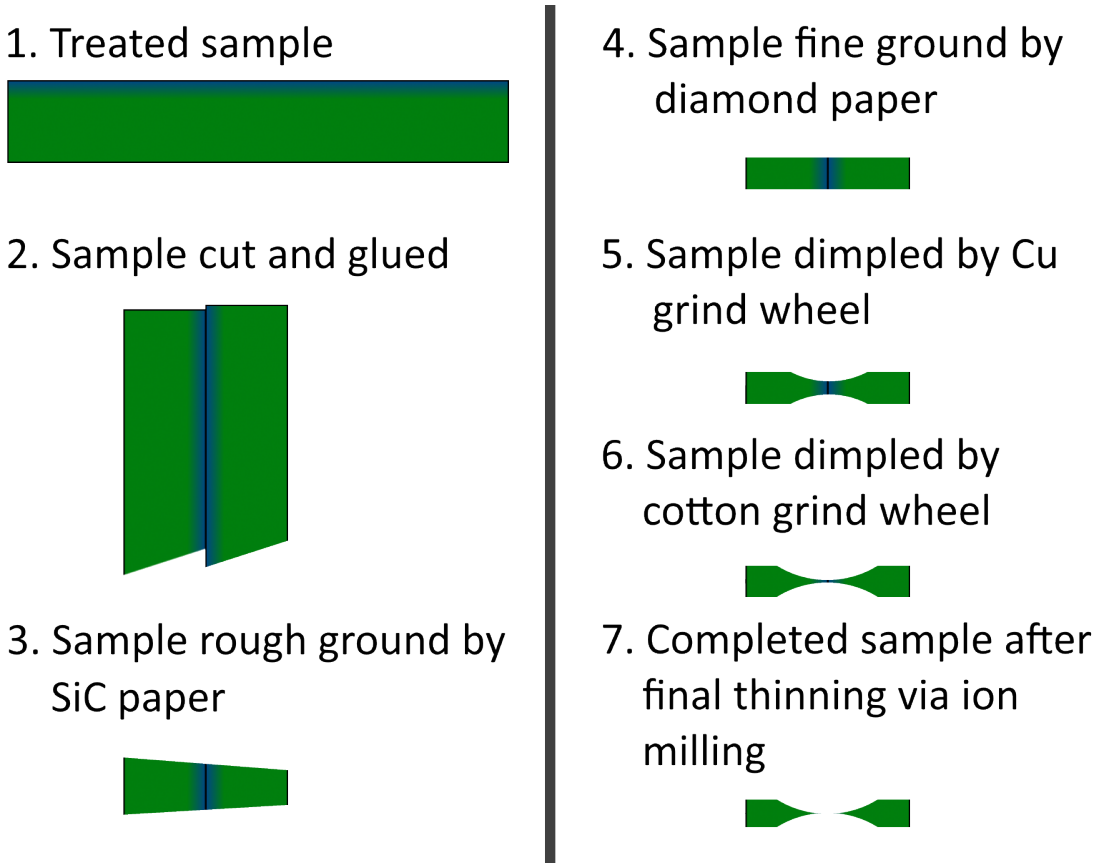

Figure 2.20: A pictorial representation of the sample evolution when using traditional grinding, dimpling and ion milling to produce electron transparent samples.

continues deepening the depression until the sample reaches a thickness of around 20 μm in the center of the depression.

With the center of the depression adequately thinned, the sample is moved to the ion milling machine. In this final step, the sample will be thinned to electron transparency by using low energy argon (Ar) atoms to sputter the surface. Two directly opposed beams of Ar are created which hit the sample at a glancing angle of approximately 10°. The sample is rotated during bombardment to ensure uniform sputtering. This process is continued until the center of the sample is optically transparent. At this point it is known that around the edges of the perceived hole,

there will be wide electron transparent regions to be observed.

2.2 Techniques

2.2.1 TEM Sample Preparation

In the equipment section three different systems were discussed that were capable of producing electron transparent samples: FIB, jet electropolishing and traditional TEM preparation. Each technique was used in this study to fabricate specimens based upon each samples' unique properties and needs. A table outlining the techniques strengths weaknesses and usage in this study are shown in Table 2.1.

Table 2.1: Comparison of the three different types of TEM sample preparation used in this study

Preparation method	Advantages	Disadvantages	Samples Produced
Focused Ion Beam Milling	-High level of control over lift out location -fast fabrication time	-incompatible with insulating materials -Possible ion damage -small observable area	All bulk studies specimens
Jet Electropolishing	Large electron transparent regions -Very fast fabrication time -damage free method	Selective dissolution may occur -variable thickness membranes -lack of depth control	All studies involving thin films
Traditional Preparation	-Compatible with nearly all materials -Large observable regions	-Slow preparation time -Potential damage from: grinding, ion milling	Multi-layered sample study

For all bulk studies, FIB was used to prepare the sample. This method was chosen as it can reliably produce samples quickly post-irradiation. Traditional TEM preparation was not used due to the extremely difficultly presented by the sample's ribbon geometry. Jet electropolishing was also ruled out since it is only capable of producing planar view samples, not a cross-sectional view as was needed in this case.

Jet electropolishing was able to be used for the thin film studies since the samples were treated after the TEM preparation had been performed. This made the disadvantage of not knowing the depth of polish not important. In this case the variable thickness aided in performing the experiment since the effect of various membrane sizes could be observed.

Lastly, traditional TEM preparation techniques were used for the multi-layer samples since heterogeneous two material structure was incompatible with jet electropolishing and one of the layers was an insulating material, making FIB a non-viable method.

2.2.2 Ion Bombardment

It is important to discuss the parameters chosen to perform the ion bombardment studies as this is the sample treatment used in all of these studies. Ion bombardment is a very powerful tool in material analysis work, but it is not without its faults and drawbacks which must be carefully considered before designing an experiment or interpreting results.

2.2.2.1 Ion Selection

One of the major problems with ion bombardment is the fact that an actual atom is being introduced into the sample when causing damage. This is not an issue when damaging using electrons, photons or neutrons. From this, chemical changes can occur in the sample. In some cases, such as doping silicon for microchip devices, this

behavior is greatly desired. However, if ion damage is being used as a surrogate to study radiation damage in general, these chemical changes are to be avoided as best as possible. If an ion is not chosen properly, very extreme changes could occur which could cloud the damage caused by the radiation interaction. In order to avoid this, two types of ions can be chosen: Noble gases and self-ions.

Noble gas ions are perfect in that they do not form chemical bonds, therefore new compound formation will not take place. They are ideal for cases where a small change in composition could cause major issues or the sample has a heterogeneous structure. However, noble gasses can cause compressive lattice strain, and in some cases can move quite freely through the sample microstructure to create very large void structures. Noble gasses then are best reserved for cases in which the ion will likely pass completely through the zone of interest either depositing deeper or passing entirely through the sample.

The other choice is a self-ion. In this case, the ion element is chosen to match a major element in the sample of interest. For example, if a steel is being irradiated, iron (Fe) is often chosen in order to minimize the compositional change within the sample. While the entire sample is not composed of Fe, it is mostly made of that element, meaning that injecting additional Fe will not cause major chemical changes. This is not a perfect solution, but by performing calculations using the fluence and penetration depth, the change in composition can be predicted. At that point it can be determined whether or not the change is significant. For most irradiations the change in composition will be negligible. Self-ions then are a great choice in many cases where the sample is homogeneous, and void structures, or compressive strain caused by a noble gas is undesirable. In this study, the self-ion in each case will be given and the maximum change in composition will be provided if a self-ion is used.

2.2.2.2 Depth and Damage Determinations

When using ion bombardment to study radiation damage it is important to consider the fact that the damaging agent is a charged particle. Charged particles will have a maximum range in a solid determined by the electronic and nuclear stopping powers between the incident ion and the substrate. The interaction between the two can be quite complex as both stopping powers will be effected by the instantaneous speed of the ion relative to the substrate, the local substrate density and several other factors which have a negligible contribution most of the time. Creating a deterministic or analytic method to calculate the resultant ion distribution and energy deposition across a wide range of energies, ions and substrate compositions would be extremely challenging. In this case a different approach must be taken.

One common and elegant solution to this problem is to use Monte Carlo methods. The specific Monte Carlo code used to perform all depth calculations in this study is the Stopping Range of Ions in Matter (SRIM)[24]. Developed by James Ziegler and others, this code is considered to be accurate for a wide variety of compounds and incident ion energies. This code provides usable results by giving the user the average ion behavior as determined by simulating a large number of individual ion events. A snapshot of the program interface and results can be seen in Figure 2.21.

An ion in the code begins at one edge of a simulated sample at the energy specified by the user. It then travels into the sample losing energy as calculated by the electronic stopping power. It will travel in a straight line until it interacts with a nucleus and has a nuclear collision event. The distance traveled between events, as well as the scattered angle and retained energy from the nuclear scattering event, is determined by a statistical model developed by experimental testing combined with a random number generator. Once enough events have been computed, the aggregate

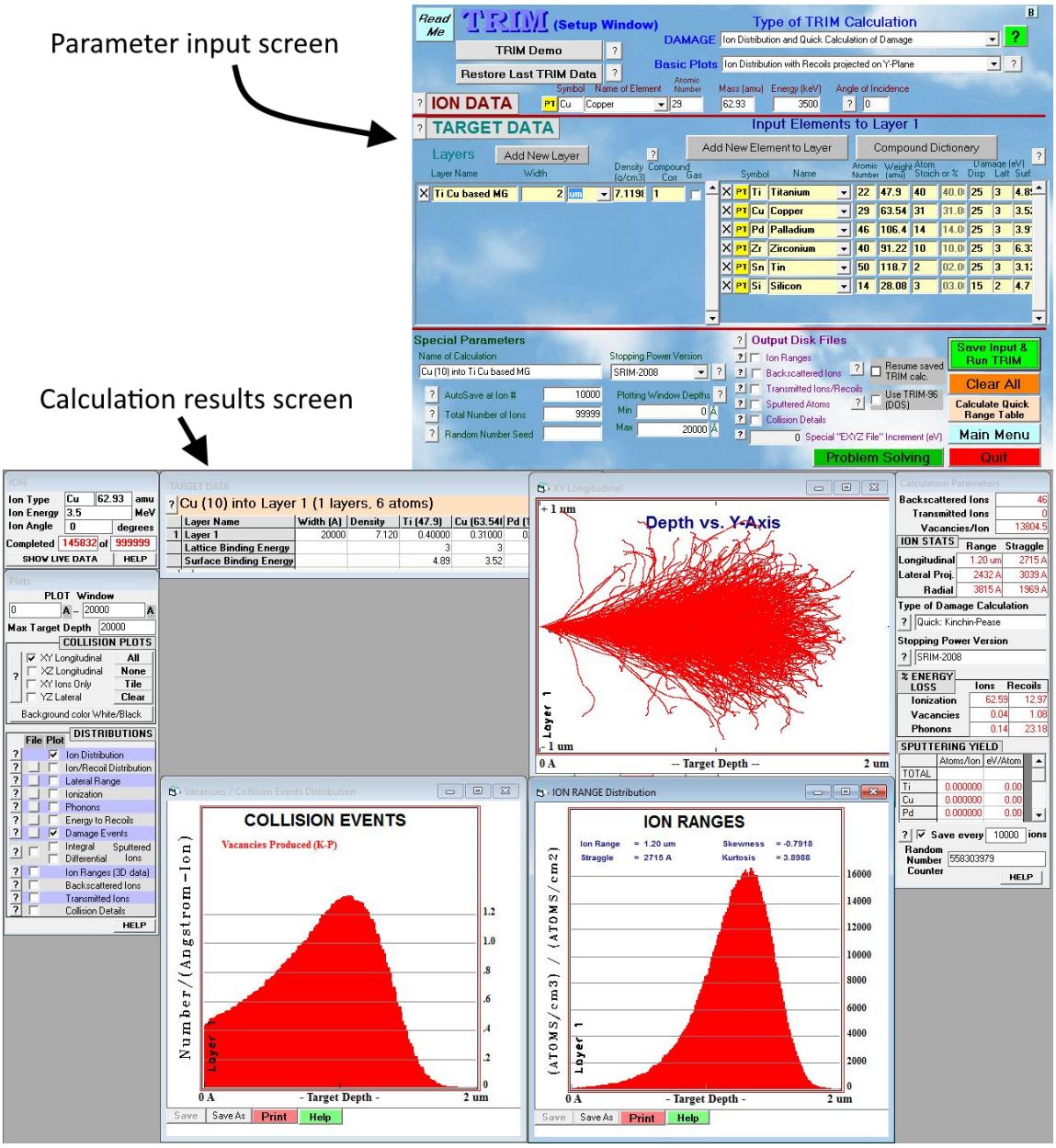

Figure 2.21: An image of the SRIM User interface and calculation screens for a typical calculation in this body of work.

behavior can be determined to within a known statistical tolerance.

With the output from SRIM, an experimentalist can determine, with a reasonable margin of error, the distribution of implanted ions as well as the damage distribution

and magnitude. However, no simulation code is perfect, and all results must be taken with caution. In the case of metallic glasses, this is doubly so.

The first issue is that SRIM must assume an atomic density. For metallic glasses this can often be difficult to determine, and the density of the glass may in fact change as the sample is bombarded due to phase changes or relaxation of the structure. This will effect the true ion ranges achieved in the sample, however, this change will not be reflected in the results given by SRIM.

The magnitude of displacements reported by SRIM will also be inaccurate. When SRIM tallies a displacement event, it is assuming a value for the lattice binding energy of the struck atom. In crystalline solids, this value can be well known, especially for solids of only one element. However, in compounds these values are less well known, and in amorphous materials the lattice binding energy can vary greatly. These values are not very well known and will have a large impact on the magnitude of the displacements caused. This inaccuracy should not, however, create large discrepancies in the distribution of displacements.

2.2.2.3 Beam Energy

Beam energy is something that must be carefully considered before the start of the irradiation. The beam energy will not only determine the ion range into the sample but also the damage distribution and magnitude. A high energy ion will penetrate further into the sample and will normally cause more damage. However, the peak damage area will also be shifted away from the surface. This must be considered carefully especially in cases where a surface layer is being studied for damage tolerance. A higher energy ion will ensure that near surface doping effects are negligible, however, having a lower energy ion will increase the damage per ion caused in the near surface region. These two effects must be balanced according to

the goals and sensitivity of the samples. SRIM is a very useful tool in determining this parameter.

2.2.2.4 Beam Intensity

The intensity of the beam is also an important factor to consider, especially for samples that are heat sensitive. Measured beam current for ion beams usually ranges from a few nano-amperes to tens of micro-amperes. While this is a small value for the current, it must be noted that the ions are at a very high energy and are depositing all of that energy within a very small volume. In the experiments here, the highest energy beams used only penetrate $\approx$2 μm. When this is taken into consideration, the heating caused by the beam is very significant. The metallic glass samples used in these experiments are heat sensitive, and so careful consideration must be made when determining the acceptable beam current for all irradiations. In some cases, such as in silicon (Si), altering the beam intensity while maintaining the ultimate fluence will change the amount of damage caused in the specimen[25]. The defect annealing time in metallic glass is not well understood, so in order to maintain continuity between samples, a constant beam intensity should be kept. Therefore for all experiments performed in this study the beam flux (number of ions/cm^2-s) has been kept constant unless otherwise noted.

2.2.2.5 Scan Pattern

Scan pattern is another factor which is important to consider. In order to maintain uniformity, most ion beam systems rely on scanning a focused beam spot over the sample. By performing this scan, uniformity should be maintained, regardless of the intensity profile for the focused beam spot. This is great for maintaining uniformity, however, this does create a pulsed beam effect. Since the spot will irradiate one part of the sample, then move away for a period of time before returning to

bombard that part of the sample, the damage rate in any particular spot will vary on a time scale similar to that of the scan time. The time between bombardment can, depending on the scan pattern used, also vary depending on the sample's proximity to the edge of the scan area. To solve this issue, a constant defocused beam can be used.

The difference in the resulting microstructure can be effected greatly depending on if a scanned beam or defocused beam is being used. This effect has been shown to be quite real in pure iron (Fe) systems, where the amount of void swelling can be altered significantly by the scan pattern chosen[26]. However, a defocused beam cannot guarantee uniformity, causing problems in estimating dose to any particular area. A way to split the difference then is to use a "wobble" beam. In this case, a defocused beam is slightly scanned, but never to the extent where a large fraction of the beam has been scanned off. By using this technique, the uniformity of the beam deposition can be enhanced while maintaining a mostly constant beam intensity across the sample. For all experiments here, a focused scanned beam was used. To help with results consistency, all samples taken using the FIB method were taken from the center of the sample.

2.2.2.6 Fluence

Lastly, ultimate fluence must be considered. Fluence is a difficult parameter to predict since ion damage effects may take place at vastly different levels of damage. Normally in theses cases, fluences points are selected not to be linearly increasing, but increasing on a logarithmic base 10 scale. For example, instead of having points taken at 2E15, 4E15, 6E15, and 8E15 ions/cm^2, fluences would instead be taken at 1E15, 1E16, 1E17 and 1E18 ions/cm^2. In this way more of the microstructure changes induced by the ion beam can be observed.

3. ULTRA-THIN FILMS OF MG

In this chapter, a study is reviewed that explores the effect of free surfaces on the crystallization resistance of metallic glasses. For electron-transparent films on the order of 100 nm, it was found that after ion bombardment and heating, the sample crystallized. Finite element analysis in an earlier study, however, showed that crystallization from direct damage cascade heating is unlikely since the quench time is many orders of magnitude faster than the critical cooling rate[4]. It is proposed then that "vacancies" created by the ion bombardment built up over time into low density zones, dubbed "excess free volume". This excess free volume enhances atomic mobility allowing for atomic level re-arrangement into the lower energy crystal state.

Alternatively, for ultra-thin films ≈10 nm in thickness, no crystallization was observed even under the same treatment. The films in question stayed amorphous even though they were subjected to the exact same conditions as the thicker films. These observations, combined with Molecular dynamics (MD) simulations, indicate that the free surface act as a defect sink for excess free volume. This removes the excess free volume, hindering the atomic mobility of the atoms, preventing crystallization.

3.1 Experimental Design

The metallic glass used in this study is zirconium based. The specific composition is: $Zr_{50}Cu_{35}Al_7Pd_5Nb_3$. This metallic glass was chosen due to its availability and ease of preparation via electropolishing. Twin jet electropolishing was used in this case since it is a fast and effective way to produce electron transparent samples. More details about twin jet electropolishing can be found in the equipment chapter. It also produces variable film thicknesses which was of interest in this study. Differential Scanning Calorimetry (DSC) was performed on this sample to determine its glass

transition and crystallization temperature. Knowing these temperature points was important in selecting the substrate temperatures that should be tested during ion bombardment. The DSC curves for various heating rates can be seen in figure 3.1. The lowest heating rate, 10 °C/min, will be used since it is closest to the steady-state conditions. The glass transition temperature is 442 °C while the crystallization temperature is 489 °C.

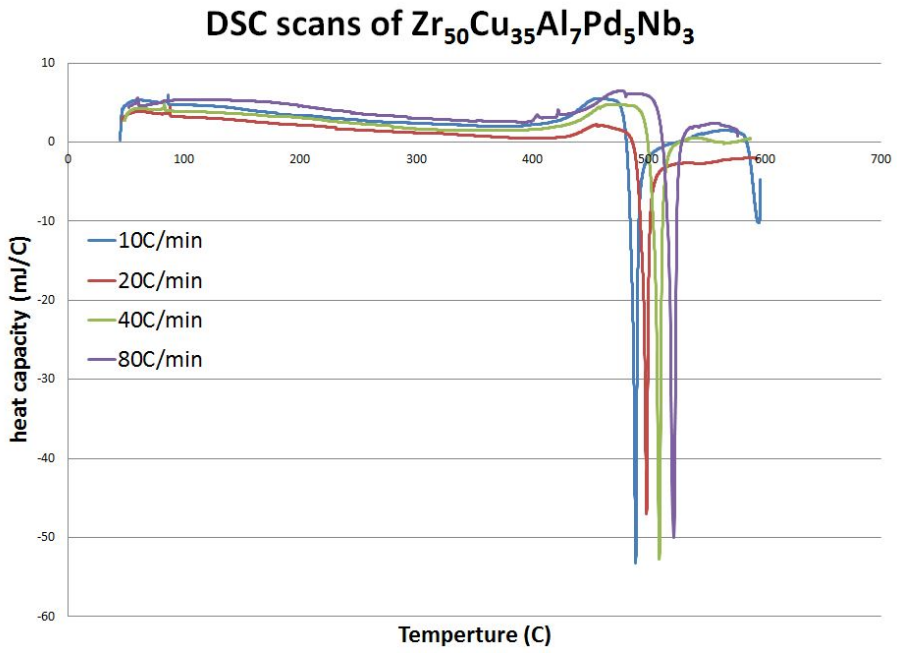

Figure 3.1: Plots of acquired DSC curves for Zr_{50} Cu_{35} Al_7 Pd_5 Nb_3 MG ribbon. Curves show distinct points for glass transition and crystallization temperatures.

The treatment of this metallic glass took place at the Argonne National Labs (ANL) Intermediate Voltage Electron Microscope (IVEM) facility. This facility offers a unique capability of *in-situ* TEM observation during heavy ion bombardment. This allows a detailed look at not just the final results of the irradiation, but a detailed look at the microstructure evolution when forming the final structure.

For ion bombardment, a 1 MeV Kr beam was used. This beam was chosen due to availability at the facility as well as to reduce the amount of chemical changes in the samples. The discussion of ion choices and energies can also be found in the equipment chapter. During irradiation the sample was observed using bright and dark field TEM. Still images as well as videos were taken of the sample to see the dynamic creation and annihilation of crystalline defects in the amorphous substrate. The substrate temperature was also adjusted during irradiations to see the effect this had on the radiation response.

3.2 Experimental Results

Initially, the sample was characterized before irradiation to ensured that the sample being used was fully amorphous. This ensures that any crystallization observed came from the ion beam treatment and not the preparation from electropolishing. An image of the sample pre-bombardment can be seen in Figure 3.2.

As can be seen by the micrographs and diffraction pattern, the sample is completely amorphous. Next the sample was heated and irradiated in steps in order to see the effect on the sample. Figure 3.3 shows the heating and irradiation pattern used for these observations as well as some select micrographs. As can be seen from the figure, bombardment happened between the heating steps. The sample was observed before and after heating to determine if the crystallization was due to the increase in temperature or from ion bombardment. Figure 3.3 shows the final state of the sample enlarged, which really captures the essence of the observations made.

From the micrographs, there are two distinct parts of the sample that show two distinct behaviors. Electron Energy Loss Spectroscopy (EELS) was used to determine the two sample thicknesses. The thicker regions were found to be 100 nm thick, while the ultra-thin film is around 10 nm thick. Here it is shown that in the thicker part

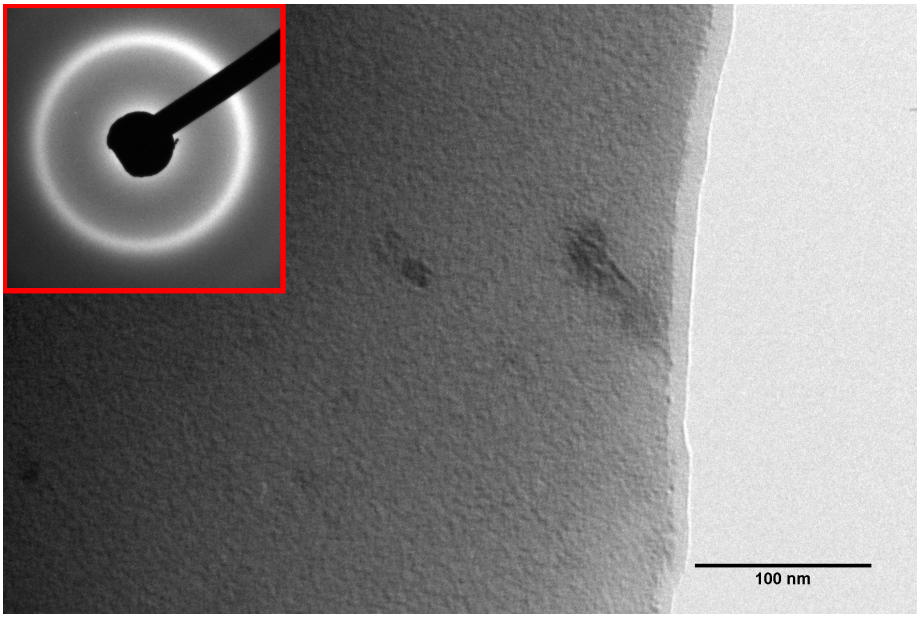

Figure 3.2: Image of the sample used in the ultra-thin MG studies. Composition: Zr_{50} Cu_{35} Al_7 Pd_5 Nb_3.

of the sample, there is a significant amount of crystallization. However, in the ultra-thin film region there is no sign of crystallization. The diffraction pattern does show some signs of crystallization, however, getting a small area selected for a diffraction pattern is not possible. This makes the dark field micrographs more indicative of the true sample structure. It is also important to note that the sample was heated to be above its glass transition temperature and the ultra thin film region had still not undergone crystallization.

3.2.1 Experimental Results: Discussion

From the observations made, it is quite interesting that the ultra-thin film stays amorphous while the slightly thicker films undergo extensive crystallization. Previous calculations were performed that showed the cooling rate at the center of the damage cascade is orders of magnitude faster then the critical cooling rate for initially forming

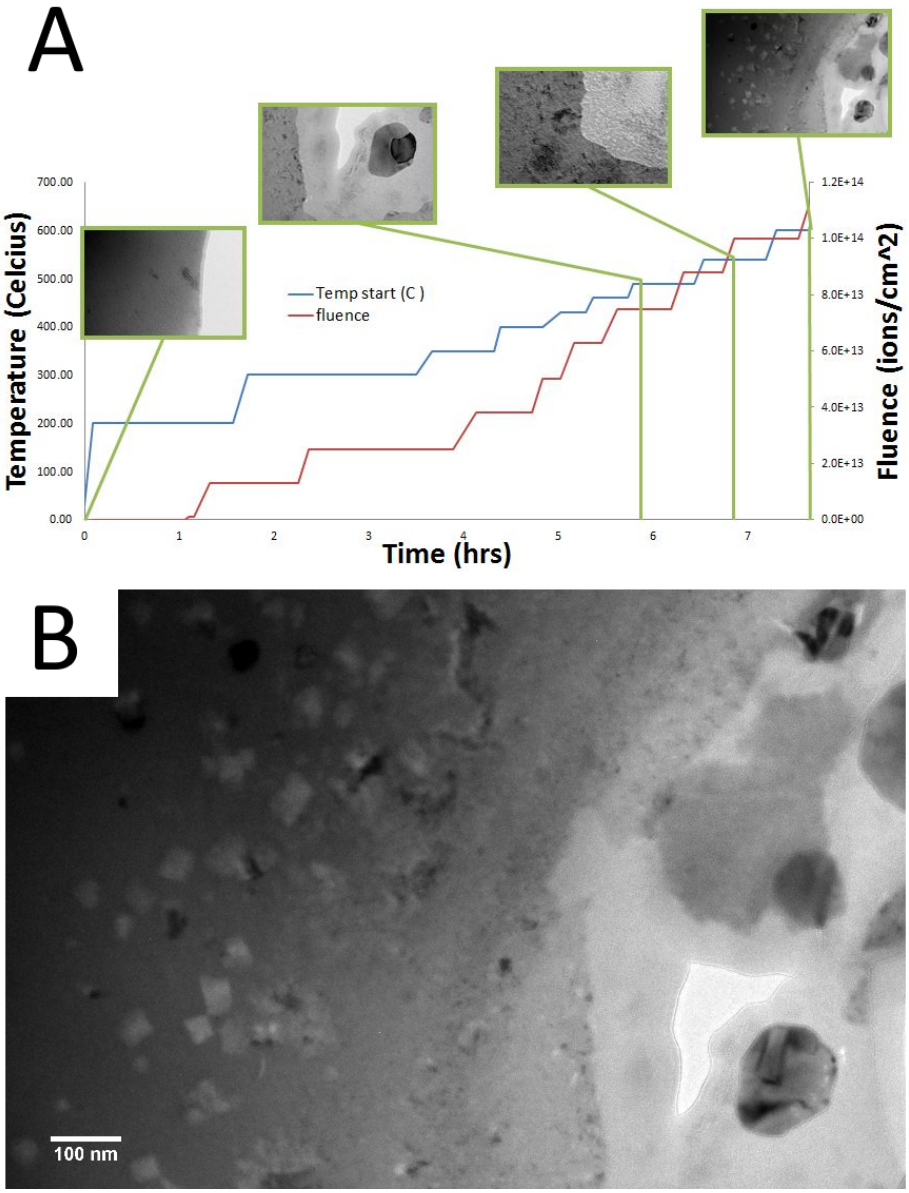

Figure 3.3: A) Plot of the temperature and fluence as a function of time experienced by the ultra thin film specimen. Micrographs from select points are included to show the phase evolution as a function of time. Composition: Zr_{50} Cu_{35} Al_7 Pd_5 Nb_3. B) Enlarged figure of the final state of the metallic glass after heating to 600 °C and ion bombardment.

a metallic glass[4].

It is proposed that the increase in excess free volume helps promote atomic mo-

bility, allowing stable crystal structures to form. This is created by the ion beam due to a defect imbalance. The defect imbalance phenomena occurs with ion beams since they create large amounts of vacancies in the near surface region. This phenomena has been documented in simulations and its effect has been seen in other ion beam related studies [3].For the samples used in this study, which are only around 100 nm thick, there is then a large amount of vacancies caused. An example defect imbalance curve can be seen in Figure 3.4.

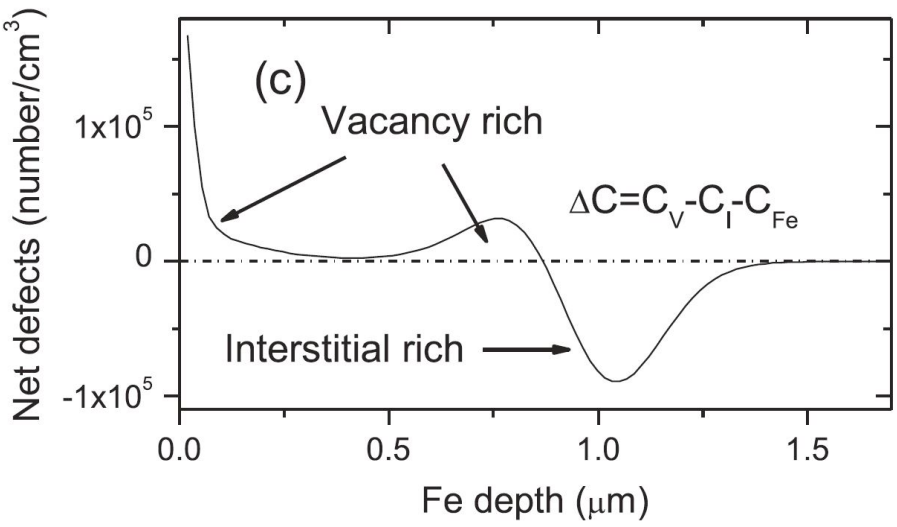

Figure 3.4: Plot of the defect imbalance created in pure iron as a result of bombardment by 3.5 MeV iron ions [3].

It is postulated that the free surfaces remove the excess free volume created by ion bombardment. By removing this excess free volume, atomic mobility is limited, preventing crystallization. In the ultra-thin region the surface effect is very strong, preventing crystallization. However, in the thicker part of the sample, the surface effect is weaker in the bulk of the film, allowing for crystallization to take place. This

will be extremely difficult to directly observe experimentally, so a computational method is employed.

3.2.1.1 Molecular Dynamics Simulations

Molecular dynamics simulations were undertaken in order to understand at an atomic level the mechanisms behind the observations made at ANL. To perform this simulation, an amorphous nickle thin film was produced. A liquid nickle system was simulated, then the atoms were frozen in place at 0 K. This closely simulates the actual process for forming a metallic glass, creating a good simulated sample to experiment on. Next, a fraction of the atoms are randomly removed from the substrate. This is to simulate the excess free volume created by ion bombardment. After these atoms were removed, the system was allowed to relax, allowing observation of how the excess free volume interacts with the free surfaces.

The results of this process can be seen in Figure 3.5. In the figure, all atoms that are shown have an average bond length 2σ longer than the average bond length for the system without excess free volume are highlighted.

As time passes, it can be seen that the excess free volume is eliminated nearly completely, starting from the free surface and working into the bulk. This clearly shows that the free surface acts as a sink for these defects. The thin film created in this simulation is of the same size as the films in the experiment. Even though it is a different material, this clearly shows that the removal of excess free volume through a free surface is plausible.

3.3 Conclusions

In-situ observation of thin film metallic glass under ion bombardment revealed that ultra-thin films on the order of 10 nm are highly resistant to crystallization both from extreme heating and ion bombardment. Under the same conditions it was found

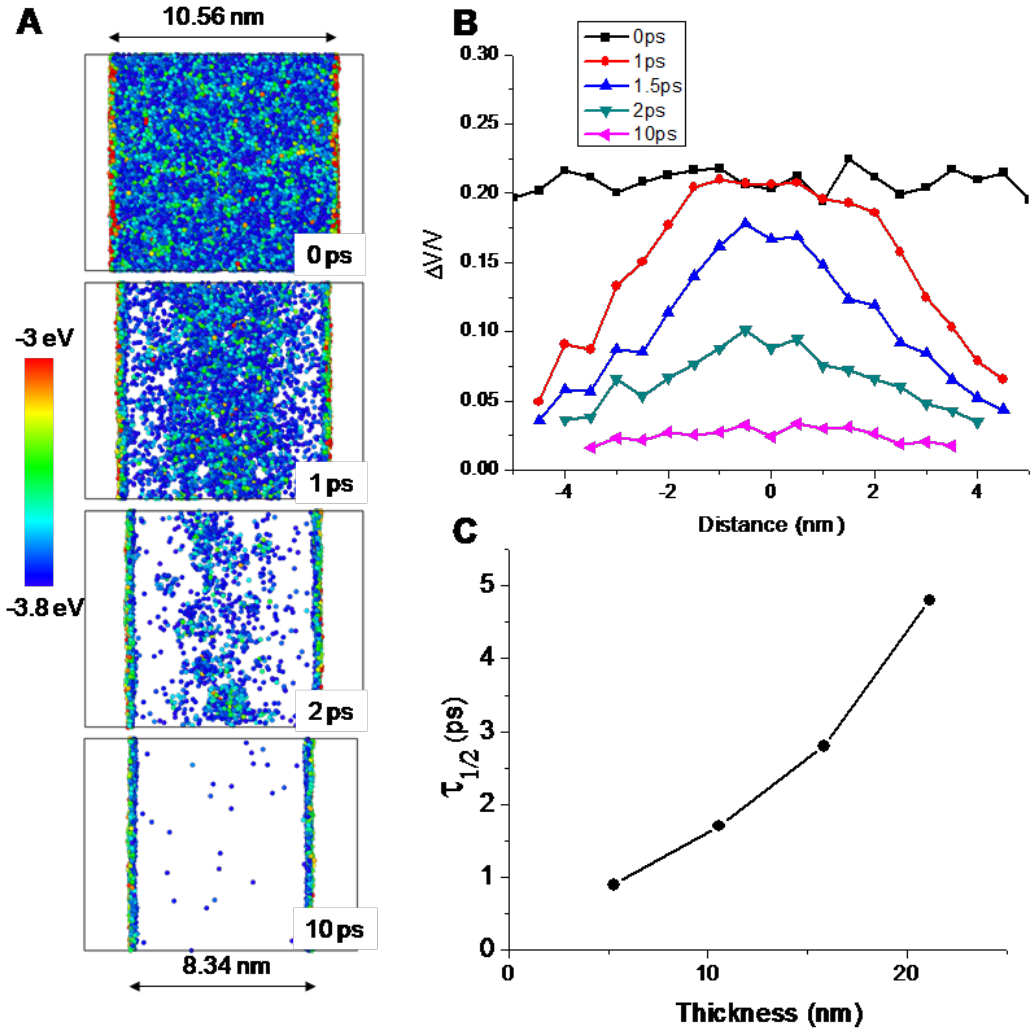

Figure 3.5: Simulations perform to study the movement of excess free volume within an amorphous film.

that slightly thicker films were found to crystallized. The mechanisms behind this phenomena were then explored. From finite element analysis, it has been shown that the crystallization is not likely caused by direct damage cascade heating, since the quench time is far too quick. Instead it is proposed that the crystallization is caused by a build up of excess free volume by ion bombardment. The introduced excess free volume allows for increased atomic mobility, leading to atomic re-arrangement into

more stable crystal structures. The crystallization resistance of the thin films then comes from the removal of the excess free volume through the free surface.

To investigate this hypothesis, molecular dynamics simulations were performed on an ultra-thin film metallic glass sample. These simulations showed that excess free volume is readily removed via the free surface. From this study is it concluded that, at least in thin films, ion-induced excess free volume in the metallic glass can lead to crystallization. It was also shown that the metallic glass free surface is capable of removing excess free volume which can enhance crystallization resistance.

4. CRYSTALLIZATION AND RE-AMORPHIZATION IN THIN FILM MG

In this chapter, a study is performed that looks at the crystallization and re-amorphization of metallic glasses. The metallic glass in question was held at a constant temperature while being bombarded by heavy ions. *In-situ* TEM bright field and dark field still shots were made of the sample before and after bombardment. Videos of the evolving microstructure were taken using dark field imaging techniques. In the videos, it is shown that there are crystals forming and disappearing in the sample. This is evidence for both crystal formation and crystal destruction by ion bombardment. The mechanisms behind this are explored.

4.1 Experimental Design

The metallic glass used in this study is zirconium based. The specific composition is: $Zr_{50}Cu_{35}Al_7Pd_5Nb_3$. This metallic glass was chosen due to its availability and ease of preparation via electropolishing. Twin jet electropolishing was used in this case since it is a fast and effective way to produce electron transparent samples. More details about twin jet electropolishing can be found in the equipment chapter. DSC was performed on this sample to determine its glass transition and crystallization temperature. Knowing these temperature points was important in selecting the substrate temperatures that should be tested during ion bombardment. The DSC data can be found in Figure 3.1 on page 60. From the 10 C/min curve, it can be seen that the glass transition temperature is 442 °C while the crystallization temperature is 489 °C.

The treatment of this metallic glass took place at the ANL IVEM facility. This facility offers a unique capability of *in-situ* TEM observation during heavy ion bombardment. This allows not only a detailed look at the final results of the irradiation,

but also at the microstructure evolution when forming the final structure.

For ion bombardment, a 1 MeV Kr beam was used. This beam was chosen due to availability at the facility as well as to reduce the amount of chemical changes in the samples. The discussion of ion choices and energies can be found in the equipment chapter. Before and after irradiation still images of the sample were taken using bright field and dark field TEM. During bombardment videos were taken in dark field imaging mode in order to see microstructural evolution.

The sample used in this experiment was placed into the TEM hot stage and elevated to 400 °C. At that point the irradiation began. The dark field videos were invaluable in looking at the microstructural evolution in real time. In this mode the crystalline defects in the sample show up as bright white spots, allowing for easy identification against the mostly amorphous background which appeared as a uniform dark gray.

4.2 Experimental Results

Initially, the sample was characterized before irradiation to ensure that the sample being used was fully amorphous. This ensures that any crystallization observed came from the ion beam treatment and not the preparation from electropolishing. An image of the sample pre-bombardment can be seen in Figure 4.1 on page 70.

Next, the sample was heated up to temperature and the ion bombardment began. A plot of the heating curve and fluence curve can be seen in Figure 4.2. During bombardment, videos of the sample were taken using the dark field imaging technique as to highlight crystal formation. The videos cannot be presented in this format, however, some still images of the sample at different fluence points were taken. These images showing the creation and destruction of some nano-crystals can be seen in Figure 4.3.

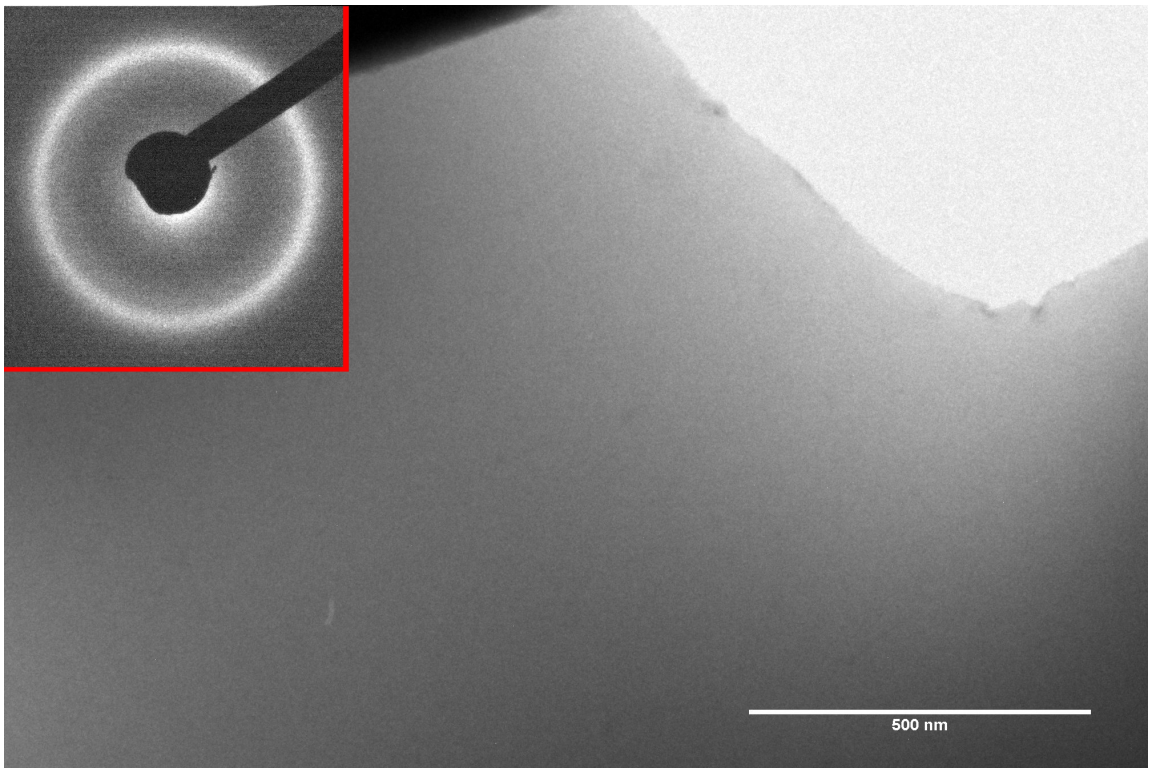

Figure 4.1: A micrograph showing the sample region of interest after heating but before irradiation.

Since the images taken were using dark field technique, the crystal intensity is also related to crystalline direction. Therefore, the crystal creation and re-amorphization observed could be due instead to crystal rotation. It must be determined if the crystals that are observed appearing and disappearing are actually doing do or simply rotating. In order to determine which case was accurate, the density of nano-crystals was recorded over a period of time.

Since the crystals are separated by amorphous zones, and by observing the diffraction pattern, it can be seen that the the nano-crystals are isotropically positioned. That is, there is no preferred orientation for the nano-crystals. It is clear from the presence of crystals that there is a creation mechanism at work. Therefore, if the

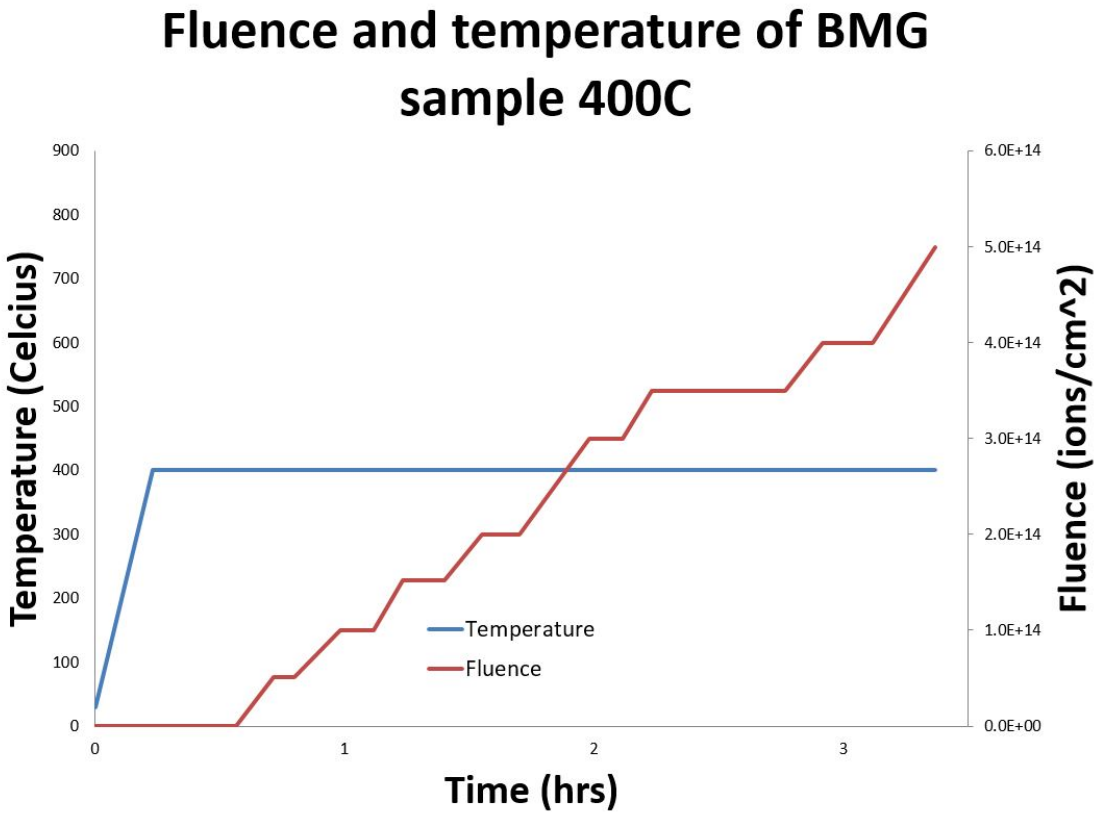

Figure 4.2: Plot showing the heating and fluence history of the sample being analyzed in this section.

crystals that are seen disappearing are simply rotating out of focus, it is expected that the crystal density will constantly increase. However, if the crystals are indeed becoming re-amorphized then the crystal density over time could decrease, stay constant or increase depending on the magnitude of the creation and destruction mechanisms. If the crystal density is observed to be increasing then the results ill be inconclusive, however, if the crystal density is constant or decreasing then it can be said that the nano-crystals are being re-amorphized rather than just rotating.

The crystal density was recorded for a section of the sample. The results can be seen in Figure 4.4. As can be seen from the figure, over a large range of fluences, the

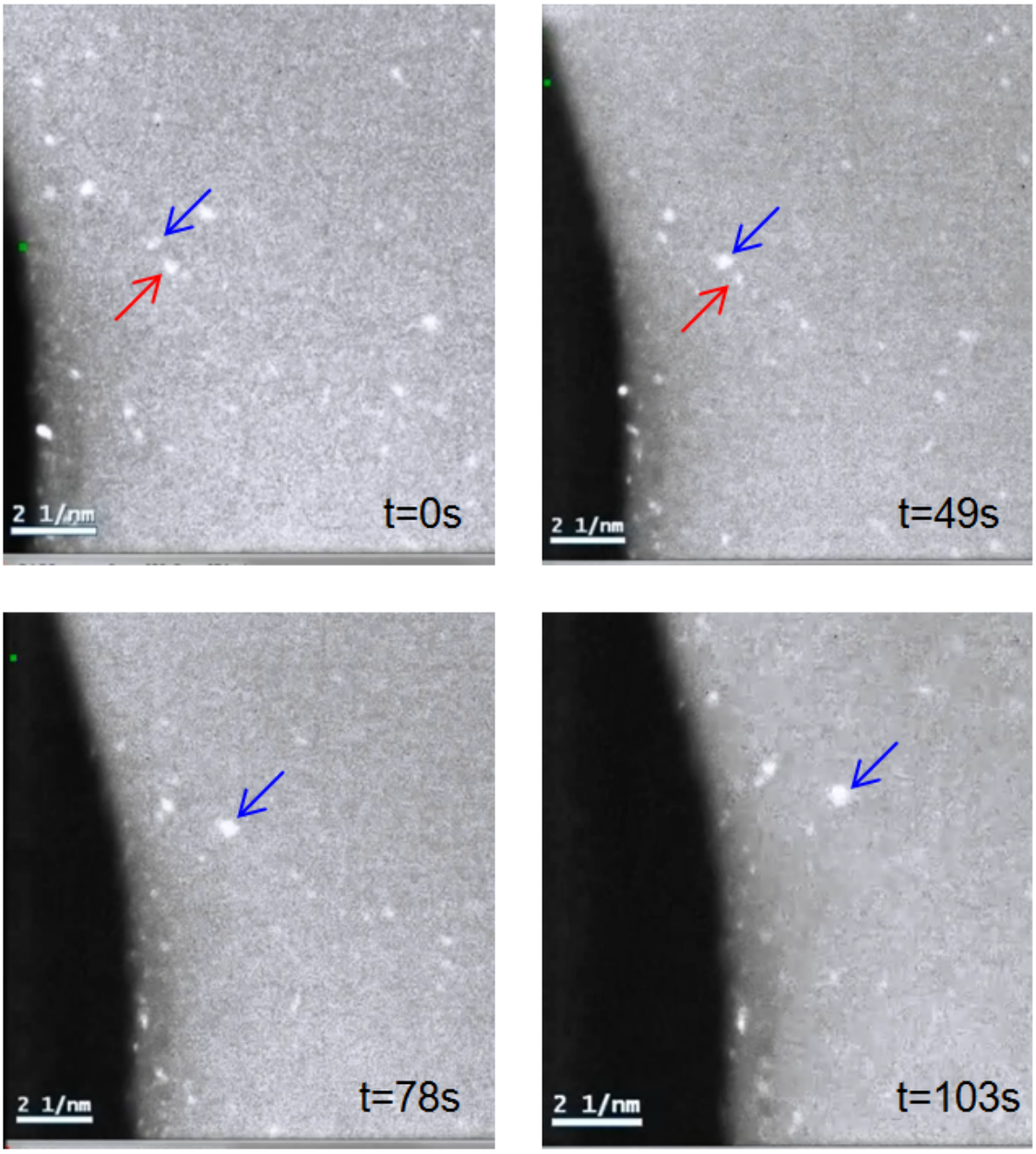

Figure 4.3: Still images from videos taken of the sample showing evolution of the microstructure over time.

crystal density is staying constant. Since the crystals are isotropically distributed, there must be a crystalline destruction mechanism.

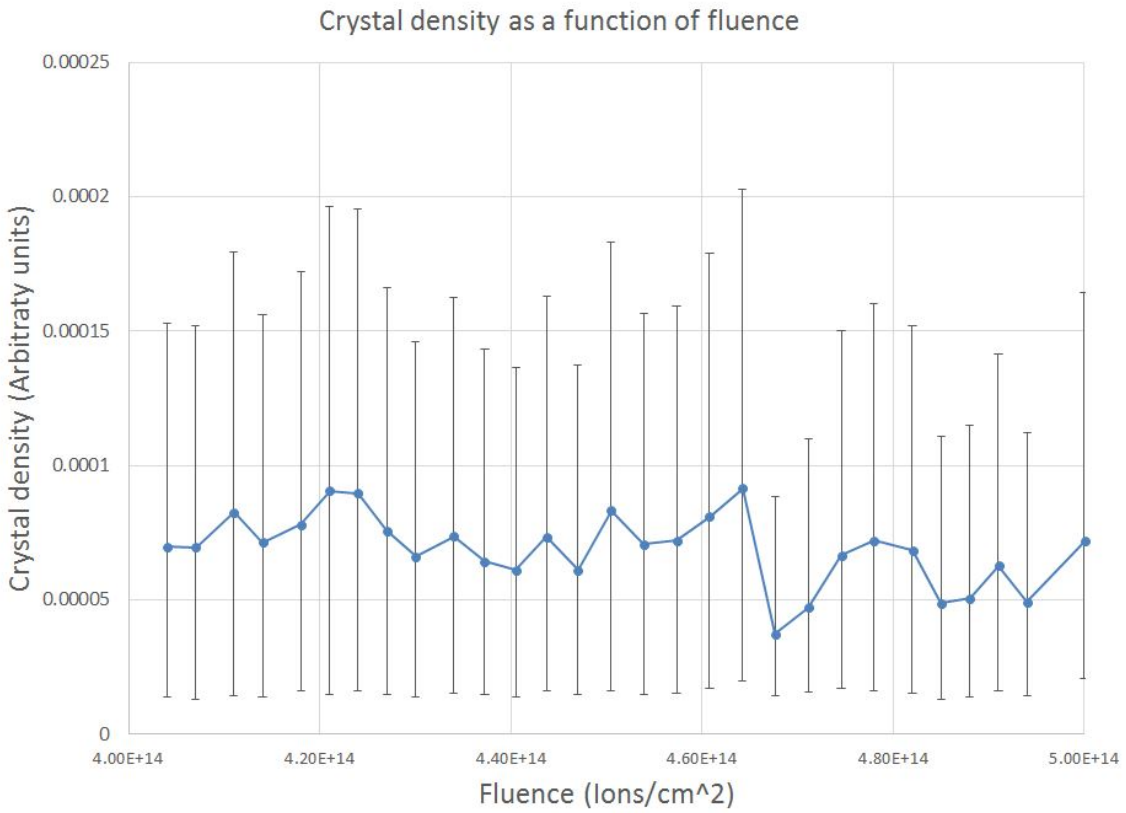

Figure 4.4: Plot showing the change in crystal density from a fluence of 4E14 to 5E14.

4.3 Results Discussion

The crystallization of thin film metallic glass has already been shown in the ultra-thin films chapter to be most likely caused by the accumulation of excess free volume. Nano-crystallization was also observed in that sample, however, re-amorphization was not observed. An explanation must be given for the re-amorphization of the nano-crystal structures. In this case it can be argued that the crystals are re-amorphizing due to localized melting from the damage cascade. In a previous study using finite element analysis, it was shown that in the core of the damage cascade, the temperatures reached were easily high enough in order to cause localized melting

[4]. It was also shown that the melted area solidified at a rate much higher than the critical cooling rate initially required to cast the metallic glass. A figure showing the results from the previous study are shown in Figure 4.5.

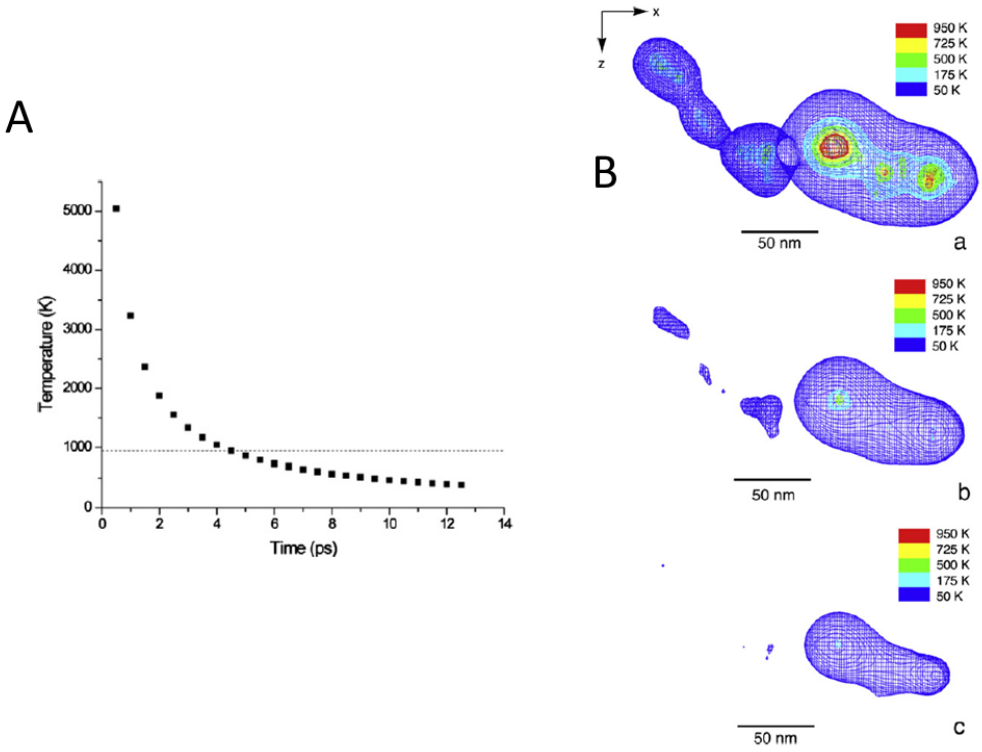

Figure 4.5: A) Plot showing the temperature evolution as a function of time in the hottest part of the damage cascade. B) Image of the simulated damage cascade used to derive the temperature plot. Taken from Meyers *et. al* [4].

This damage cascade induced melting and re-quenching is the proposed mechanism by which the metallic glass re-gains its amorphous state. This effect is entirely dependent on the beam which strengthens this argument based on the unchanging density of the crystals as see in Figure 4.4. This indicates that the rate of creation

of nano crystals by ion-beam induced excess free volume is in equilibrium with the rate of crystal removal by damage cascade quenching. An equilibrium state such as this would be difficult to achieve if there were two independent mechanisms at work. It was also evident from observations, that when the sample was not being irradiated, the microstructure did not evolve, indicating that both the crystal creation and destruction cannot be caused by a heat effect alone.

4.4 Conclusions

From the observations made with this sample, ion bombardment provides both a creation and a destruction mechanism for nano-crystals in a thin film amorphous metallic glass. Video evidence suggests that the number of crystals which have been formed by creation of excess free volume by ion bombardment saturates after a certain time. This saturation suggests a destruction mechanism as well, which was not observed in previous ultra-thin studies. Based on previous modeling research, the destruction mechanism is postulated to be directly related to the core of a damage cascade created by ion bombardment. Localized melting and rapid quenching occurs in this region, which replicates on a very small scale the process used for initially forming the metallic glass. The localized melting and rapid re-quenching is able to re-amorphize crystalline structures that have formed within the film. Since both of these effects are driven by ion bombardment, it implies that at a certain point the effects will cancel out, leaving an equilibrium level of nano-crystals in the matrix. This equilibrium state was observed in these samples, strengthening the argument for a direct ion beam creation and destruction mechanism.

5. LAYERED STRUCTURES

In this chapter, a layered structure consisting of an amorphous material, SiOC, and a polycrystalline material, Fe, was irradiated to a high fluence by 120 keV He ions in order to determine the radiation stability of the structure. It was found that for a thin film structure with characteristic size ≈10 nm, the system was extremely radiation tolerant, withstanding up to 20 DPA without major structural changes. However, for a similar structure with a characteristic size of ≈50 nm, there were major structural changes observed. This phenomena is similar to previous observations using free surfaces in the ultra-thin film studies presented in chapter 3.

5.1 Experimental Design

The samples used in this experiment were produced using magnetron sputtering. A Si wafer with a thermally grown SiO_2 layer was used as the substrate. SiOC was deposited on top of this substrate, proceeded by a layer of Fe of the same thickness. This process was repeated until a layered structure of appreciable thickness was produced on top of the Si wafer. This required more thin layers to achieve when compared to the number of thick layers. Before irradiation a sample was made electron transparent by traditional TEM sample preparation then observed under TEM to ensure layer uniformity as well as confirm the amorphous nature of the SiOC. An image showing both the thin and thick layer sample before irradiation can be seen in Figure 5.1.

Next, the samples were irradiated using 120 keV He at room temperature. Helium was chosen to reduce chemical changes. 120 keV was chosen due to instrumental capability as well as for adequate range into the sample to reduce He deposition in the layer of interest. The samples were irradiated to 5, 12.5 and 20 DPA. The fluence

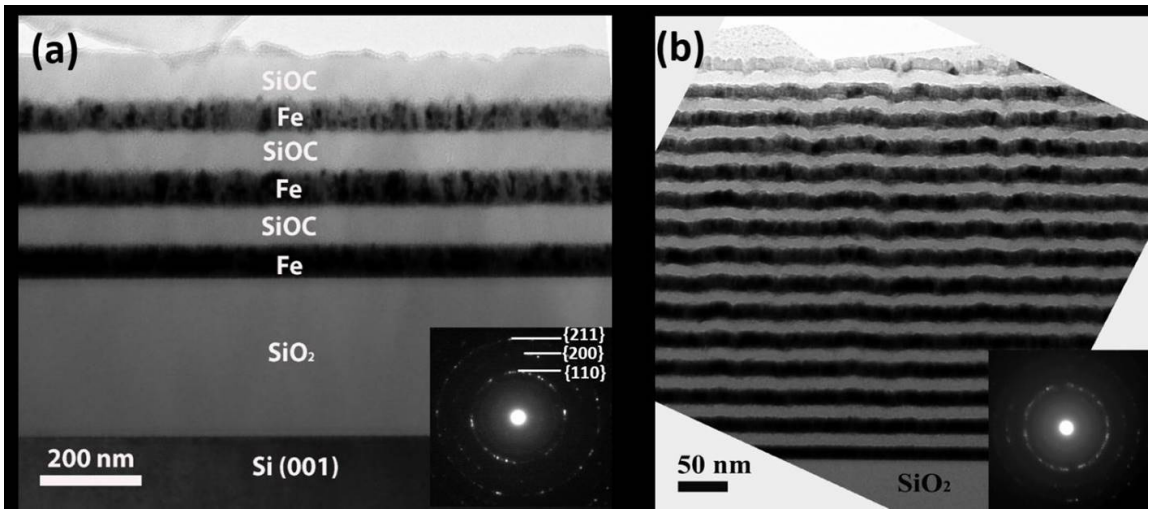

Figure 5.1: A micrograph showing the 10 nm and 50 nm samples before undergoing ion bombardment

required to attain 1 DPA in the layer of interest was determined through SRIM to be 4E16 ions/cm^2. All irradiations took place at room temperature.

After bombardment, the samples were made electron transparent through traditional TEM sample grinding, dimpling and ion milling. This preparation method was required as FIB cannot handle insulating materials, such as SiOC, and the layered structure is incompatible with electropolishing. After thinning, the samples were again observed under TEM to note any changes that occurred to the microstructure.

5.2 Experimental Results

As seen in Figure 5.1 the samples were originally very ordered and clean. The SiOC layers have a very uniform color, indicating a good amorphous structure, and the two layers are very distinct. Diffraction patterns to confirm the amorphous nature of the SiOC directly were impossible to obtain due to the size of the films. The diffraction pattern seen does have an amorphous ring and a scattering of spots. It is thought, from the bright field and dark field observations that the spots in the

diffraction patterns are a result of the polycrystalline Fe layer, while the diffuse ring is produced by the amorphous layer of SiOC.

After the irradiation was completed, the samples were examined under TEM to determine the microstructure changes. The data for the 20 DPA sample can be seen in Figure 5.2 and 5.3. As can be seen in the micrograph, the samples did undergo some microstructural changes.

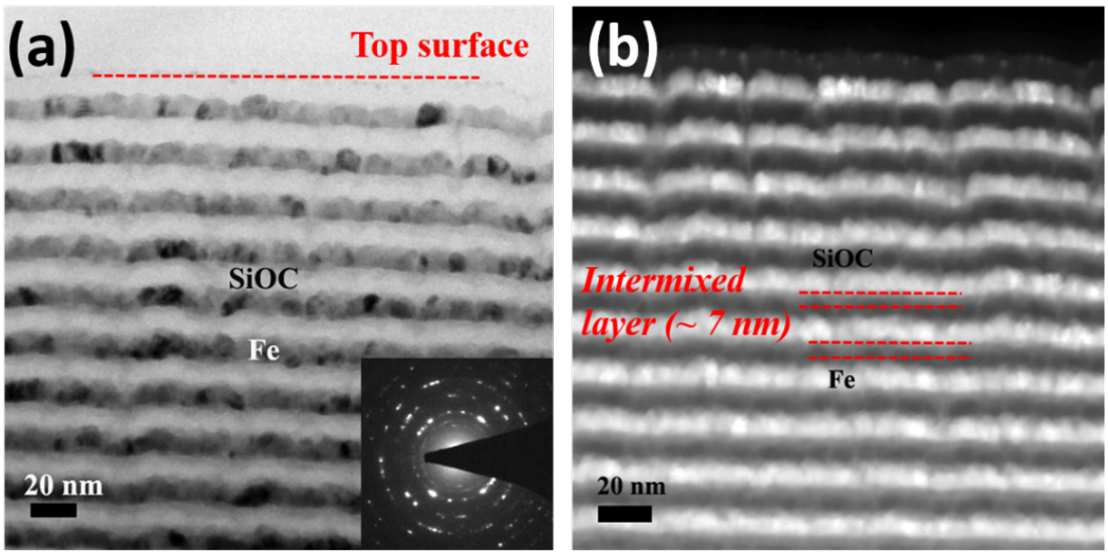

Figure 5.2: A micrograph showing the 10 nm sample after undergoing ion bombardment until 20 DPA. Bright field (a) and dark field (b) images are provided.

For the 10 nm samples, there was no observable decomposition of the SiOC layer. There was, however, some observed mixing between the SiOC and Fe layers. This mixing does not appear to have disrupted the SiOC layer to any great degree, and the material itself seems to maintain its amorphous structure. This result seems to confirm the previous findings from the ultra-thin film studies seen in chapter 3. For films of this size, excess free volume buildup is able to be limited by the interface

between the Fe and SiOC layer. This prevented crystallization of the SiOC layer even under heavy damage conditions.

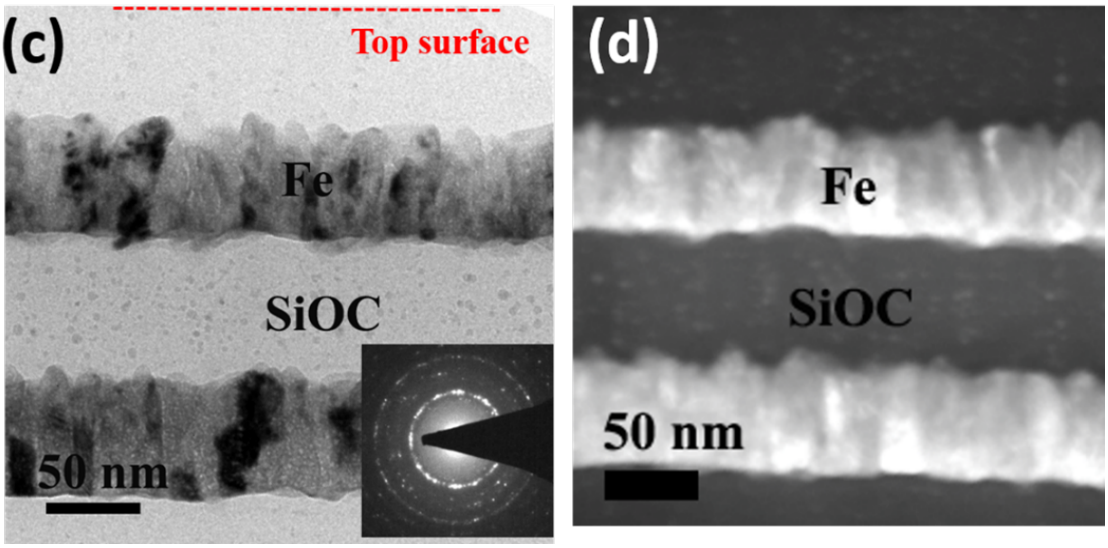

Figure 5.3: A micrograph showing the 50 nm sample after undergoing ion bombardment until 20 DPA. Bright field (c) and dark field (d) images are provided.

For the thicker film samples, the inter-layer mixing was not as pronounced, but there were some nano-crystals observed in the bulk of the SiOC layer. What is interesting to note is that, again, there was no crystal formation near the interface. This is most likely due to the elimination of free volume within the near-interface region. Next to the interface, the excess free volume that builds up can be eliminated. However, far from this surface, this defect sink property was not strong enough, and therefore free volume was able to buildup resulting in crystallization.

5.3 Conclusions

The layered structured studies were able to clearly show that the interface effect can function very similarly to the free surface effect observed in other metallic glass

compounds. In the very thin film structure there was no crystallization observed. This is thought to be because of the ability of the free surface to remove the excess free volume like the free surface seen in previous studies. In the thicker film samples, there was crystallization observed, but only away from the interface. This shows the ability of the free surface to keep crystallization from forming near the surface, but into the bulk, this effect is limited and cannot prevent free volume buildup and subsequent crystallization.

6. BULK STUDIES: TEMPERATURE DEPENDENCE

In this chapter, variable temperature experiments are performed on bulk metallic glass ribbons. Fluence, dose rate, ion species and ion energy were kept fixed in order to determine the response of the metallic glass purely as a function of temperature. It was found that the metallic glass, up to a certain temperature would remain completely amorphous. However, above that temperature point the metallic glass underwent complete crystallization. Around the critical temperature point, some strange phenomena were observed which warranted further studies. The mechanisms behind this crystallization and the abnormal phenomena observed are explored in this chapter.

6.1 Experimental Design

The samples used in this experiment were fabricated using the melt-spun ribbon technique. The composition used for all studies is $Ti_{40}Cu_{31}Pd_{15}Zr_{10}Nb_7Sn_2Si_3$. This composition was chosen due to its good glass forming ability as well as its wide super-cooled liquid region. DSC curves to determine temperature points were performed initially. A plot of the DSC curve can be seen in Figure 6.1. It is important to note that all DSC data acquisitions are preformed with the sample being heated at a constant rate. In the experiments performed here the samples are being heated then held at a constant temperature. The resulting microstructure that will be observed in the experimental setting will be the equilibrium structure for that temperature. The best descriptive data points for an equilibrium condition from the DSC curves available will be from the 10 °C curve. According to the 10 C/min curve, the glass transition temperature and the crystallization temperature are 448 °C and 498 °C respectively.

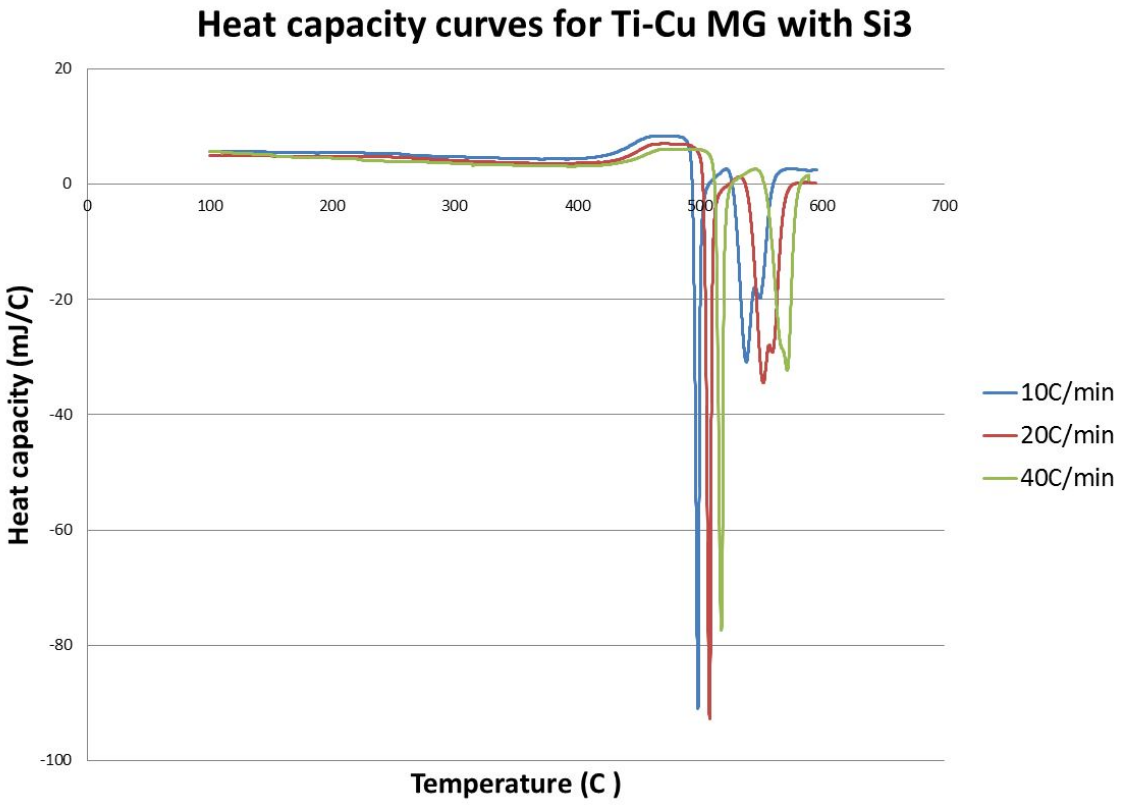

Figure 6.1: DSC curve showing three different heating rate curves for the Ti_{40} Cu_{31} Pd_{15} Zr_{10} Nb_7 Sn_2 Si_3 metallic glass used for the temperature dependent experiments.

Next, untreated samples were prepared using FIB in order to determine if the samples were completely amorphous before irradiation. An image of a sample before treatment is shown in Figure 6.2. As seen by the bright field, dark field and diffraction pattern, the sample is completely amorphous throughout.

With the important temperature points known, and the samples confirmed to be amorphous, the irradiation matrix was produced. The temperatures were chosen to give a good range of conditions up to and around the glass and crystallization temperature. The specific temperatures used were: room temperature, 100, 200, 225, 250, 275, 300, 390, and 480 °C.

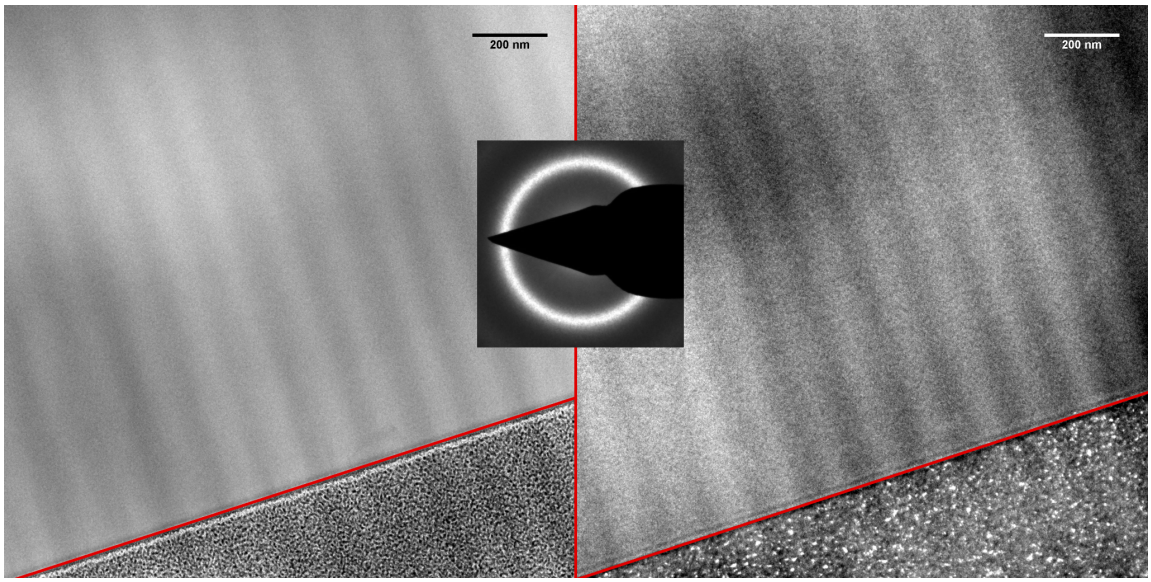

Figure 6.2: Bright field, Dark field and diffraction pattern images of Ti_{40} Cu_{29} Pd_{15} Zr_{10} Nb_7 Sn_2 Si_5 MG before treatment.

The samples were all irradiated with 3.5 MeV Cu to an ultimate fluence of 1E16 ions/cm^2. In order to ensure the effects from beam heating and annealing effects were constant for all samples, the beam flux was kept the same for all samples. A SRIM plot showing the expected Cu ion distribution and DPA for a 1E16 ions/cm^2 irradiation are shown in Figure 6.3. After irradiation, electron transparent samples were made using the FIB lift out process and examined under TEM.

6.2 Experimental Results

TEM examination of the samples after FIB processing showed some very interesting results. From the bright field, dark field and diffraction patterns, samples irradiated up to 225 °C showed no crystallization. There was some near surface re-structuring, but that is believe to be a result of some oxidation or carbonation during either initial fabrication, or as a result of oil contamination in the irradiation chamber. A compilation of images for each of the temperatures up to 225 °C is

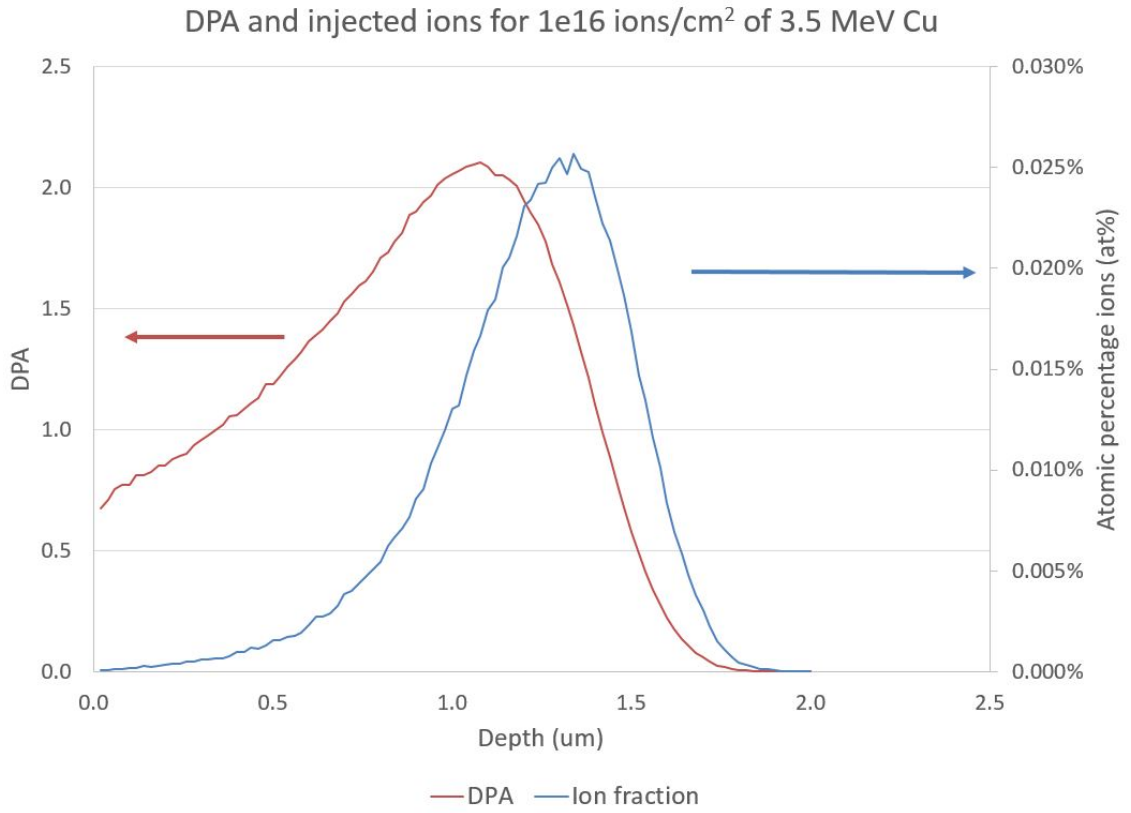

Figure 6.3: SRIM output showing the calculated range and DPA curve for 1E16 ion/cm^2 of 3.5 MeV Cu into Ti_{40} Cu_{31} Pd_{15} Zr_{10} Nb_7 Sn_2 Si_3.

shown in Figure 6.4.

Since the samples were stable to 1E16 ions/cm^2, a sample was irradiated at room temperature to 1E17 ions/cm^2 to test for high-DPA stability. This sample was completely amorphous as well, showing that crystallization from direct ion bombardment is very difficult to achieve in bulk samples. An image of this sample after bombardment can be seen in Figure 6.5.

All samples above 250 °C show complete crystallization even far beyond the ion range. The deepest observed crystallization was at 10 μm in depth. This depth is largely limited by the FIB to be able to produce samples which are larger then 10 x

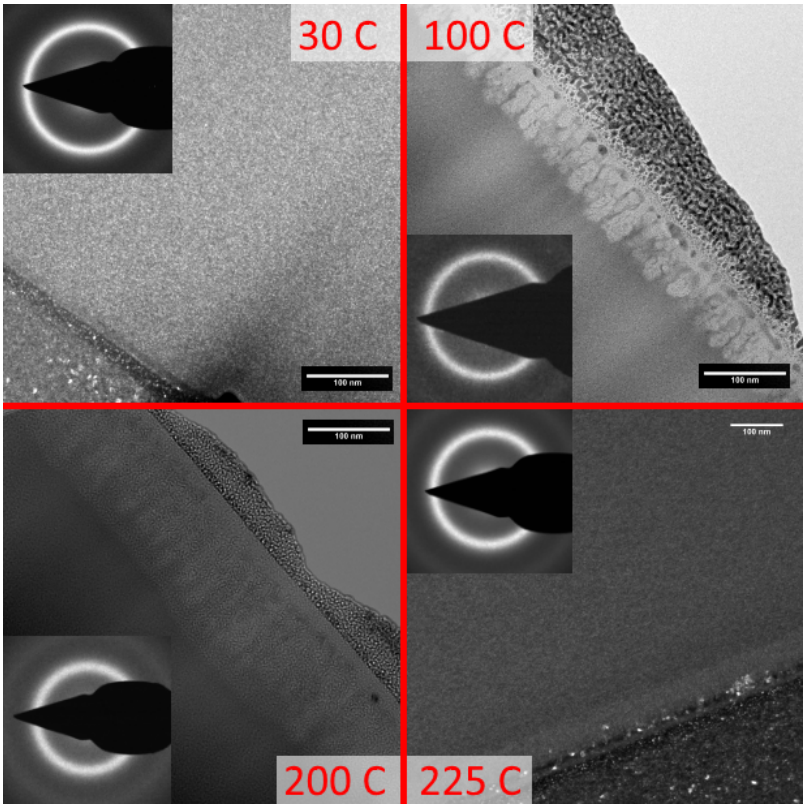

Figure 6.4: Bright field and dark field micrographs of samples from 30-225 °C.

10 μm in size. Images of the samples irradiated above 250 °C can be seen in Figure 6.6.

Lastly, at 250°C a very interesting structure was observed. It is a multilayer structure which consists of several distinct layers. Large isotropic grains are present from the surface to 674nm which interestingly enough, appear to have thin bands of amorphous material between them. Next an amorphous band from 674nm to 1127nm is present followed by a region of columnar grains which extend until 1456 nm where the structure is dominated by a nano-grained structure outside of the ion range. An image of this structure is found in Figure 6.7.

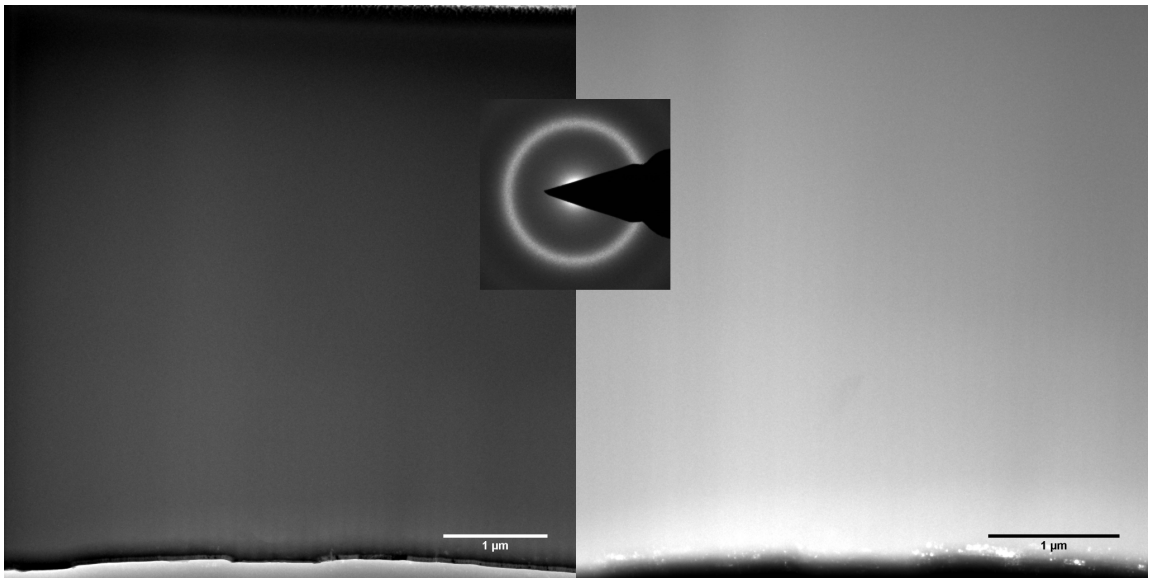

Figure 6.5: Bright field and dark field and diffraction pattern micrographs of a sample irradiated at room temperature to 1E17 ions/cm^2.

6.3 Discussion of Results

6.3.1 30 to 225 °C

It was shown in the TEM results that for sample with a substrate temperature at or below 225 °C, there was no crystallization observed. This finding is important since it shows that in bulk samples even high fluences are not enough to cause crystallization on their own. This result is very different from the previous findings in the thin films and ultra-thin films study. This crystallization resistance is thought to arise from two different mechanisms: injected interstitial interactions and 3D re-structuring. Both of these mechanisms work to remove excess free volume from the sample, preventing crystallization.

First, in the case of the thin films, nearly all incident ions pass completely through the sample. This creates excess free volume while the injected interstitial effect is nullified. However, in the bulk case, the ions come to rest in the sample creating

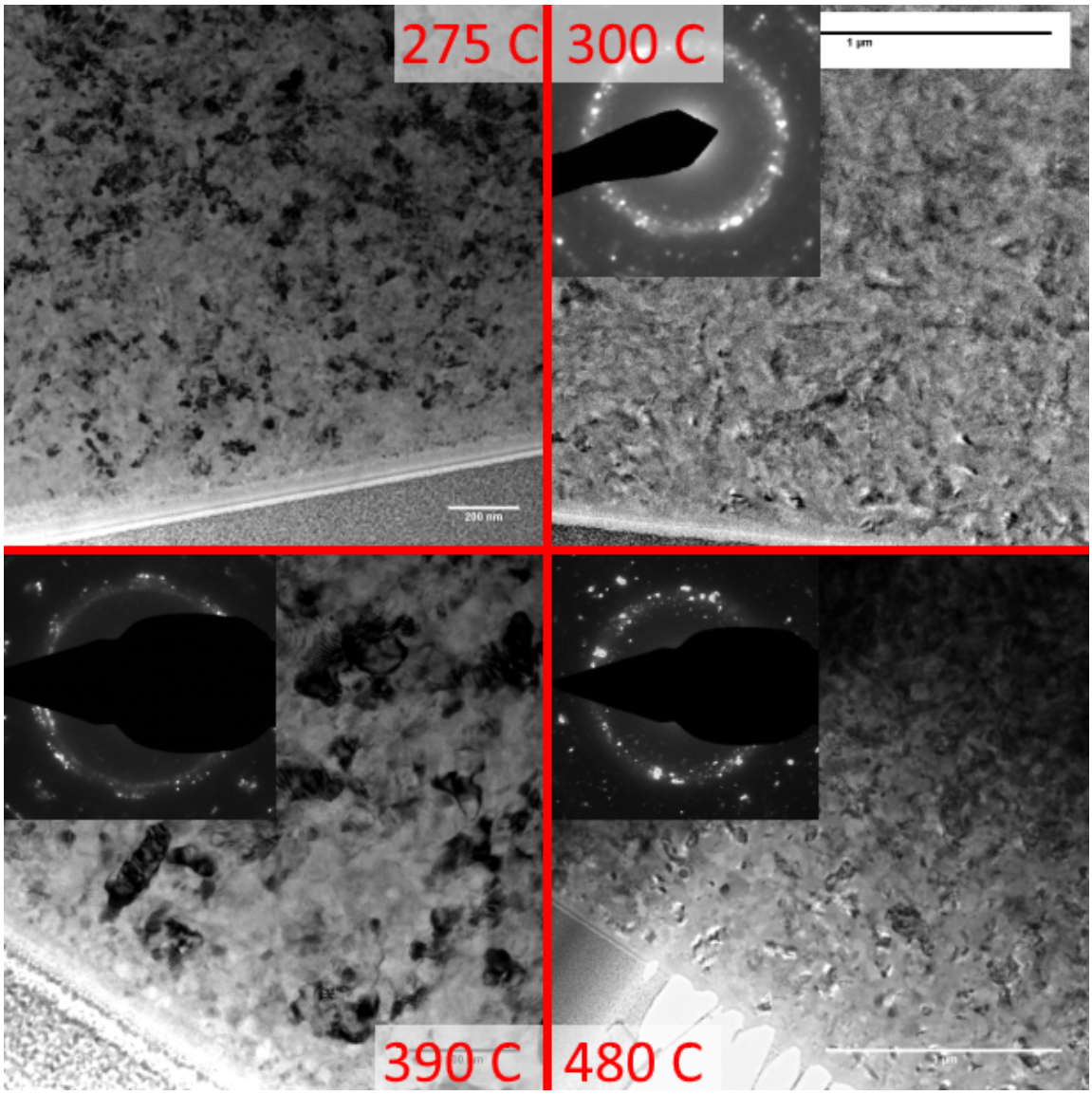

Figure 6.6: Bright field micrographs of samples from 275-480 °C.

injected interstitials or negative excess free volume. These areas of abnormally high and abnormally low packing density will interact with each other and cancel out, removing the excess free volume. This cancellation effect can be seen clearly in Figure 3.4 on page 64 where large sections of the sample are net zero for created vacancies and interstitials.

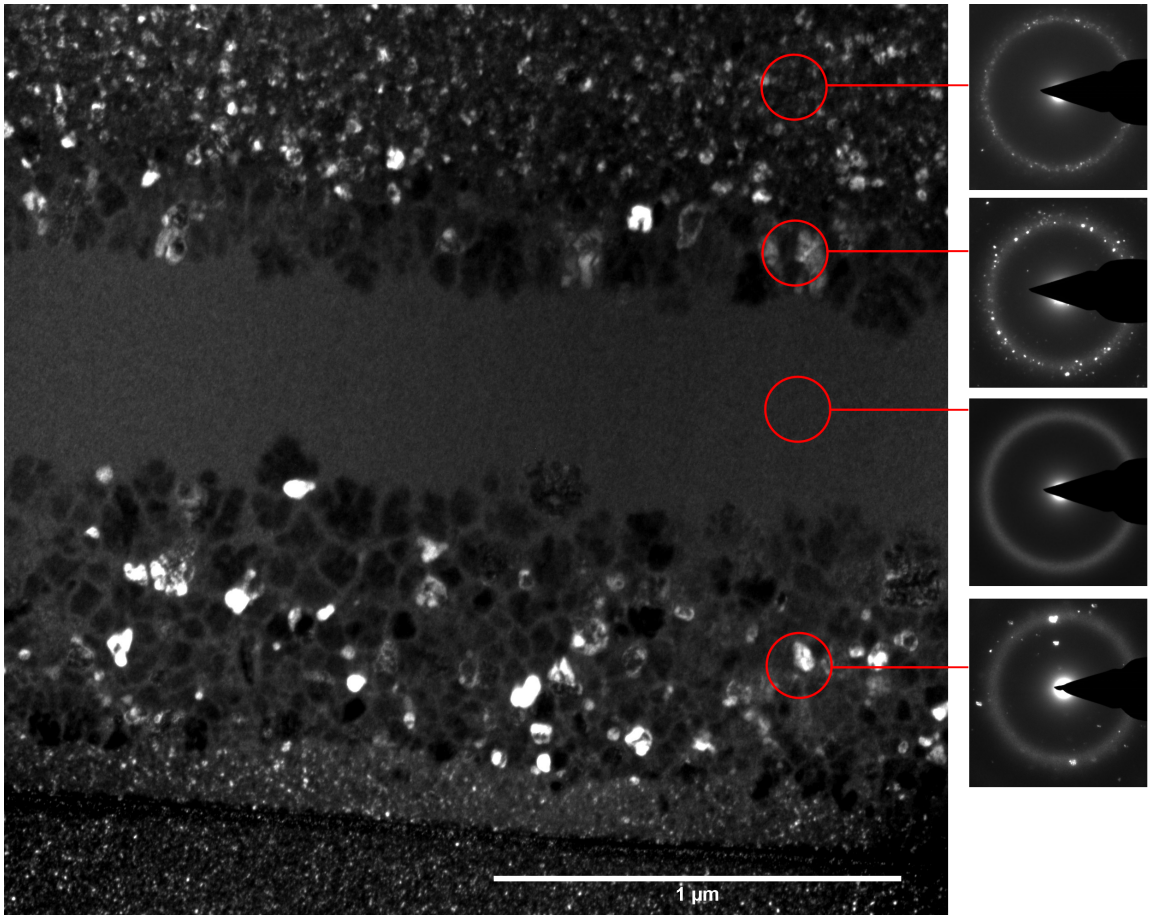

Figure 6.7: Dark field micrograph with labeled diffraction patterns showing the structure in different layers.

Second, the thin film samples are only able to relax in two directions. The structure is too thin to allow for any significant relaxation in the third axis. However, for the bulk sample, the third axis is available, leading to more material which is able to relax around the areas of excess free volume, reducing its ability to increase atomic mobility to a point where crystallization can occur.

6.3.2 275 to 480 °C

From TEM observation, the samples have become completely crystallized, far beyond the projected range of the ions. The best explanation for this phenomena

is that the beam is simply heating the sample until it is above the crystallization temperature. A simple calculation was performed to confirm this. Using two 1-D steady state conduction models and the known energy and intensity of the beam, a pure conduction heat transfer calculation was performed to predict the temperature that the near surface region was elevated to during irradiation. The full heat transfer calculation can be seen in Appendix A.

Using 275 °C as a test stage temperature the model was run using reasonable values to determine the maximum temperature achieved by the sample. The temperature curves for a metallic glass ribbon along the length, and in the direction of the beam can be seen in Figure 6.8

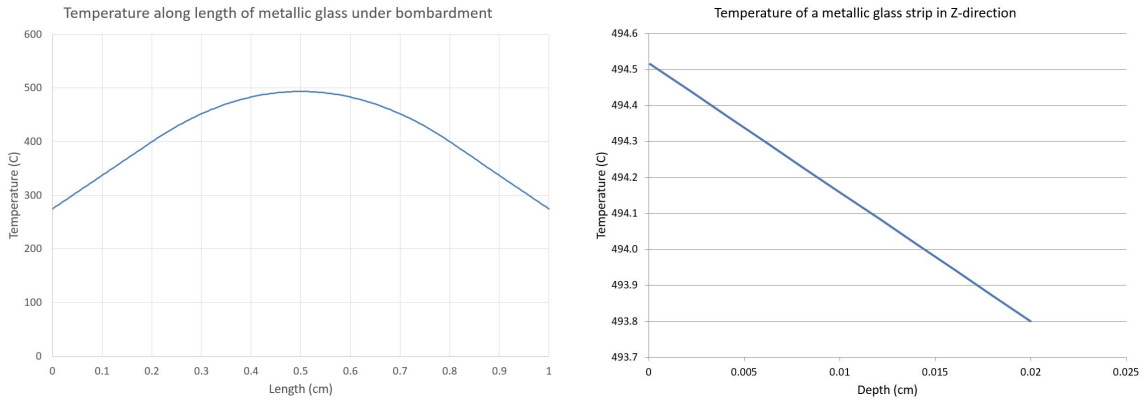

Figure 6.8: Plot showing the temperature curves along the length and through a metallic glass ribbon

AS can be seen by this calculation, beam heating can easily raise the center of the sample to within a few degrees of the crystallization temperature. This model does not take into account temperature gradients caused by the silver paste, but that will also play a role, increasing the ultimate temperature seen at the surface of the metallic glass. This model also shows that the temperature gradient along the

direction of the beam is largely negligible. This explains why the metallic glass is observed to be crystallized all the way through the sample. If the gradient in the direction of the beam was significant, then partial crystallization would be observed.

6.3.3 250 °C

For this sample, a multi-part structure was observed. This structure is a result of a few different steps that occurred. The complex structure is mostly a consequence of the sample being held on the edge of the critical temperature to cause thermal crystallization by beam heating.

Early in the irradiation, either due to a fluctuation in beam current or substrate temperature, the sample was raised slightly above the crystallization temperature, causing mass crystallization through the sample. With the sample so close to the critical temperature, even a small change could have caused this to occur. After the mass crystallization, the sample temperature or beam current lowered, causing the sample to return to under the critical crystallization temperature. Now the beam began to re-amorphize the sample. As seen in the lower temperature samples, the beam cannot cause direct crystallization. However, it does cause damage cascades, which will locally melt and re-quench faster than the critical cooling rate, causing the crystalline material to re-amorphize. As can be seen in Figure 6.7, the sample does not fully re-amorphize. This is due to the damage cascade shape. The majority of the energy from a damage cascade is deposited over a certain range from the surface. A SRIM plot of the DPA as a function of depth can be seen in Figure 6.9.

As can be seen in Figure 6.9, the amorphous band perfectly matches with the peak of the DPA curve. In this region there is the most energy deposition, and the core of the damage cascade. In that band the DPA rate is high enough to prevent any further crystal growth from occurring even at this elevated temperature.

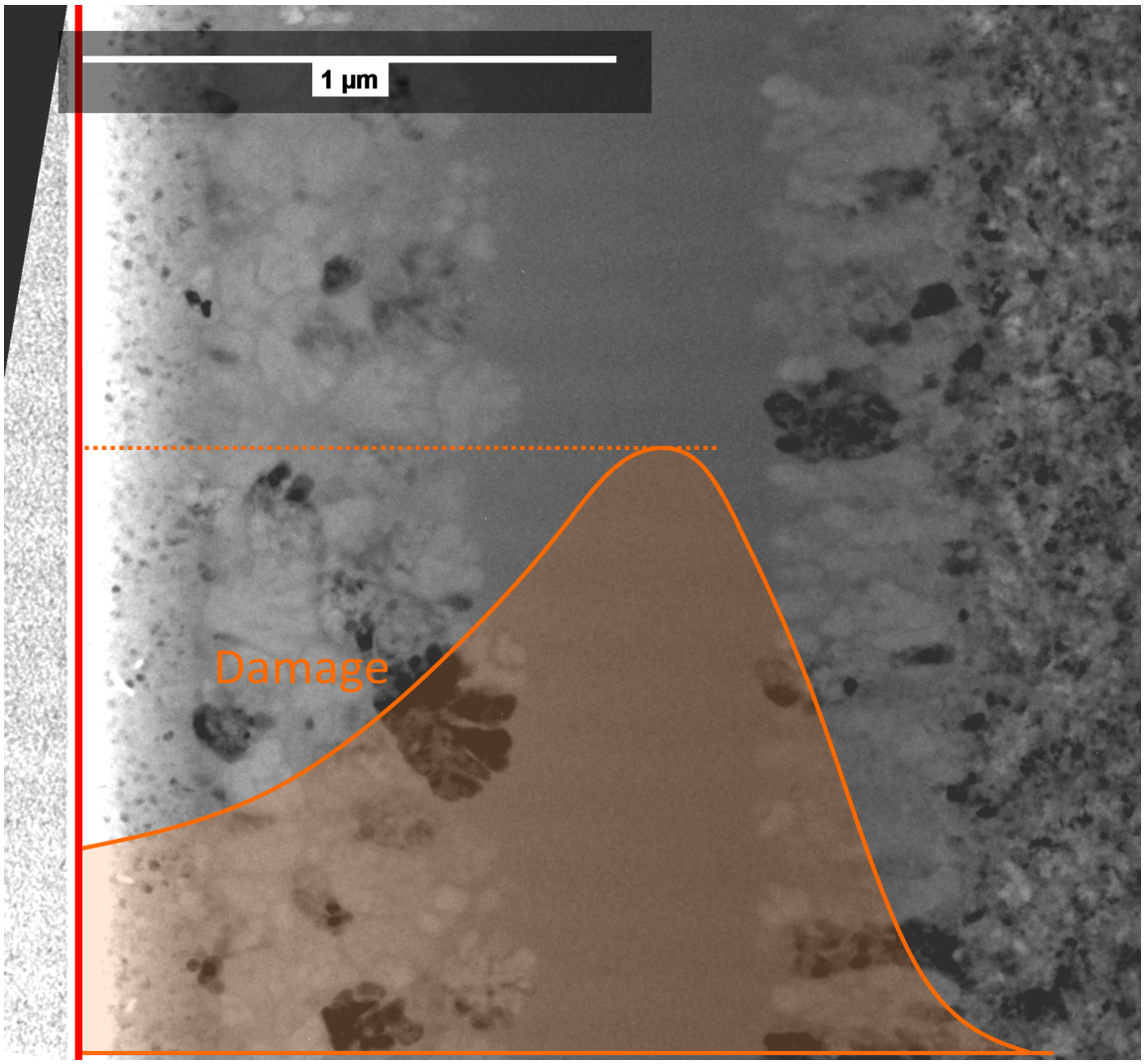

Figure 6.9: Bright field micrograph of the 250 °C sample with DPA curve

However, in the lesser damage regions, there is not enough heat to locally melt the sample, only enough to heat it to high temperature. This results in an increased thermal budget for diffusion. The increased thermal budget as well as ion-induced mixing allows for those crystals to form and grow.

6.4 Conclusions

As shown in this study, the metallic glass is very resistant to crystallization by direct ion bombardment. It was also shown that by heating the substrate to above a certain temperature with a given ion flux, the sample would fully crystallize through heating. Around the critical temperature a unique layered structure was seen which is attributed to a multi-step process made possible by the close proximity of substrate temperature to the critical crystallization temperature. More importantly, this study suggests that, for bulk samples, the ion beam cannot cause direct crystallization by creation of excess free volume. It is suggested that this is due to two processes: injected interstitials from the beam, reducing overall excess free volume, as well as multi-directional relaxation of the matrix around any sites that do have excess free volume.

7. BULK STUDIES: FLUENCE DEPENDENCE

In this chapter, experiments are performed on bulk metallic glass ribbons. More specifically, this study examines the effects of increasing fluence on the microstructure of the metallic glass. Two temperatures were chosen for these experiments, room temperature and 250 °C. These temperatures were chosen due to the observations made in the last set of temperature dependent samples. Initially the samples were crystallized either purely by heating or heating by ion bombardment. Next, the samples were bombarded to various fluences at either 250 °C or room temperature.

It was found that under bombardment at room temperature, after crystallization by ion beam heating, the near surface region was amorphized from its crystalline state. For the 250 °C irradiations, each stage of the multi-layer structure was seen to develop. At very low fluences, the sample is completely amorphous in the near surface region, however, with increasing fluence, re-crystallization was seen to occur until the layered structure seen in Figure 6.7 developed. For the samples that were crystallized purely by heating, re-irradiation at room temperature was able to briefly re-amorphize the samples at a low dose, but there was significant elemental segregation observed. With increasing fluence, the near surface re-crystallized. The mechanisms behind these observed phenomena are explored in this chapter.

7.1 Experimental Design

The samples used in this experiment were fabricated using the melt-spun ribbon technique. The composition used for all studies is $Ti_{40}Cu_{31}Pd_{15}Zr_{10}Nb_7Sn_2Si_3$. This composition was chosen due to its good glass forming ability as well as its wide supercooled liquid region. DSC curves to determine temperature points were performed initially. A plot of the DSC curve can be seen in chapter 3 in Figure 6.1.

Table 7.1: Table showing the different doses post-crystallization that each of the samples received. Fluence values are reported in ions/cm^2.

Processes	1E13	1E14	1E15	1E16	1E17
Ion Crystallized + Room Temperature Irradiation		X	X	X	X
Ion Crystallized + 250 °C Irradiation		X	X	X	
Thermal Crystallized + Room Temperature Irradiation	X	X	X	X	

To start, all samples were crystallized using 3.5 MeV Cu ions with a substrate temperature of 350 °C. These conditions were chosen based on the results from the temperature dependent experiments. Next, the samples were further irradiated at lower temperatures to different doses in order to see how the microstructure evolved. The secondary irradiation doses as a function of their temperature can be seen in Table 7.1.

After both irradiation stages were performed, an electron transparent sample was created using the FIB lift-out technique. TEM was then performed on the sample to characterize the crystal and amorphous structures created.

7.2 Experimental Results

The first samples examined were the samples crystallized by ion bombardment, and re-irradiated at room temperature. For these samples, the near surface was seen to become re-amorphous by 1E14 ions/cm^2 and stayed that way all the way up to the final test fluence of 1E17 ions/cm^2. Images of the samples can be seen in Figure 7.1.

The next samples examined were the samples crystallized by ion bombardment and re-irradiated at 250 °C. For these samples, it was observed that at 1E14 ions/cm^2

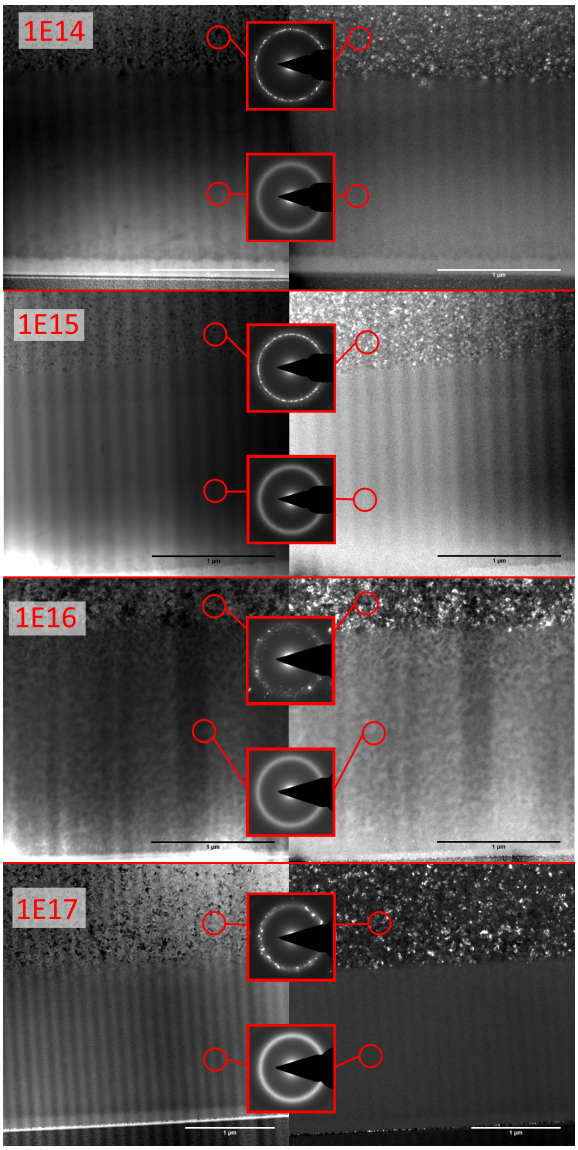

Figure 7.1: Bright field, dark field and diffraction pattern images of samples crystallized by beam heating, then re-irradiated to the indicated fluence at room temperature by 3.5 MeV Cu.

the sample near surface region was completely amorphous up to the end of ion range. After this, increasing fluence started to re-crystallize the sample starting from the edges of the amorphous region, as observed after irradiation up to 1E15 ions/cm^2. The crystallization grew and coarsened until a defined amorphous band surrounded

by large crystal grains formed at 1E16 ions/cm^2. Images of each of these stages can be seen in Figure 7.2.

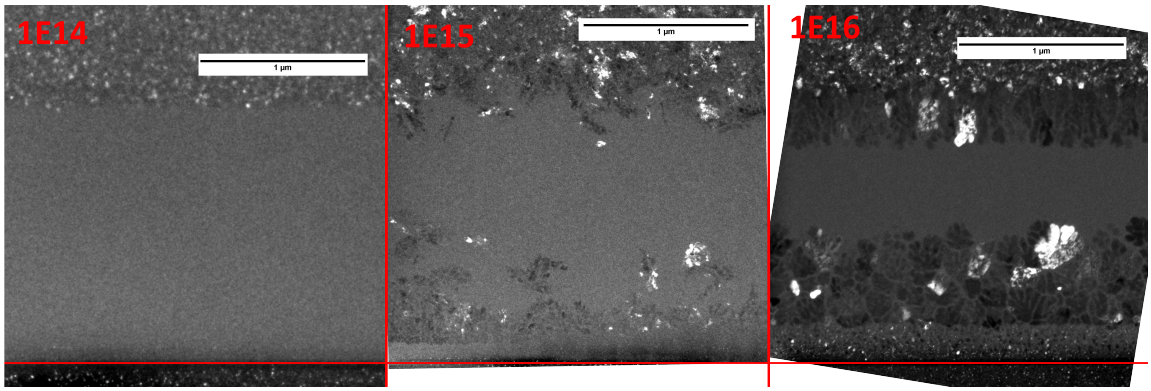

Figure 7.2: Dark field TEM micrographs of samples initially crystallized by irradiation at 350 °C, then re-irradiated to the indicated fluences at 250 °C.

Lastly, the samples that were crystallized purely by heating and then bombarded at room temperature were observed. To ensure the sample was completely crystallized, resistance measurements of the sample were taken. The sample was heated and the was resistance measured by using the voltage comparator method and a lock in amplifier. It is well documented that the resistance of metallic glass decreases upon crystallization [27]. The metallic glass used in this study is no exception. A plot of the resistance as a function of temperature can be seen in Figure 7.3. The large drop in resistance, followed by a stable resistance upon cooling shows that the sample achieved complete crystallization.

With the sample completely crystallized, it was irradiated using 3.5 MeV Cu ions at room temperature to various fluences. At 1E13 ions/cm^2, a partial re-amorphization was observed, and at 1E14 ions/cm^2 the near surface was fully re-amorphized, but segregated. After that the near surface became increasingly crys-

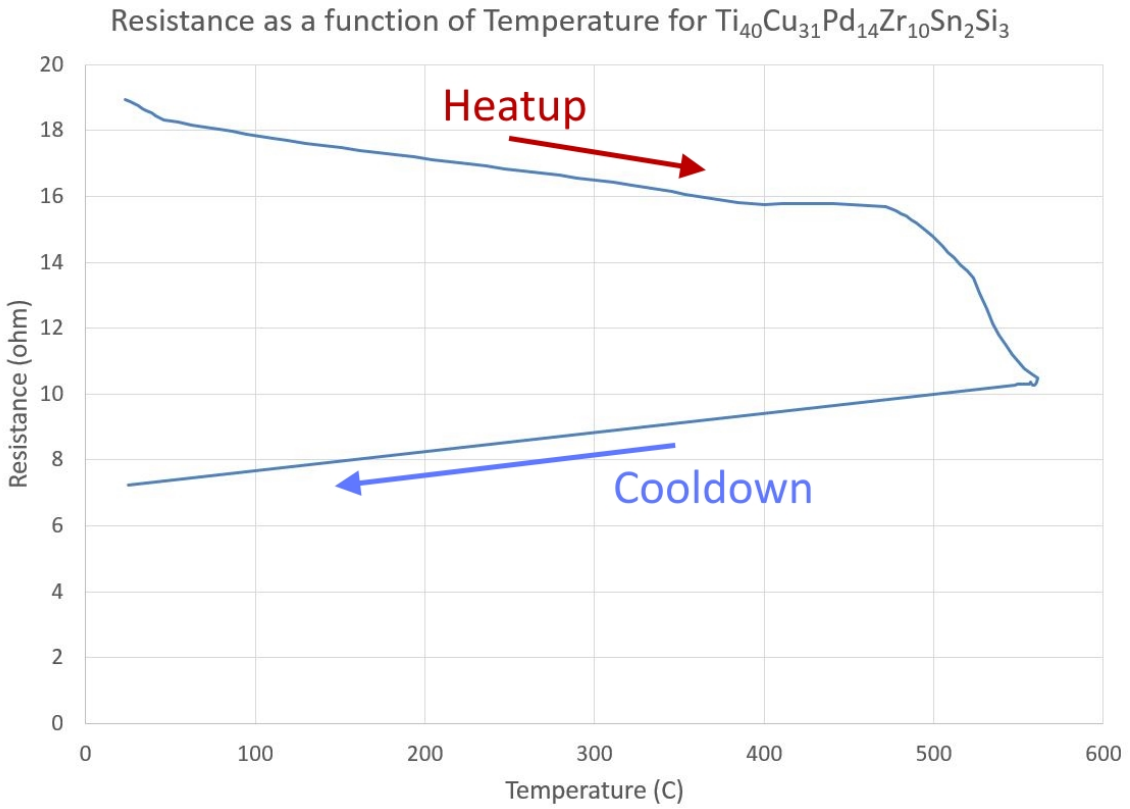

Figure 7.3: A plot of the resistance of Ti_{40} Cu_{31} Pd_{15} Zr_{10} Nb_7 Sn_2 Si_3 metallic glass as a function of temperature.

tallized with increasing fluence up to 1E16 ions/cm^2. Images of all of the samples can be seen in Figure 7.4.

7.3 Results: Discussion

As can be seen by the three cases of treatments, there is an evident connection between the phase of the sample, the temperature of irradiation, the DPA and even the crystallization history of the sample. Further examination of these effects will show how these different effects come into play.

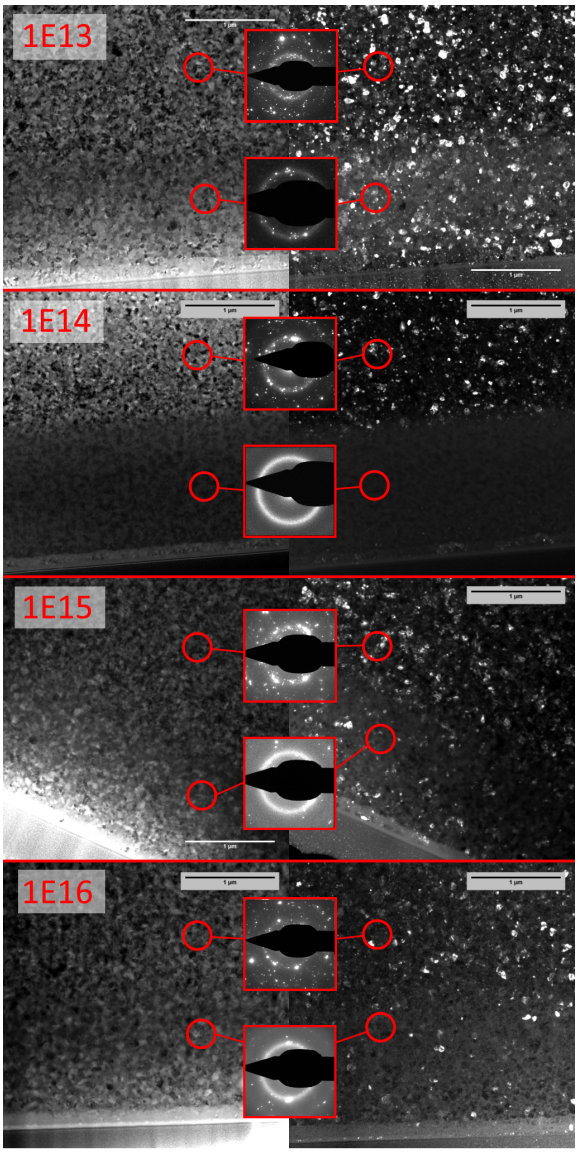

Figure 7.4: Dark field, bright field and diffraction patterns of samples initially crystallized by thermal crystallization, then re-irradiated to the indicated fluences at room temperature.

7.3.1 Beam Crystallization + Room Temperature Irradiation

As can be seen in Figure 7.1 the samples re-irradiated at room temperature after crystallization by beam heating had a completely amorphous near surface region.

All through the ion range, even up to a very high fluence, the near surface remained amorphous. This shows that overall the beam drives the metallic glass to be amorphous. Far from causing direct crystallization in bulk samples, it has the ability to reverse crystallization. This is an extremely desirable characteristic for implementation in a nuclear setting, as ion bombardment, which causes massive damage to the microstructure is unable to directly cause crystallization.

7.3.2 Beam Crystallization + 250 °C Irradiation

For the samples re-irradiated at 250 °C after crystallization by ion bombardment, the story is quite different. As can be seen in Figure 7.2, the sample is initially re-amorphized by the beam, however, with increasing dose, the sample re-crystallizes. This is quite peculiar behavior, but can be explained by the temperature that the sample was re-irradiated at. With the sample fully crystallized, the elements within the metallic glass have been segregated into more stable compositions for crystal formation. When the secondary irradiation begins at a lower temperature (250 °C), the ion bombardment is able to cause enough damage to remove any crystal structure that was created. However, since the substrate temperature is elevated, diffusion is allowed to occur. Elements are still segregated into pockets of stable crystal compounds from the initial crystallization, and so, with time, form more stable crystal structures which are able to survive the ion bombardment. The amorphous band, which exists at the peak damage depth of the beam, is subject to such a high DPA rate, no stable crystals can form.

This process is supported by the observations at 1E15 ions/cm^2. The sample begins crystallizing from the edges of the amorphous band, where the ion beam damage is less. In this area it is easier for crystals to form since the re-amorphizing effect of the beam is lessened. As more stable crystal structures from, they are

allowed to grow since the surrounding substrate contains all of the elements required to continue growing the crystal structure.

It is also important to note that the crystals beyond the projected range did not grow or coarsen, this again shows a role ion bombardment plays in the formation of this crystal structure. The crystals formed at the edge of the amorphous band are stable under ion bombardment, but in order to grow, the elements that they are made of must be brought into contact with the crystal surface. In the bulk, the crystals themselves lock the atoms in place, not allowing the crystals to grow. However, within the ion bombarded region, ion mixing shuffles the atoms around allowing crystal growth to take place. A diagram outlining this idea is shown in Figure 7.5.

7.3.2.1 Crystal Analysis by Energy Dispersive Spectroscopy (EDS)

The hypothesis that the crystals formed at the edges of the high damage region are a more stable structure than the bulk metallic glass must be further investigated. This analysis was performed using EDS. In this technique, the electron beam of the TEM is highly focused and impinges only on a small area of the sample. As the electrons interact with the material, they will produce characteristic X-rays which can be recorded using a silicon lithium (SiLi) drifted detector.

The crystals formed at the edge of the layered structure are too small to analyze their structure, however, the composition, which can be investigated, should vary from the original composition of the MG. In order to investigate this, EDS was performed at several points along the sample. Initially line segments 600 nm long were sampled from the specimen at 200 nm intervals from the surface. The line segment, rather than point geometry was chosen in order to homogenize the spectra collected. The resulting spectra can be seen over a dark field image of the sample in

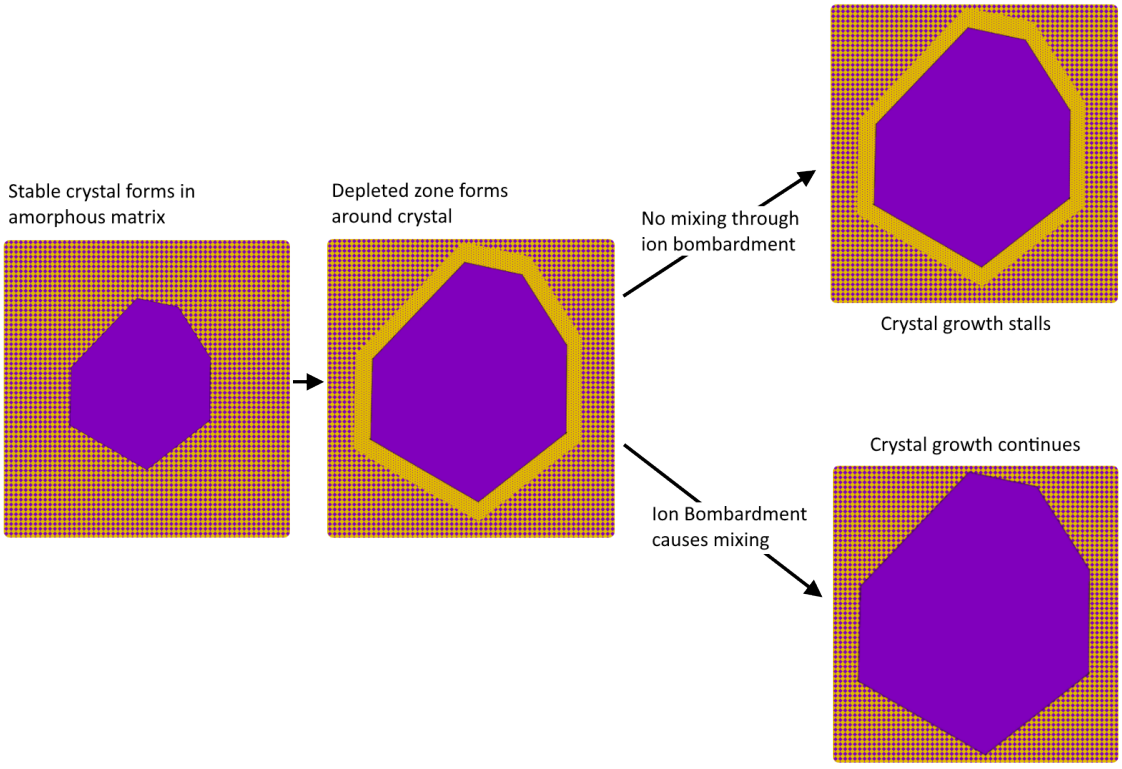

Figure 7.5: Diagram showing the crystal growth enhancement due to ion mixing

Figure 7.6. The same plot with 2σ error bars can be seen in Figure 7.7.

This plot shows that there is indeed some composition change going on. It is clear that, especially near the amorphous band edges, there is an elemental segregation occurring. The Pd in particular seems to be strongly effected by the crystallization process, and is depleted on the crystal-amorphous interface. The other elements show trends that are opposite to this, but this may be a consequence of the strong change in the Pd signal.

It should also be noted that these plots also give a strong indication of extensive carbon and oxygen contamination for the first 200 nm in the sample. It is unclear as to if this contamination happened during the production or irradiation of the metallic

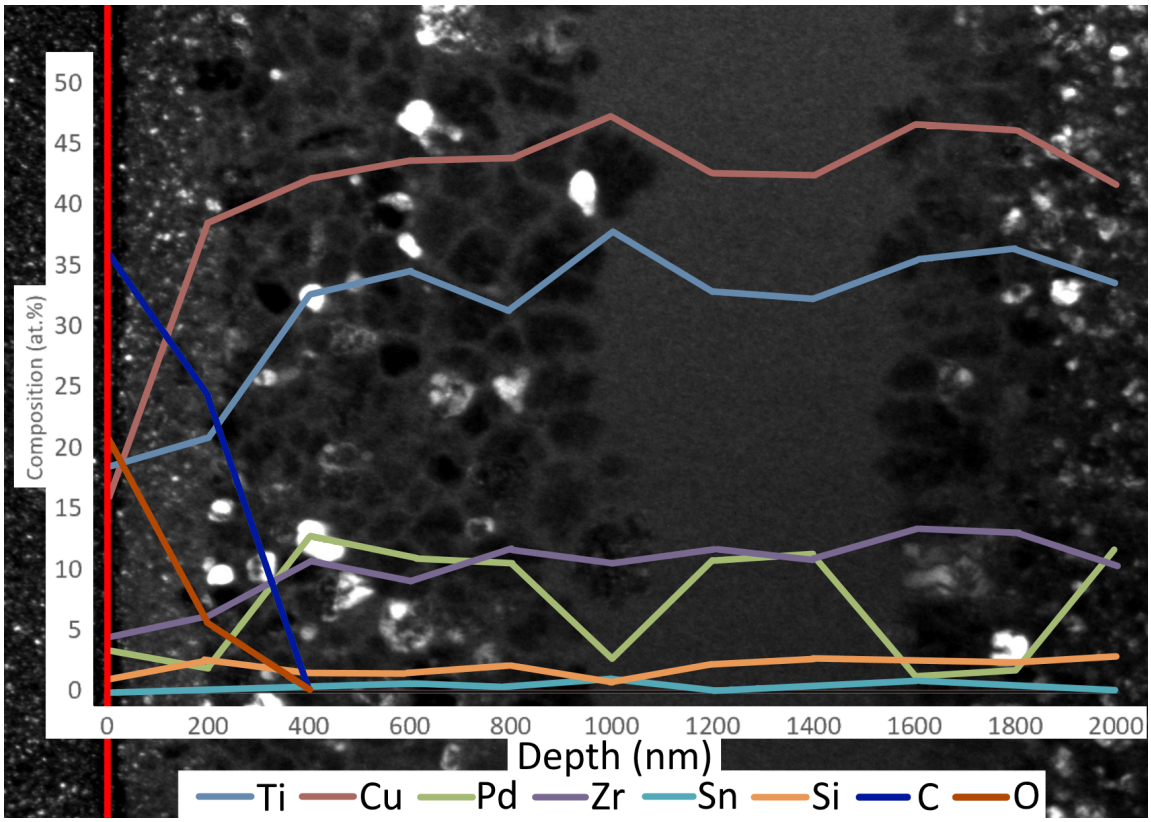

Figure 7.6: A plot of the composition of the sample as determined by the EDS data as a function of depth over a dark field image of the sample. Each data point in the averaging of properties along a 500 nm segment at that depth.

glass, however, since the oxygen and carbon signal are completely absent past 200 nm, it is unlikely that this contamination significantly effected the microstructure beyond that range.

Next, some point measurements were taken inside the crystalline region. This was done in order to see if different crystal grains have varying compositions. It is expected that if crystallization preferential structures are being made the composition will vary from crystal to crystal. An image showing the sampling locations and the average sampling location can be seen in Figure 7.8.

These four points each exhibit different compositions. For some elements, such

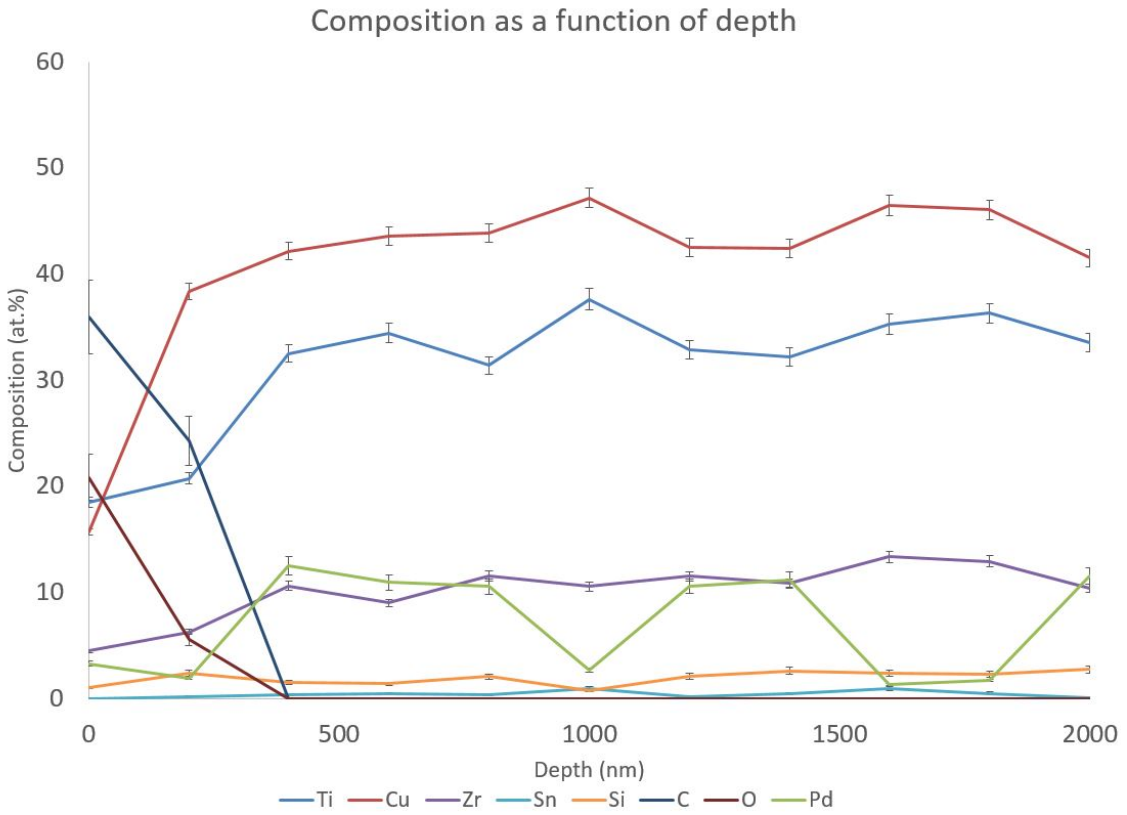

Figure 7.7: A plot of the composition of the 250 °C 1E16 ions/cm^2 sample as determined by the EDS data as a function of depth. Each data point in the averaging of properties along a 500 nm segment at that depth. error bars reported at 2σ.

as Ti and Cu, the differences are relatively small. However, for Pd and Zr there are large differences in the percentages. This shows that the crystals formed are indeed different compositions to some extent. Lastly, scanning TEM (STEM) was used to image the sample. This type of imaging is useful in this case since it is not sensitive to diffraction contrast, as is the case in bright field and dark field TEM. That means that contrast is primarily generated by differences in composition. The STEM image of this sample can be seen in Figure 7.9.

Overall, all of this data does show that there is a change in composition between crystals as well as a difference between the crystals and the amorphous bulk. This

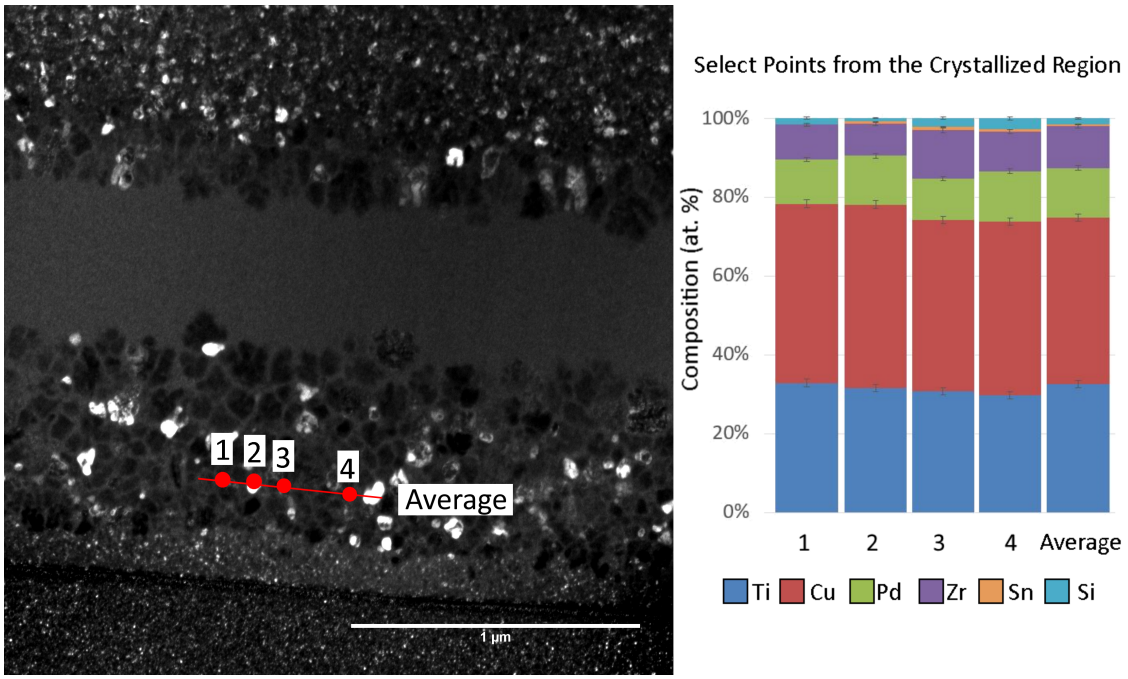

Figure 7.8: Plot showing the composition of the sample at four different locations and an average composition along a 600 nm long line. Error bars reported at 2σ.

evidence supports the idea that these crystals are able to survive in the lower level ion damage regions due to their more stable composition.

7.3.2.2 5 MeV

In order to see if the layered structure could be replicated at a different depth, a sample was crystallized with the same beam heating method, then re-irradiated to 1E16 ions/cm^2 with 5 MeV Cu at 250 °C. The results can be seen in Figure 7.10.

As can be seen in the micrograph, the sample has been re-amorphized throughout the ion range. This result is quite different from the irradiation with 3.5 MeV Cu. This is due to the reduced beam heating effect. Since this irradiation was performed at a higher energy, the beam current is machine limited. Since the beam flux was lower, the true sample temperature is also lower. This reduces the ability of the atoms

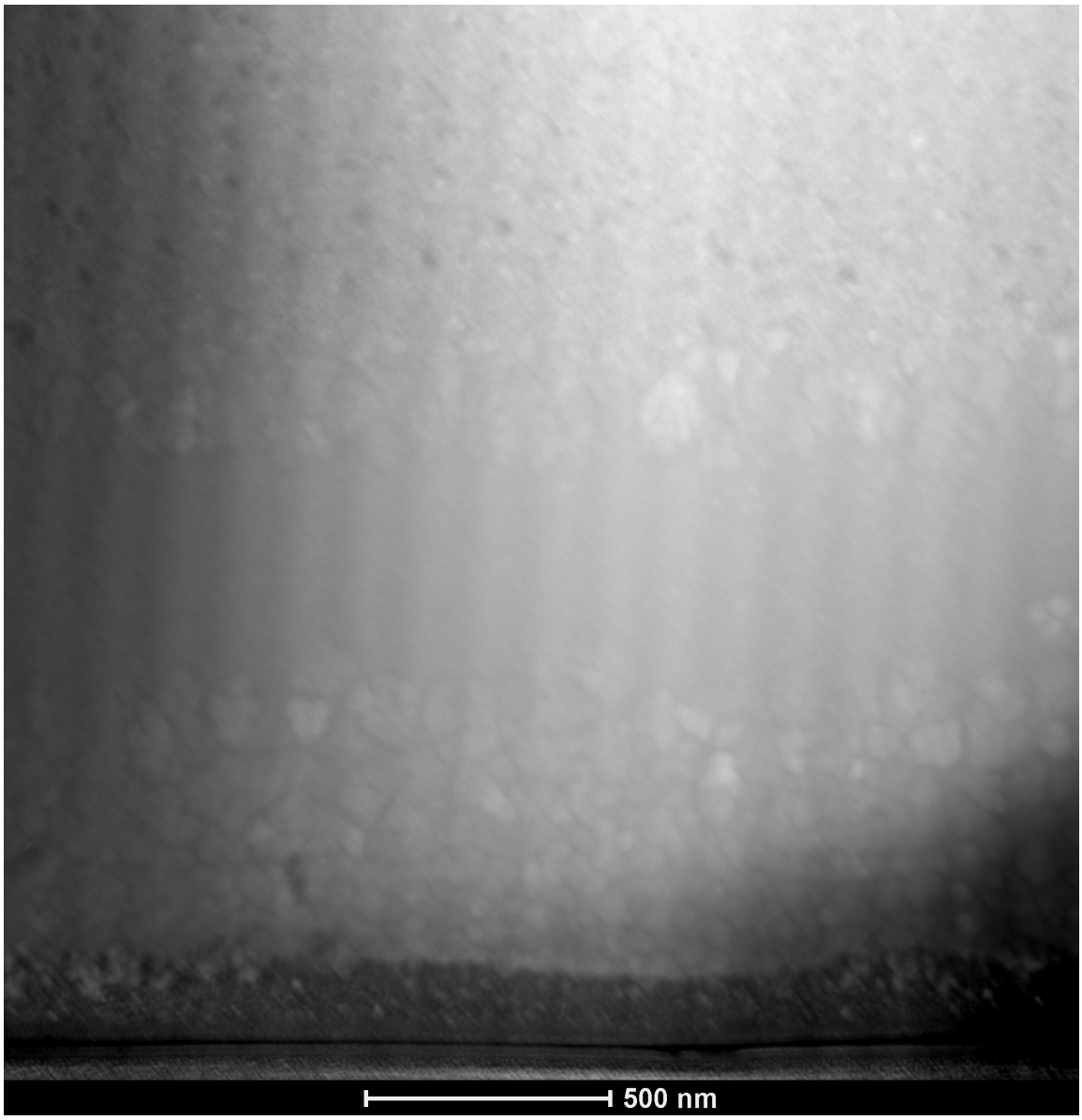

Figure 7.9: STEM micrograph showing the irradiated region for the 1E16 ions/cm^2 at 250 °C.

to migrate and form stable crystal compounds. This results in the same phenomena that was observed in the room temperature irradiations, where no-recrystallization was observed.

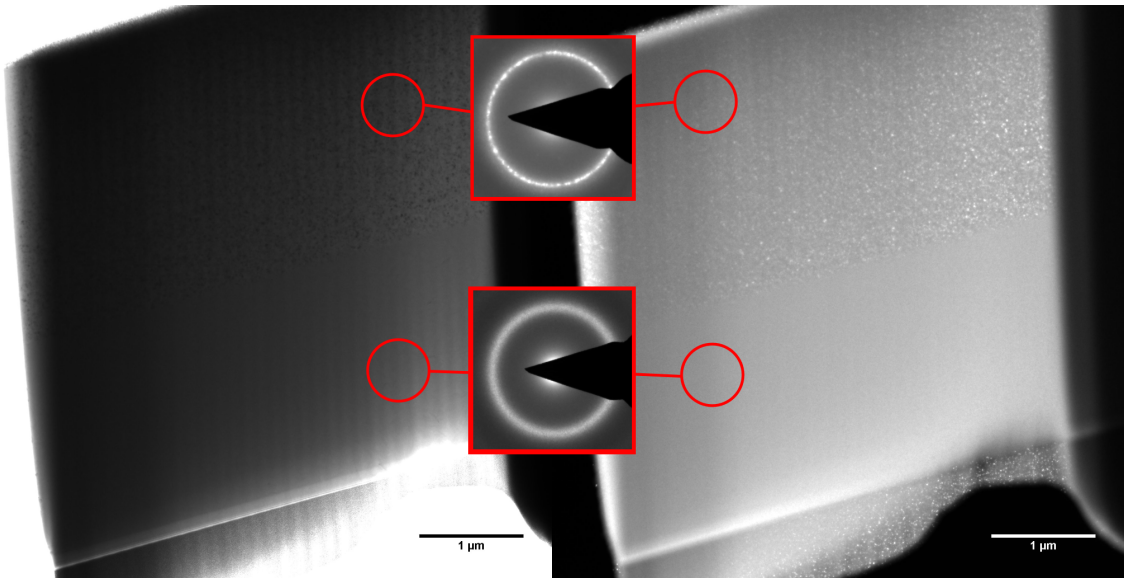

Figure 7.10: Bright field, dark field and diffraction pattern images of Ti_{40} Cu_{31} Pd_{15} Zr_{10} Nb_7 Sn_2 Si_3 metallic glass crystallized by ion bombardment at 350 °C and re-irradiated at 250 °C to 1E16 ions/cm^2 by 5 MeV Cu.

7.3.3 Thermal Crystallization + Room Temperature Irradiation

The thermally crystallized samples re-irradiated at room temperature were a great illustration of the two process discussed in the previous samples. The thermally crystallized samples showed large amounts of segregation based upon the crystallization step. This shows that the crystal structures formed after crystallization is not the original composition of the metallic glass. With the applied heat, the elements are able to diffuse and form more stable crystal forming compounds. This is especially evident in the case of the 1E14 ions/cm^2 sample, where the near surface region is completely amorphous, but obviously segregated. A more fully detailed micrograph can be seen in Figure 7.11. This sample is more highly segregated than the ion crystallized sample since there was no ion-induced mixing occurring when the sample crystallized. Due to this enhanced segregation, stable crystals were able

to form much more rapidly. As can be seen in Figure 7.4, the equilibrium structure forms much more rapidly. This study also shows the powerful amorphization power of the beam. Even with stable compounds formed, there is still a distinctly amorphous zone in the high damage rate region.

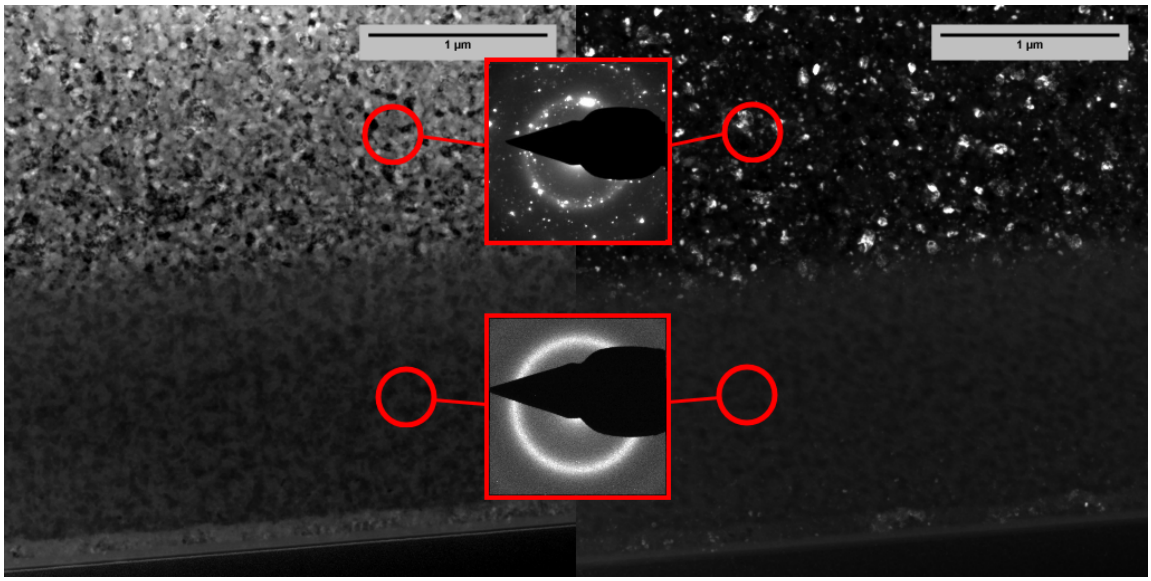

Figure 7.11: Bright field, dark field and diffraction patterns of the sample initially thermally crystallized then re-irradiated to 1E14 ions/cm^2 at room temperature

7.4 Conclusions

From these multiple-temperature experiments, several important correlations were able to be made between the crystallization causing diffusion effects and the amorphizing ion damage rate effect. The variable temperatures and diffusion rates all contributed to the final equilibrium structure achieved.

In the cases where the crystallized samples were irradiated at room temperature the diffusion effects were too little to overcome the re-amorphizing nature of the

beam. In that case, the samples were quickly re-amorphized and remained that way all the way to extremely high levels of DPA.

It was seen from observation of the 250 °C samples that metallic glass can remain amorphous even at an elevated temperature as long as the beam intensity is high enough to continue amorphizing the sample. In this case the DPA rate was high enough only to keep part of the ion bombarded region amorphous. The areas of lower damage rate were at a high enough temperature to nucleate crystals. Since the ion bombardment was continuing in that region, the matrix around the crystals was kept well mixed. In that case, it prevented a depleted zone from forming around the crystal, allowing the crystals to continue growing. This was in sharp contrast to the crystals outside the ion bombardment region, which did not see any crystal grain coarsening even with an extended time at an elevated temperatures.

The thermally crystallized samples were able to very clearly show the amount of segregation effected the ability of the beam to re-amorphize the metallic glass. It was observed that the sample was able to be re-amorphized at 1E14 ions/cm^2, however, unlike previous cases, the sample showed a distinct segregation of elements even after re-amorphizing. This segregation occurred since these samples were annealed at a much higher temperature than the samples crystallized with beam heating. This allowed for more stable and complete crystal formation in the thermally crystallized samples.

The patches of amorphous material seen in the 1E14 ions/cm^2 sample have a composition that closely matches the stable crystal compound of the crystal that was in that location before it was re-amorphized. The presence of this already stable crystal composition is what caused these samples to re-crystallize, unlike the beam crystallized samples that were re-irradiated at room temperature. IT can be seen that with larger doses, the area with the highest DPA rate

8. POROUS MG

In this chapter, a study is performed that looks at porous metallic glass. The porous MG was able to be fabricated using low energy He bombardment to very high doses at room temperature. Through this process, very large voids were formed in the MG while retaining the amorphous structure of the atoms. Next, the samples were irradiated with 3.5 MeV Cu at 350 °C in order to induce crystallization. Post-irradiation TEM analysis showed that this process was able to crystallize the sample fully. However, the previously created voids were also removed, making it impossible to determine if the thin film crystallization resistance seen in chapter 3 could be replicated in a bulk specimen.

8.1 Experimental Design

The samples used in this experiment were fabricated using the melt-spun ribbon technique. The composition used for all studies is $Ti_{40}Cu_{31}Pd_{15}Zr_{10}Nb_7Sn_2Si_3$. This composition was chosen due to its good glass forming ability as well as its wide supercooled liquid region. Intially DSC was performed in order to determine critical temperature points. A plot of the DSC curve can be seen in chapter 6, Figure 6.1 on page 82.

The ribbons were then bombarded with 100 keV helium to a fluence of 1E18 ions/cm^2. The expected DPA and He deposition as calculated by SRIM can be seen in figure 8.1 for these irradiation conditions.

A select sample was then bombarded with 3.5 MeV Cu at 350 °C. The conditions to cause crystallization were determined from the bulk studies temperature dependent experiments. After the Cu bombardment, electron transparent samples were prepared by FIB and examined under TEM.

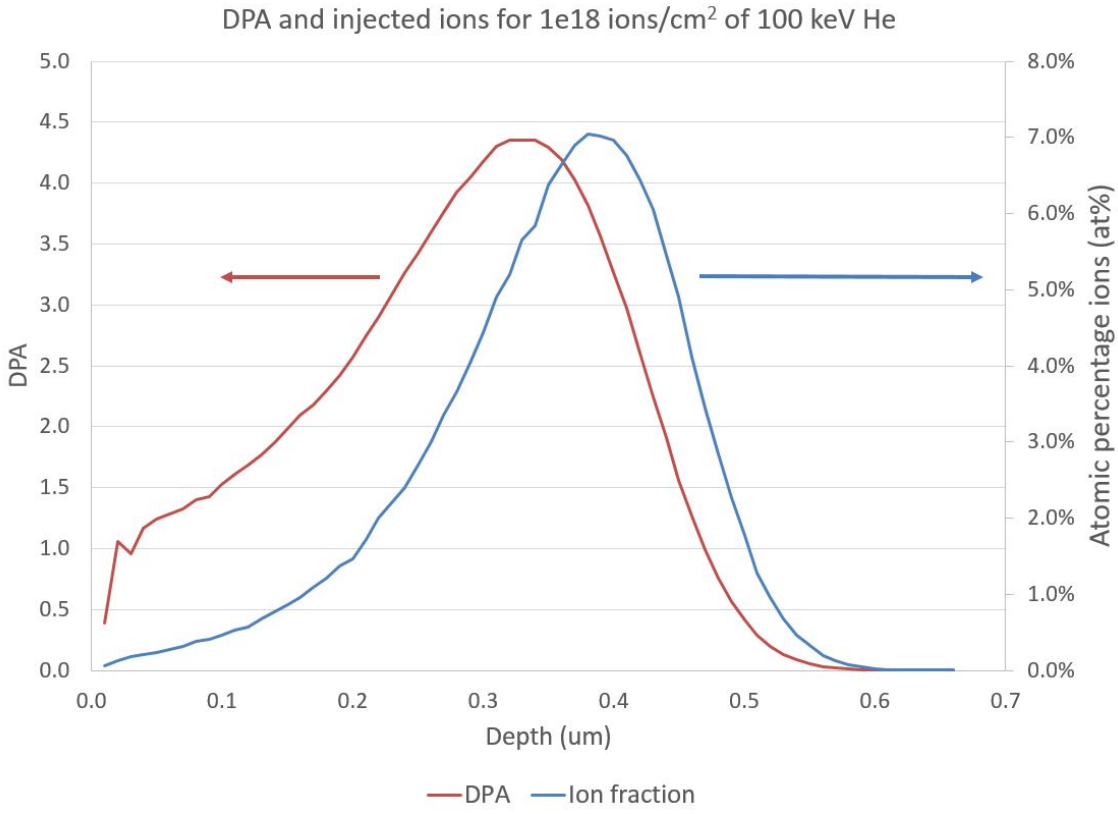

Figure 8.1: SRIM output showing the calculated DPA and ion atomic fraction for 1E18 ion/cm^2 of 100 keV He into Ti_{40} Cu_{31} Pd_{15} Zr_{10} Nb_7 Sn_2 Si_3.

8.2 Experimental Results

TEM micrographs of the sample after He bombardment to 1E18 ions/cm^2 can be seen in Figure 8.2. This sample was suitable to test and see if the ultra-thin film crystallization resistant properties could be seen in the thin films between the voids. Higher resolution pictures, highlighting the amorphous nature of the thin films between voids, can be seen in Figure 8.3.

The amorphous samples were also hardness tested to determine the effect the porous structure had on the mechanical properties. The data was compared against an untreated amorphous sample, and a fully crystallized sample. The hardness as a

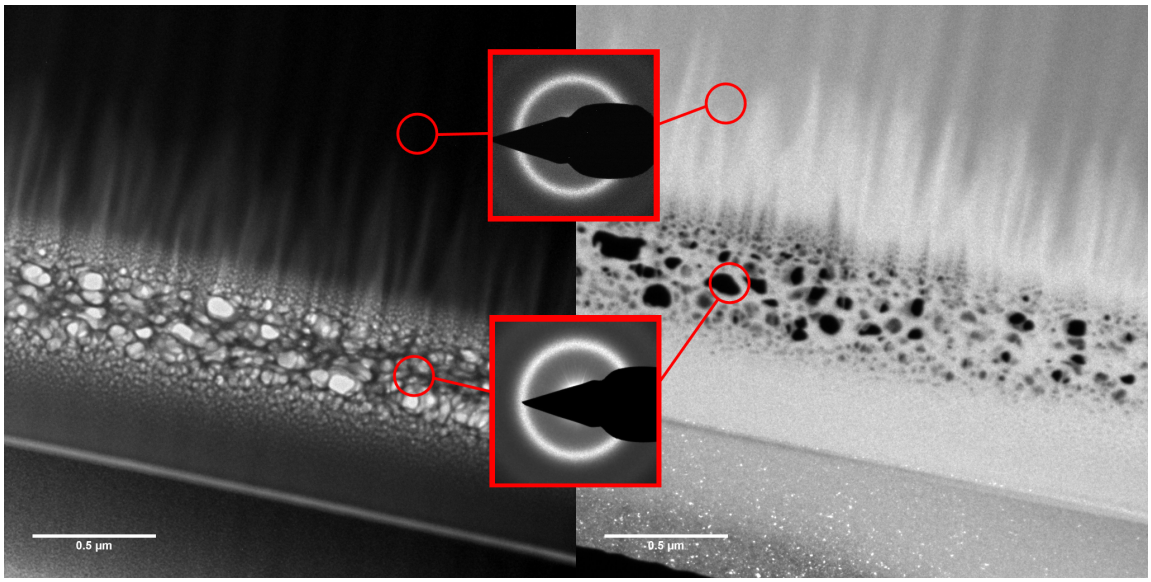

Figure 8.2: Bright field, dark field, and diffraction pattern images of Ti_{40} Cu_{31} Pd_{15} Zr_{10} Nb_7 Sn_2 Si_3 metallic glass after bombardment to 1E18 ions/cm^2 by 100 keV He

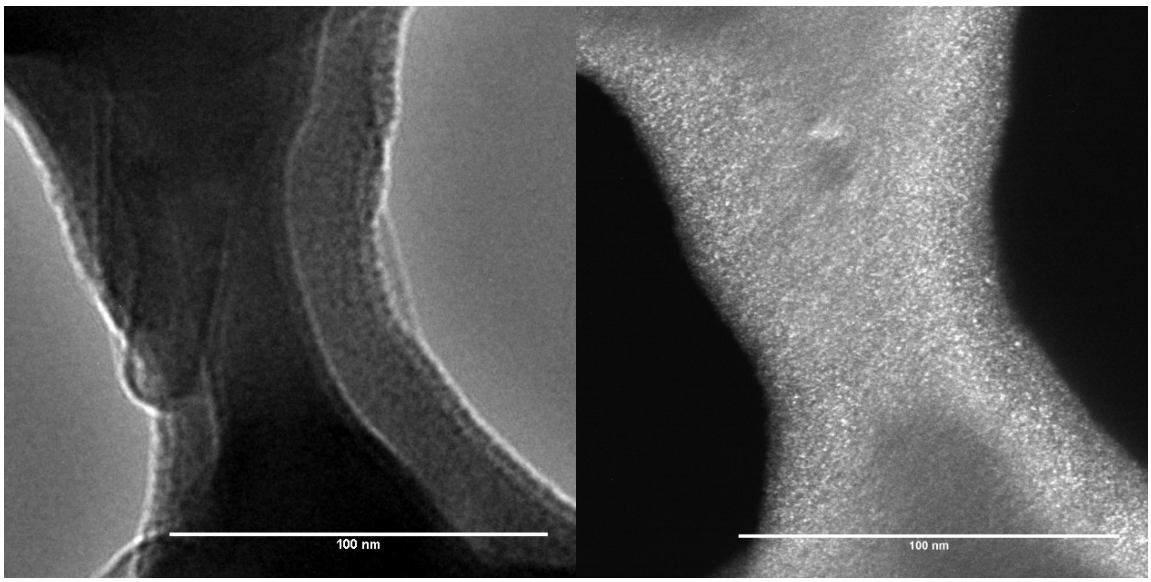

Figure 8.3: High resolution bright field and dark field images of Ti_{40} Cu_{31} Pd_{15} Zr_{10} Nb_7 Sn_2 Si_3 metallic glass film between voids after bombardment to 1E18 ions/cm^2 by 100 keV He

function of depth for each sample is presented in Figure 8.4.

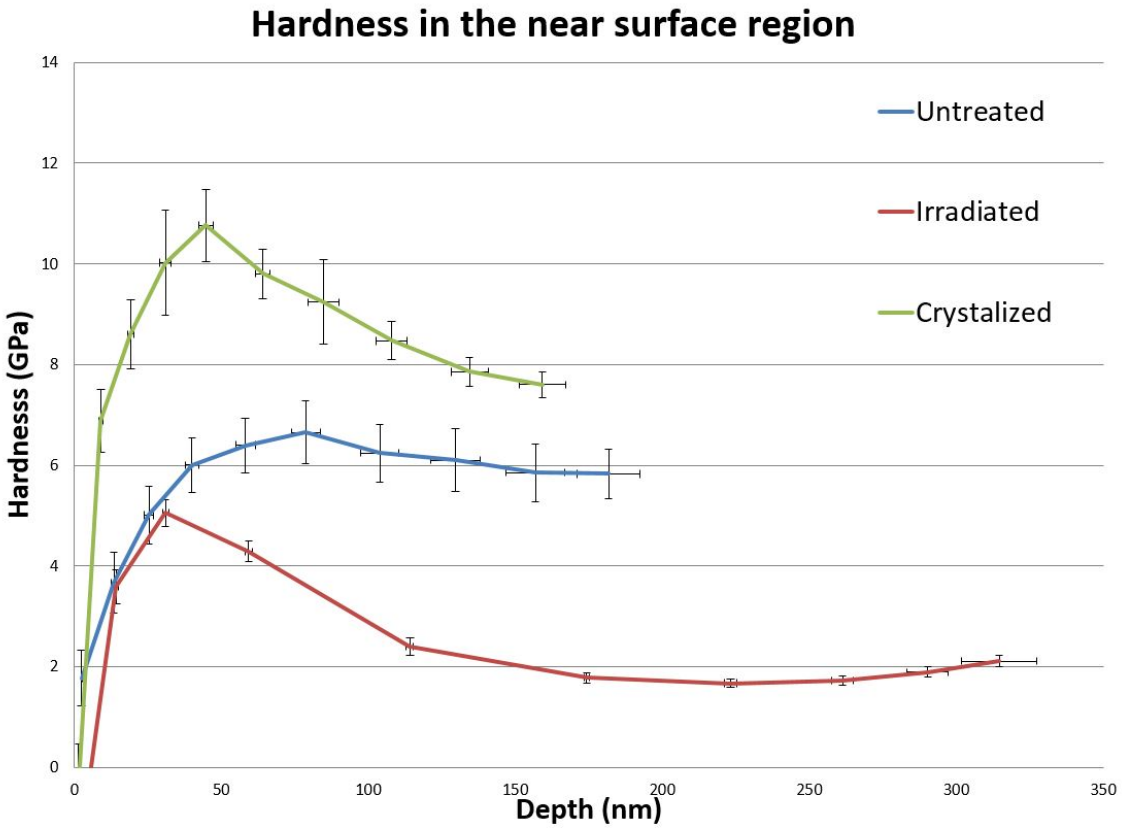

Figure 8.4: Nano-indentation data for a fully crystallized, untreated, and 100 keV He irradiated sample.

This data shows several interesting features. It is observed that the sample is much softer in the bubble region. This is not surprising given that the region has a very low density. In the near surface region the irradiated sample and the untreated sample are indistinguishable. This is also expected since there should be little deposition or ion damage in the near surface region. Lastly, it is interesting to note that the crystalline sample is much harder than the other two samples. These trends will be discussed in a later section.

The amorphous sample was then irradiated to 1E16 ions/cm^2 by 3.5 MeV Cu ions at 350°C to induce crystallization as had been seen in previous studies. After this irradiation, the sample was examined using TEM and found to have fully crystallized. This process also, unfortunately, removed the voids that had been produced in the previous step. The void structures mostly collapsed and moved towards the surface. This is unfortunate for the studies here, but not unexpected, since Helium is highly mobile, especially at elevated temperatures. The results of this treatment can be seen in Figure 8.5. There are a few voids that remain in the very near surface regions. However, the thin films that are left are fully crystallized , as can be seen in Figure 8.6.

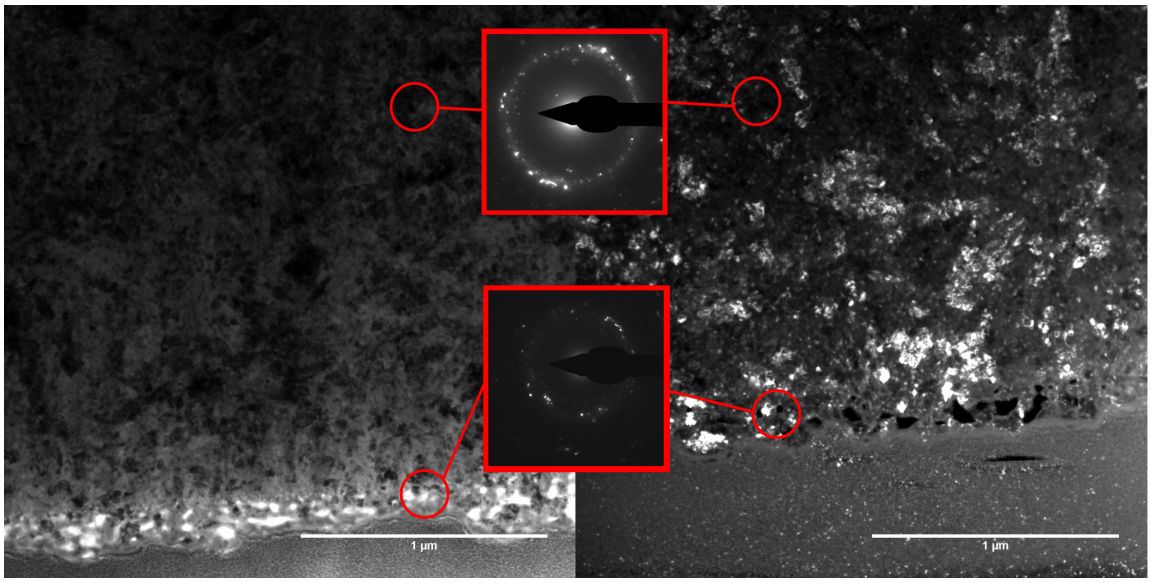

Figure 8.5: Bright field, dark field, and diffraction pattern images of Ti_{40} Cu_{31} Pd_{15} Zr_{10} Nb_7 Sn_2 Si_3 metallic glass after bombardment to 1E18 ions/cm^2 by 100 keV He and subsequent bombardment to 1E16 ions/cm^2 by 3.5 MeV Cu at 300 °C

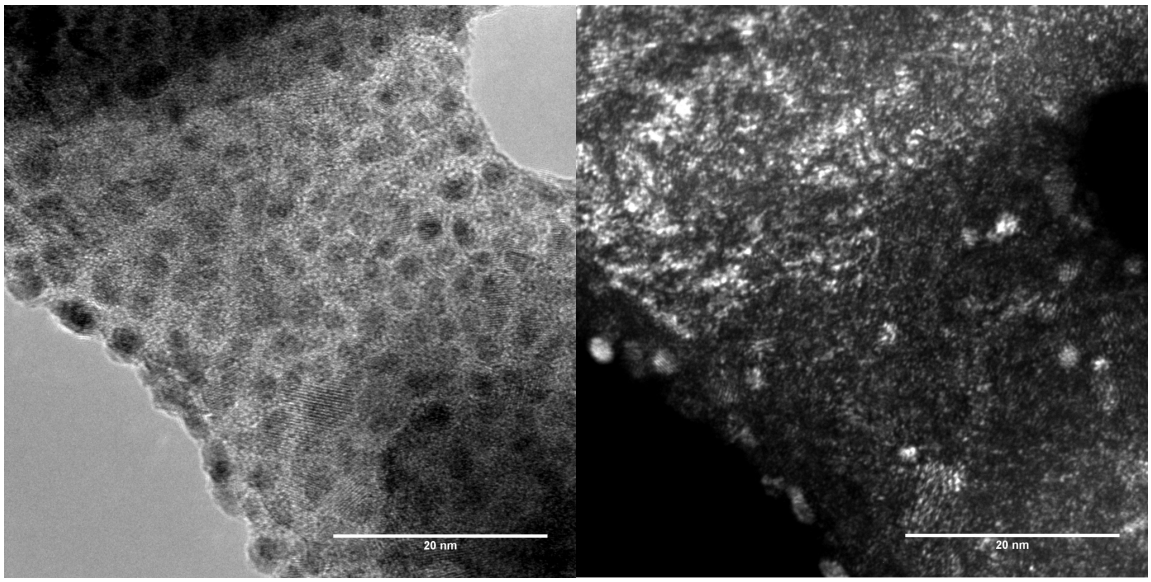

Figure 8.6: High resolution bright field and dark field images of Ti_{40} Cu_{31} Pd_{15} Zr_{10} Nb_7 Sn_2 Si_3 metallic glass film between voids after bombardment to 1E18 ions/cm^2 by 100 keV He and subsequent bombardment to 1E16 ions/cm^2 by 3.5 MeV Cu at 300 °C

8.3 Conclusions

These results seem to mirror what was observed in previous bulk studies in terms of what conditions will induce a phase change in the metallic glass. The void structure was particularly interesting since the voids grew to be a large and interconnected network. In many other materials the maximum void size is largely capped due to the ability of the Helium to migrate through the sample. It appears that this metallic glass is very adept at trapping helium and forming large, inter-connected voids. This structure could be of use in filter-type applications.

The hardness data shows that the voided region is much softer when compared to the untreated samples. This is to be expected as the bubble region is an area of much lower density. It is also interesting to note that the crystallized sample has a much higher harness then the untreated sample. This is mostly attributed to the

increase in density of the sample as it undergoes the crystallization process.

Finally, characterization of the thin films between voids was unable to be performed due to the collapse of the structure. The voids formed by He bombardment were unable to withstand the bombardment by high energy Cu ions. This resulted in a sample which was crystallized, but unable to be analyzed.

9. CONCLUSIONS

Many studies have been performed in this analysis of metallic glass crystallization mechanisms. In this chapter, the overall important findings of each study are summarized. The bulk of this work is able to cover several different scenarios that a metallic glass would encounter if it were used as a material in the construction of a device that would be in a heavy radiation field.

9.1 Ultra-thin Films

In-situ observation of thin film metallic glass under ion bombardment revealed a peculiar behavior that ultra thin films on the order of 10 nm are highly resistant to crystallization both from extreme heating and ion bombardment while slightly thicker films are susceptible to crystallization. The mechanisms behind this phenomena was then explored. From finite element analysis, it has been shown that the crystallization is not likely caused by direct damage cascade heating, since the quench time is far too quick. Instead it is proposed that the crystallization is caused by a build up of excess free volume by ion bombardment. The introduced excess free volume allows for increased atomic mobility, leading to atomic re-arrangement into more stable crystal structures. The crystallization resistance of the thin films then comes from the removal of the excess free volume through the free surface. To investigate this idea, molecular dynamics simulations were performed on a thin film metallic glass sample, with induced excess free volume. These simulations showed that excess free volume is readily removed via the free surface. From this study is it concluded that, at least in the near surface region, a defect imbalance in the metallic glass can lead to crystallization. It was also shown that the metallic glass free surface is capable of removing excess free volume which can enhance crystallization resistance.

9.2 Thin Films

From the observations made of thin film metallic glasses, ion bombardment provides both a creation and a destruction mechanism for nano-crystals formed in a metallic glass matrix. Video evidence suggests that the number of crystals which have been formed by creation of excess free volume by ion bombardment saturates after a certain time. This saturation suggests a destruction mechanism as well, which was not observed in previous ultra-thin studies. Based on previous modeling research, the destruction mechanism is postulated to be directly related to the core of a damage cascade created by ion bombardment. A localized melting and rapid quenching occurs in this region, which replicates on a very small scale the process used for initially forming the metallic glass. This is able to re-amorphize crystalline structures that have formed within the film. Since both of these effects are driven by ion bombardment, it makes since that at a certain point the effects will cancel out, leaving an equilibrium level of nano-crystals in the matrix.

9.3 Layered Structures

The layered structured studies were able to clearly show that the interface effect can function very similarly to the free surface effect observed in other metallic glass compounds. In the very thin film structure there was no crystallization observed. This is thought to be because of the ability of the free surface to remove the excess free volume like the free surface seen in previous studies. In the thicker film samples, there was crystallization observed, but only away from the interface. This shows the ability of the free surface to keep crystallization from forming near the surface, but into the bulk, this effect is limited, and cannot prevent free volume buildup and subsequent crystallization.

9.4 Temperature Dependent

By looking at the temperature response of metallic glass under ion bombardment, it was found that metallic glass is very resistant to crystallization by direct ion bombardment. It was also shown that by heating the substrate to above a certain temperature with a given ion flux, the sample would fully crystallize through heating. Around the critical temperature a unique layered structure was seen which is attributed to a muli-step process made possible by the close proximity of substrate temperature to the critical crystallization temperature. More importantly, this study suggests that, for bulk samples, the ion beam cannot cause direct crystallization by creation of excess free volume. It is suggested that this is due to two processes: injected interstitials from the beam, reducing overall excess free volume, as well as multi-directional relaxation of the matrix around any sites that do have excess free volume.

9.5 Fluence Dependent

From these multiple-temperature experiments, several important correlations were able to be made between the crystallization causing diffusion effects and the amorphizing ion damage rate effect. The variable temperatures and diffusion rates all contributed to the final equilibrium structure achieved.

In the cases where the crystallized samples were irradiated at room temperature the diffusion effects were too little to overcome the re-amorphizing nature of the beam. In that case, the samples were quickly re-amorphized and remained that way all the way to extremely high levels of DPA.

It was seen from observation of the 250 °C samples that metallic glass can remain amorphous even at an elevated temperature as long as the beam intensity is high enough to continue amorphizing the sample. In this case the DPA rate was high

enough only to keep part of the ion bombarded region amorphous. The areas of lower damage rate were at a high enough temperature to nucleate crystals. Since the ion bombardment was continuing in that region, the matrix around the crystals was kept well mixed. In that case, it prevented a depleted zone from forming around the crystal, allowing the crystals to continue growing. This was in sharp contrast to the crystals outside the ion bombardment region, which did not see any crystal grain coarsening even with an extended time at an elevated temperatures.

The thermally crystallized samples were able to very clearly show the amount of segregation effected the ability of the beam to re-amorphize the metallic glass. It was observed that the sample was able to be re-amorphized at 1E14 ions/cm^2, however, unlike previous cases, the sample showed a distinct segregation of elements even after re-amorphizing. This segregation occurred since these samples were annealed at a much higher temperature than the samples crystallized with beam heating. This allowed for more stable and complete crystal formation in the thermally crystallized samples.

The patches of amorphous material seen in the 1E14 ions/cm^2 sample have a composition that closely matches the stable crystal compound of the crystal that was in that location before it was re-amorphized. The presence of this already stable crystal composition is what caused these samples to re-crystallize, unlike the beam crystallized samples that were re-irradiated at room temperature. It can be seen that with larger doses, the area with the highest DPA rate remains amorphous, while lower DPA rate zones will grow large grained crystals.

9.6 Porous MG

These results seem to mirror what was observed in previous bulk studies in terms of what conditions will induce a phase change in the metallic glass. The void structure

was particularly interesting since they grew to be such a large and interconnected network. In many other materials the maximum void size is largely capped due to the ability of the Helium to migrate through the sample. It appears that this metallic glass is very adept at trapping helium and forming large-inter-connected voids. This structure could be of use in filter type applications.

The hardness data shows that the voided region is much softer when compared to the untreated samples. This is to be expected as the bubble region is an area of much lower density. It is also interesting to note that the crystallized sample has a much higher harness then the untreated sample. This is mostly attributed to the increase in density of the sample as it undergoes the crystallization process.

Unfortunately, the crystallization resistance seen in the ultrathin samples was unable to be replicated in these samples due to the collapse and removal of the thin film structures. The crystallization of the metallic glass by ion bombardment caused the collapse and loss of the void structure. This resulted in the thin film structures that were developed, unable to be characterized.

9.7 Overall

These studies have shown that there are several phenomena that work together to cause metallic glass to either retain, lose or recover its coveted amorphous state. Ion bombardment in bulk cases is shown to have a re-amorphizing effect, as long as the crystal structures formed are close to the original composition of the metallic glass. Heating from ion bombardment in bulk cases is the only observed way crystallization occurred. In very thin film samples, crystallization can occur from the presence of excess free volume. This is an a-thermal effect which lowers the local density to such a degree, atomic mobility is produced, allowing for re-arrangement into more energetically favored crystal structures. It was also seen the the beam can re-

amorphize in these cases as well through the localized melting and rapid quenching in the core of the damage cascade region. In the case of very thin films ≈10 nm thick, crystallization is not seen to occur even under very high dose bombardments and high temperatures which induced crystallization in slightly thicker films. This behavior was attributed to the ability of the free surface to remove excess free volume which would otherwise build up and cause crystallization as seen in other parts of the sample. This crystallization resistance effect was also seen in multi-layered samples which appeared to duplicate the ability to remove excess free volume through a material interface. Lastly, metallic glass was shown to be very robust under He irradiation, able to form very large void structures without crystallizing.

All of these discoveries help define the radiation response of metallic glass under heavy radiation damage. This information can then be used when considering the use of metallic glass in applications where a high-radiation field is to be expected. This also shows that under certain conditions metallic glass does not suffer the same sorts of microstructure change that is so disruptive to the material properties of other polygrained materials such as steels, and can even recover its amorphous microstructure under the right conditions. This form of self-healing material is highly sough after in the materials research community today. With all of these beneficial properties, and robust microstructure, Metallic glass may be the material to solve some of the toughest materials challenges of today.

REFERENCES

[1] Seung-Yub Lee. Deformation mechanisms of bulk metallic glass matrix composites. *California Institute of Technology (Ph.D Disseratation)*, 2005.

[2] Vladimir A. Lobastov, Ramesh Srinivasan, and Ahmed H. Zewail. Four-dimensional ultrafast electron microscopy. *Proceedings of the National Academy of Sciences of the United States of America*, 102(20):7069–7073, 2005.

[3] Lin Shao, C.-C. Wei, J. Gigax, A. Aitkaliyeva, D. Chen, B.H. Sencer, and F.A. Garner. Effect of defect imbalance on void swelling distributions produced in pure iron irradiated with 3.5 mev self-ions. *Journal of Nuclear Materials*, 453(1âĂŞ3):176 – 181, 2014.

[4] Michael Myers, E.G. Fu, Michelle Myers, Haiyan Wang, Guoqiang Xie, X. Wang, W-K Chu, and Lin Shao. An experimental and modeling study on the role of damage cascade formation in nanocrystalization of ion-irradiated ni52.5nb10zr15ti15pt7.5 metallic glass. *Scripta Materialia*, 63(11):1045 – 1048, 2010.

[5] W. Klement, R. H. Willens, and P. Duwez. Non-crystalline Structure in Solidified Gold-Silicon Alloys. *nat*, 187:869–870, September 1960.

[6] Y. Q. Cheng, E. Ma, and H. W. Sheng. Atomic level structure in multicomponent bulk metallic glass. *Phys. Rev. Lett.*, 102:245501, Jun 2009.

[7] P. Lin, G. Palumbo, U. Erb, and K.T. Aust. Influence of grain boundary character distribution on sensitization and intergranular corrosion of alloy 600. *Scripta Metallurgica et Materialia*, 33(9):1387 – 1392, 1995.

[8] Mark Telford. The case for bulk metallic glass. *Materials Today*, 7(3):36 – 43, 2004.

[9] Toshiji Mukai, T.G Nieh, Yoshihito Kawamura, Akihisa Inoue, and Kenji Higashi. Dynamic response of a pd40ni40p20 bulk metallic glass in tension. *Scripta Materialia*, 46(1):43 – 47, 2002.

[10] S.J Pang, T Zhang, K Asami, and A Inoue. Synthesis of feâĂŞcrâĂŞmoâĂŞcâĂŞbâĂŞp bulk metallic glasses with high corrosion resistance. *Acta Materialia*, 50(3):489 – 497, 2002.

[11] C. J. Gilbert, R. O. Ritchie, and W. L. Johnson. Fracture toughness and fatigue-crack propagation in a zrâĂŞtiâĂŞniâĂŞcuâĂŞbe bulk metallic glass. *Applied Physics Letters*, 71(4):476–478, 1997.

[12] M.F. Ashby and A.L. Greer. Metallic glasses as structural materials. *Scripta Materialia*, 54(3):321 – 326, 2006. Viewpoint set no: 37. On mechanical behavior of metallic glassesViewpoint set no: 37. On mechanical behavior of metallic glasses.

[13] X. K. Xi, D. Q. Zhao, M. X. Pan, W. H. Wang, Y. Wu, and J. J. Lewandowski. Fracture of brittle metallic glasses: Brittleness or plasticity. *Phys. Rev. Lett.*, 94:125510, Apr 2005.

[14] Jan Schroers and William L. Johnson. Ductile bulk metallic glass. *Phys. Rev. Lett.*, 93:255506, Dec 2004.

[15] Ying-Kun Xu, Han Ma, Jian Xu, and En Ma. Mg-based bulk metallic glass composites with plasticity and gigapascal strength. *Acta Materialia*, 53(6):1857 – 1866, 2005.

[16] J. Z. Jiang, T. J. Zhou, H. Rasmussen, U. Kuhn, J. Eckert, and C. Lathe. Crystallization in zr41.2ti13.8cu12.5ni10be22.5 bulk metallic glass under pressure. *Applied Physics Letters*, 77(22):3553–3555, 2000.

[17] Jesse Carter, E.G. Fu, Michael Martin, Guoqiang Xie, X. Zhang, Y.Q. Wang, D. Wijesundera, X.M. Wang, Wei-Kan Chu, and Lin Shao. Effects of cu ion irradiation in cu50zr45ti5 metallic glass. *Scripta Materialia*, 61(3):265 – 268, 2009.

[18] Mustafa Bakkal, Chain T. Liu, Thomas R. Watkins, Ronald O. Scattergood, and Albert J. Shih. Oxidation and crystallization of zr-based bulk metallic glass due to machining. *Intermetallics*, 12(2):195 – 204, 2004.

[19] Jesse Carter, E.G. Fu, G. Bassiri, B.M. Dvorak, N. David Theodore, Guoqiang Xie, D.A. Lucca, Michael Martin, Mark Hollander, Xinghang Zhang, and Lin Shao. Effects of ion irradiation in metallic glasses. *Nuclear Instruments and Methods in Physics Research Section B: Beam Interactions with Materials and Atoms*, 267(8âĂŞ9):1518 – 1521, 2009. Proceedings of the 16th International Conference on Ion Beam Modification of Materials.

[20] Yu. Yavlinskii. Track formation in amorphous metals under swift heavy ion bombardment. *Nuclear Instruments and Methods in Physics Research Section B: Beam Interactions with Materials and Atoms*, 146(1âĂŞ4):142 – 146, 1998.

[21] S. Klaumünzer, Ming-dong Hou, and G. Schumacher. Coulomb explosions in a metallic glass due to the passage of fast heavy ions? *Phys. Rev. Lett.*, 57:850–853, Aug 1986.

[22] M. Sorescu, E. T. Knobbe, and D. Barb. Evolution of phases and microstructure in $fe_{81}b_{13.5}si_{3.5}c_2$ metallic glass during electron-beam and pulsed-laser irradiation. *Phys. Rev. B*, 51:840–850, Jan 1995.

[23] E.G. Fu, Jesse Carter, Michael Martin, Guoqiang Xie, X. Zhang, Y.Q. Wang, Rick Littleton, Sean McDeavitt, and Lin Shao. Ar-ion-milling-induced structural changes of cu50zr45ti5 metallic glass. *Nuclear Instruments and Methods in Physics Research Section B: Beam Interactions with Materials and Atoms*, 268(6):545 – 549, 2010.

[24] James F. Ziegler, M.D. Ziegler, and J.P. Biersack. {SRIM} âĂŞ the stopping and range of ions in matter (2010). *Nuclear Instruments and Methods in Physics Research Section B: Beam Interactions with Materials and Atoms*, 268(11âĂŞ12):1818 – 1823, 2010. 19th International Conference on Ion Beam Analysis.

[25] M. T. Myers, S. Charnvanichborikarn, L. Shao, and S. O. Kucheyev. Pulsed ion beam measurement of the time constant of dynamic annealing in si. *Phys. Rev. Lett.*, 109:095502, Aug 2012.

[26] Jonathan G. Gigax, Eda Aydogan, Tianyi Chen, Di Chen, Lin Shao, Y. Wu, W.Y. Lo, Y. Yang, and F.A. Garner. The influence of ion beam rastering on the swelling of self-ion irradiated pure iron at 450ÂăÂřc. *Journal of Nuclear Materials*, 465:343 – 348, 2015.

[27] Yongdong Liu, Seiichi Hata, Kouichi Wada, and Akira Shimokohbe. Thermal, mechanical and electrical properties of pd-based thin-film metallic glass. *Japanese Journal of Applied Physics*, 40(9R):5382, 2001.

[28] Michiaki Yamasaki, Shinya Kagao, and Yoshihito Kawamura. Thermal diffusivity and conductivity of zr55al10ni5cu30 bulk metallic glass. *Scripta Materialia*, 53(1):63 – 67, 2005.

APPENDIX A

HEAT TRANSFER CALCULATION

Two heat conduction models are used for this calculation, since it is really a 2-D problem. The metallic glass samples are a fixed to the stage using silver paste at the ends of the ribbon. A schematic of this setup can be seen in Figure A.1. It can be assumed that the ends of the metallic glass are at the indicated stage temperature. The center of the glass is not affixed well to the stage, and so an adiabatic condition can safely be assumed for the rest of the strip. The second directional effect comes from beam heating. Since the beam is only heating the very front surface of the metallic glass, there will be heat diffusion perpendicular to the surface as well as the heat diffusion along the strip.

A.1 X-direction Model Development

The first model that was developed was the heat transfer along the strip to the ends of the ribbon. Here a model was used that assumed a constant temperature condition at one edge, and an adiabatic condition in the center. For the center part of the strip (α), the beam was used as uniform heat source. The magnitude of the heat source was calculated from the beam current, energy and irradiated area. For the outer section (β), no heat source was used as it was not in the irradiated area. The fundamental equations used to generate the model are seen in Equations A.1. The boundary conditions used can be seen in Equations A.2. Continuity conditions were used at the interface. These are slightly simplified since constant material conditions are assumed.

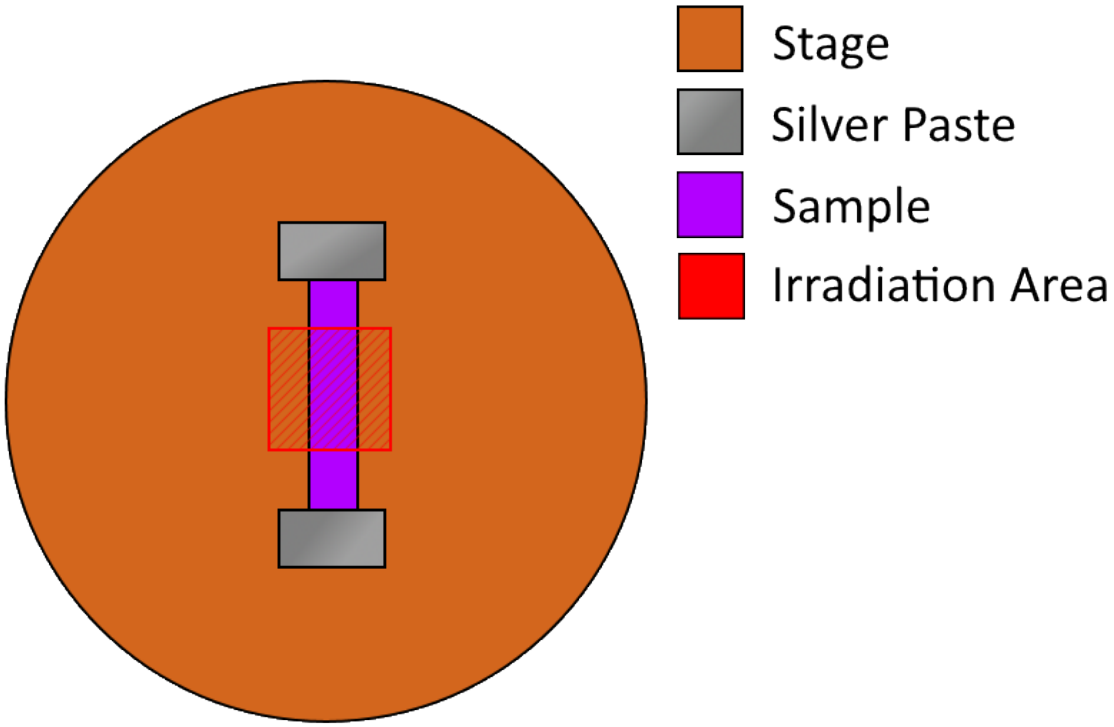

Figure A.1: Diagram showing how the MG samples are mounted for irradiation.

$$For x < X_o, k\frac{d^2T(x)_\alpha}{dx^2} + \dot{q} = 0 \tag{A.1a}$$

$$For x >= X_o, k\frac{d^2T(x)_\beta}{dx^2} = 0 \tag{A.1b}$$

In these equations X_o is distance from the center of the sample to the edge of the irradiated region, k is the thermal conductivity of the metallic glass and $\dot{q}$ is the heat generated per unit volume from the beam. For this model it is assumed that the energy of the beam is uniformly deposited through the entire width of the sample. This is not accurate to the physical phenomena that is occurring, but will

be accounted for in the second model.

Boundary Conditions

$$-k\frac{dT(\Psi)_\alpha}{dx} = \Psi \tag{A.2a}$$

$$T(0)_\beta = T_s \tag{A.2b}$$

Interface Conditions

$$\frac{dT(X_o)_\alpha}{dx} = \frac{dT(X_o)_\beta}{dx} \tag{A.2c}$$

$$T(X_o)_\alpha = T(X_o)_\beta \tag{A.2d}$$

For the boundary conditions, $T(0)_\alpha$ is the temperature of the center of the sample, T_s is the sample of the stage and Ψ is the distance from the center of the sample to the edge of the sample.

A.2 Z-direction Model Development

Next, a model is developed in order to account for the heat being transferred from the surface into the bulk of the sample. In order to do this, the sample had to be broken in to two distinct regions. One with internal heat generation, representing the near surface region within the ion range, and the rest of the sample without internal heat generation. A diagram of the layout can be seen in Figure A.2. The fundamental equations describing this model can be seen in Equations A.3

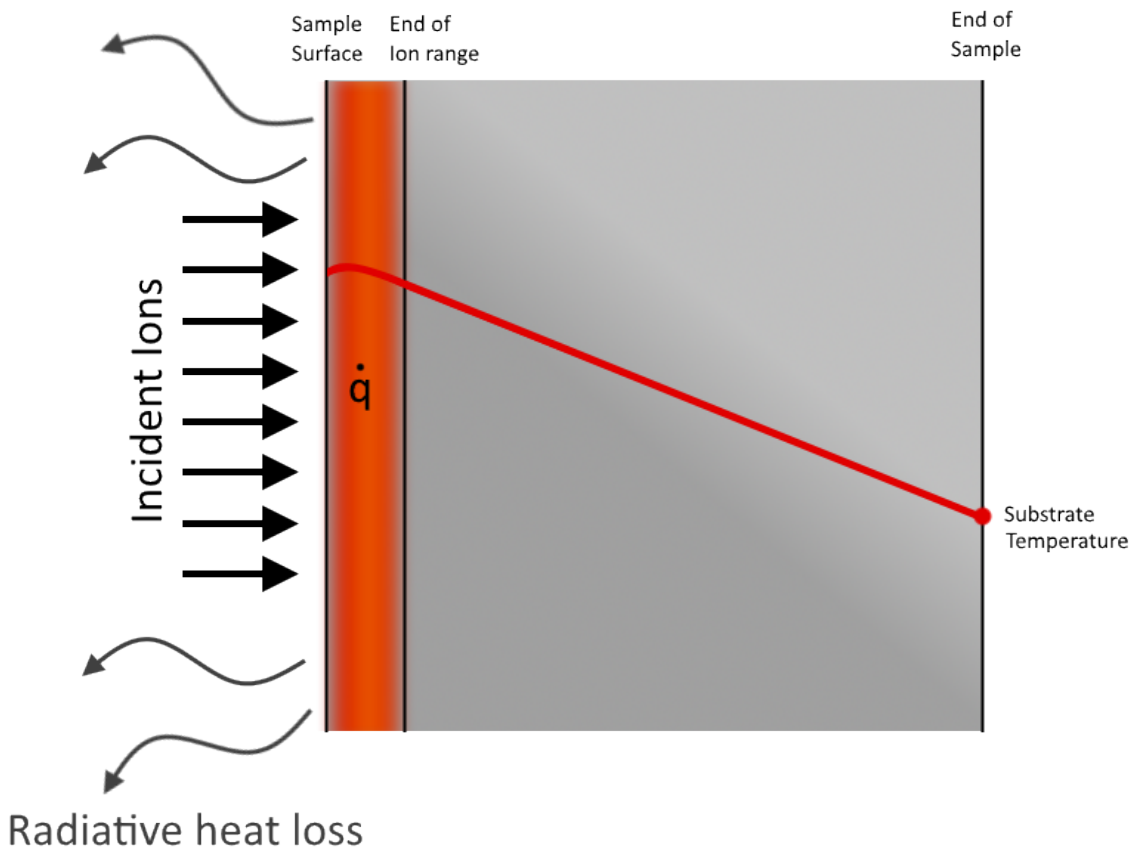

Figure A.2: Diagram showing the expected temperature curve shape and layered structure to be used for the heat transfer model.

$$For z < \phi, k\frac{d^2T(z)_\gamma}{dz^2} + \dot{q} = 0 \tag{A.3a}$$

$$For z >= \phi, k\frac{d^2T(z)_\delta}{dz^2} = 0 \tag{A.3b}$$

In these equations k is the thermal conductivity of the metallic glass and $\dot{q}$ is the heat generated per unit volume from the beam. It is assumed that the beam is uniformly depositing energy within the projected range of the ion track. This is

not exactly the heat profile generated by the beam, however, this will not effect the conclusions of this calculation significantly.

Next, boundary conditions and interface conditions must be defined. For the surface of the sample being bombarded, a radiative heat transfer condition is applied. It is assumed that the shape factor is 1 and that the emissivity is 0.15. This emissivity is chosen since the sample is a highly polished metal. The back surface of the sample is defined by a constant temperature condition. The temperature used is given from the first heat equation model. The interface conditions are simply continuity conditions, simplified since material properties are assumed constant for both areas. The boundary and interface conditions can be seen in Equations A.4.

Boundary Conditions

$$-k\frac{dT(0)_\gamma}{dz} = S\epsilon\sigma(T_c^4 - T(0)_\gamma^4) \tag{A.4a}$$

$$For x < X_o, T(\Theta)_\delta = T_\alpha(x) For x > X_o, \qquad T(\Theta)_\delta = T_\beta(x) \tag{A.4b}$$

Interface Conditions

$$\frac{dT(\phi)_\gamma}{dz} = \frac{dT(\phi)_\delta}{dz} \tag{A.4c}$$

$$T(\phi)_\gamma = T(\phi)_\delta \tag{A.4d}$$

For the boundary conditions, $T(0)_\gamma$ is the temperature of the surface of the sample, S is the shape factor of the surface, ϵ is the emissivity of the sample, σ is planks constant, T_c is the temperature of the chamber surrounding the sample and Θ is the thickness of the sample. For the interface conditions ϕ is the end of range for the ions and defines the thickness of the sample zone with internal heat generation.

Table A.1: Table showing the different parameters required to perform the heat transfer calculation

Parameter	Value	Units
Beam current	250	nA
Irradiated area	0.3	cm^2
Ion Energy	3.5	MeV
Sample thickness	200	μm
Sample length	1.0	cm
Thermal conductivity	3	W/m-K [28]
Ion charge state	2	Integer

A.3 Results

With both models defined, it was solved for a stage temperature of 275 ^{c}ircC. This case was used since this is the lowest temperature at which complete crystallization was observed. The necessary parameters to solve these equations are seen in Table A.1.

First, the temperature along the length of the sample was solved for. The resulting temperature curve can be seen in Figure A.3. The maximum temperature point at the center of the sample was 493.8 °C up from a stage temperature of 275 °C giving a temperature difference of 217 °C.

With the maximum temperature known, this is fed into the second set of equations as the constant temperature condition for the back face of the sample. The resulting curve can be seen in Figure A.4. From the back temperature of 493.8 °C the surface temperature is 494.5 °C giving a temperature difference of 0.7 °C.

A.4 Conclusion

Looking at the two models, it is clear that the majority of the temperature rise comes from the length of the sample. This also shows that the crystallization

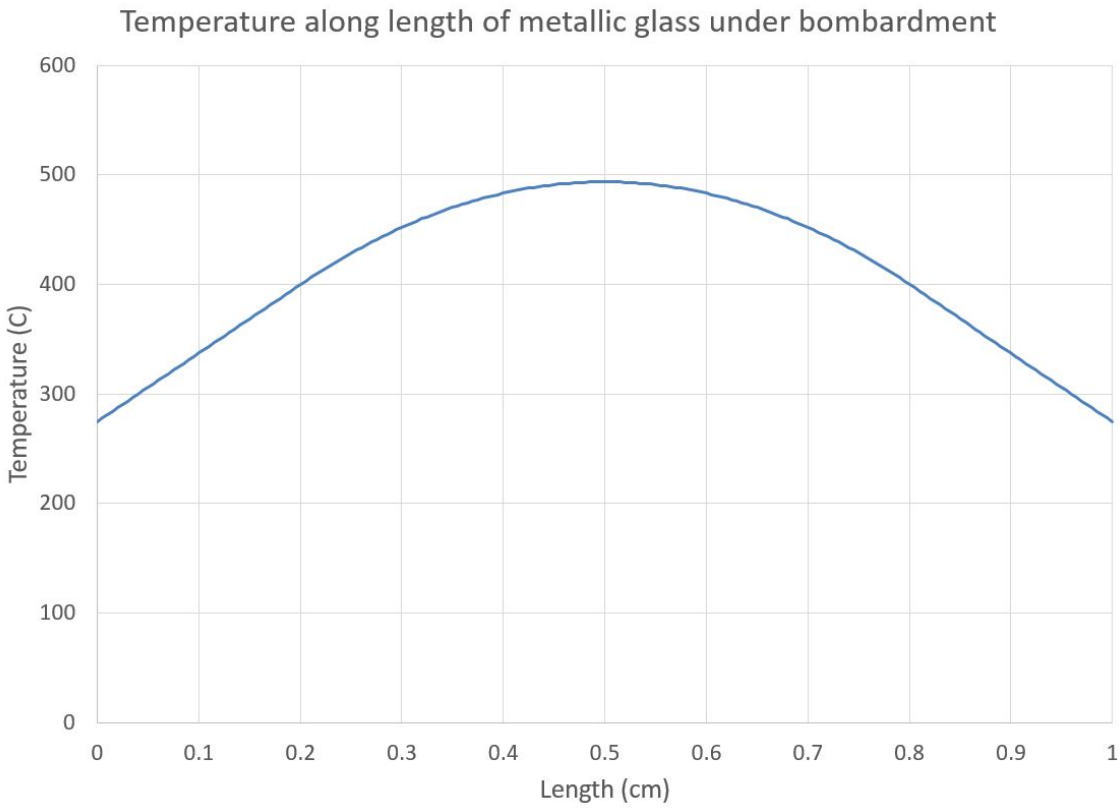

Figure A.3: Plot showing the temperature in the X-direction

observed is simply from heating the sample to above its crystallization temperature and not a beam effect. Along the Z-direction, there is hardly any temperature change. This explains why the sample is fully crystalline throughout. If the sample had a larger gradient in the Z-direction, then it could be reasonably expected that the sample would only be crystalline in the near surface and not throughout.

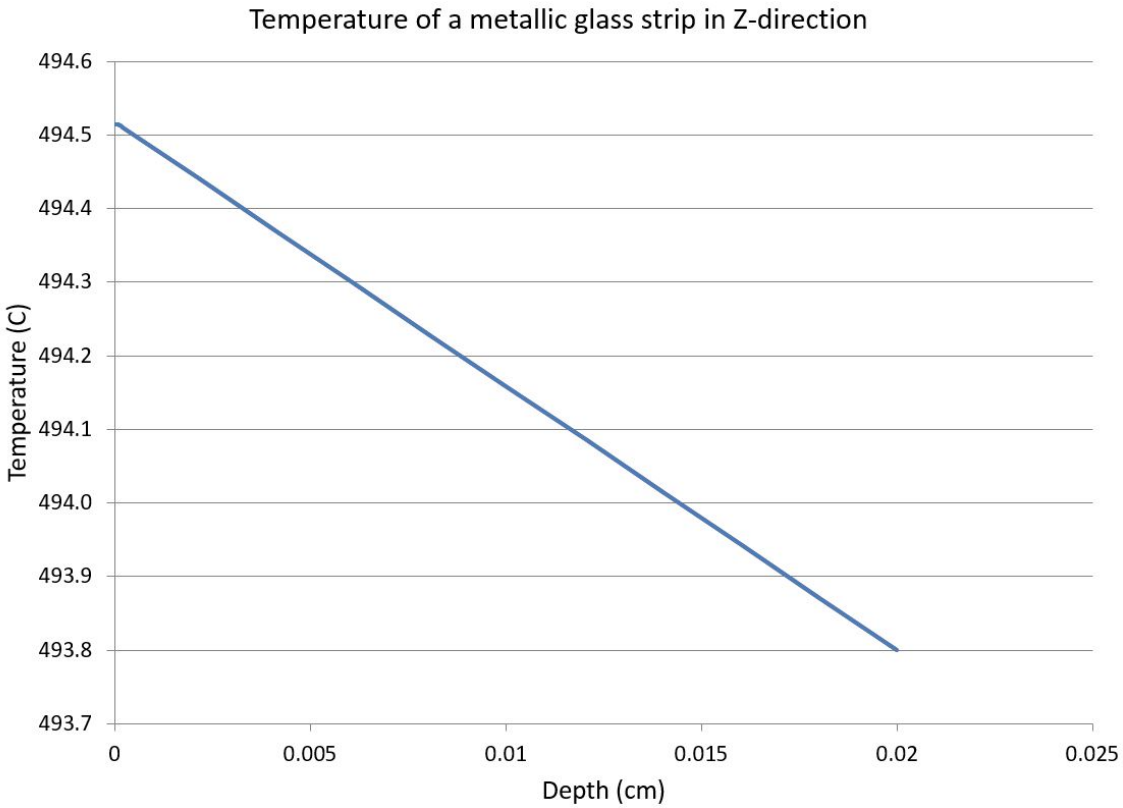

Figure A.4: Plot showing the temperature in the Z-direction